Solution-Phase Synthesis and Properties of Thin Films and Nanocomposites for Thermoelectricity

by

Yuanyu Ma

A Dissertation Presented in Partial Fulfillment
of the Requirements for the Degree
Doctor of Philosophy

Approved by November 2016
Graduate Supervisory Committee:

Robert Wang. Chair
Nathan Newman
Liping Wang
Owen Hildreth

ARIZONA STATE UNIVERSITY

December 2016

ABSTRACT

The use of nanoparticle-in-matrix composites is a common motif among a broad range of nanoscience applications and is of particular interest to the thermal sciences community. To explore this morphological theme, crystalline inorganic composites were synthesized by mixing colloidal CdSe nanocrystals and In_2Se_3 metal chalcogenide complex (MCC) precursor in hydrazine solvent and then thermally transform the MCC precursor into a crystalline In_2Se_3 matrix. The volume fraction of CdSe nanocrystals was varied from 0 to ~100% .Rich structural and chemical interactions between the CdSe nanocrystals and the In_2Se_3 matrix were observed. The average thermal conductivities of the 100% In_2Se_3 and ~100% CdSe composites are 0.32 and 0.53 W/m-K, respectively, which are remarkably low for inorganic crystalline materials. With the exception of the ~100% CdSe samples, the thermal conductivities of these nanocomposites are insensitive to CdSe volume fraction.This insensitivity is attributed to competing effects rise from structural morphology changes during composite formation.

Next, thermoelectric properties of metal chalcogenide thin films deposited from precursors using thiol-amine solvent mixtures were first reported. $Cu_{2-x}Se_yS_{1-y}$ and Ag-doped $Cu_{2-x}Se_yS_{1-y}$ thin films were synthesized, and the interrelationship between structure, composition, and room temperature thermoelectric properties was studied. The precursor annealing temperature affects the metal:chalcogen ratio, and leads to charge carrier concentration changes that affect Seebeck coefficient and electrical conductivity. Incorporating Ag into the $Cu_{2-x}Se_yS_{1-y}$ film leads to appreciable improvements in thermoelectric performance. Overall, the room temperature thermoelectric properties of

these solution-processed materials are comparable to measurements on $Cu_{2-x}Se$ alloys made via conventional thermoelectric material processing methods.

Finally, a new route to make soluble metal chalcogenide precursors by reacting organic dichalcogenides with metal in different solvents was reported. By this method, SnSe, PbSe, SnTe and $PbSe_xTe_{1-x}$ precursors were successfully synthesized, and phase-pure and impurity-free metal chalcogenides were recovered after precursor decomposition. Compared to the hydrazine and diamine-dithiol route, the new approach uses safe solvent, and avoids introducing unwanted sulfur into the precursor. SnSe and $PbSe_xTe_{1-x}$ thin films, both of which are interesting thermoelectric materials, were also successfully made by solution deposition. The thermoelectric property measurements on those thin films show a great potential for future improvements.

TABLE OF CONTENTS

CHAPTER Page

CHAPTER Page

LIST OF TABLES

LIST OF FIGURES

CHAPTER 1. INTRODUCTION AND BACKGROUND

The thermoelectric effect directly converts temperature difference into voltage differences and vice versa. This effect enables the creation of solid-state thermoelectric power generators and coolers, which are promising for addressing challenges related to energy and climate change. For example, thermoelectric power generators can convert waste heat (e.g., automotive exhaust) into electricity. Moreover, thermoelectric refrigerators eliminate the need for refrigerants, which are generally potent greenhouse gases. The efficiency of thermoelectric material is determined by its thermoelectric figure of merit, ZT,

$$ZT = \frac{S^2\sigma}{\kappa}T \qquad (1.1)$$

where S is the Seebeck coefficient, σ is electronic conductivity, T is absolute temperature, κ is thermal conductivity. The Seebeck coefficient has units of electrical potential divided by temperature and characterizes the voltage generated per degree of temperature difference. Heat is carried by both electrons and phonons, and so the thermal conductivity consists of two subcomponents, the electron thermal conductivity, κ_e, and the phonon thermal conductivity, κ_p. To achieve high ZT, a high electronic conductivity and a high seebeck coefficient is required. Simultaneously, a low thermal conductivity is needed. Those simultaneous requirements are challenging in traditional materials because of the interplay among electronic conductivity, Seebeck coefficient and thermal conductivity.

1.1 Electronic Conductivity

If n electrons per unit volume all move with velocity v, in a time dt the electrons will move by a distance vdt, so that $n(vdt)A$ electrons will cross an area A perpendicular to the velocity v. The charge crossing A in dt will be $-nevAdt$, therefore, the current density is

$$j = -nev \tag{1.2}$$

In the presence of electric field E, there will be a mean electronic velocity opposite to the field.

$$j = \sigma E \; ; \; \sigma = \frac{ne^2\tau}{m} \; ; \; \sigma = ne\mu \tag{1.3}$$

where μ is carrier mobility and τ is carrier relaxation time. The current density linearly depends on electric field E. The electronic conductivity σ depends on carrier concentration n, carrier mobility μ.

The electronic conductivity can also be derived using the Boltzmann transport equation to arrive at the following expression.

$$\sigma = -\frac{e^2}{3}\tau(E)v(E)^2 D(E)\frac{\partial f_0}{\partial E} \tag{1.4}$$

where $D(E)$ is the electron density of states per unit volume per unit energy interval, and f_0 is Fermi-Dirac distribution. This expression relates the electronic conductivity to the more fundamental aspects of a given material (i.e., the electronic band structure and the

Fermi level, which are implicitly included in the electronic density of states and Fermi-Dirac distribution, respectively).

1.2 Seebeck Coefficient

The Seebeck coefficient is the magnitude of built-up voltage when a temperature difference is applied across the material. The Seebeck coefficient is also sometimes referred to as thermopower or thermal emf in the literature, and it is defined as follows:

$$S = -\frac{\Delta V}{\Delta T} \tag{1.5}$$

Like the electronic conductivity, the Seebeck coefficient can also be related to the electronic band structure and Fermi level via the Boltzmann transport equation:

$$S = -\frac{1}{eT}\frac{\int v^2 \tau (E-E_f)\frac{\partial f_o}{\partial E} D(E) dE}{\int v^2 \tau \frac{\partial f_o}{\partial E} D(E) dE} \tag{1.6}$$

where E_f is the Fermi level. Note that if you insert the electronic conductivity expression derived from the Boltzmann transport equation, the Seebeck coefficient can be simplified as:

$$S = -\frac{1}{eT}\frac{\int_0^\infty \sigma(E)(E-E_f) dE}{\int_0^\infty \sigma(E) dE} \tag{1.7}$$

The equation above tells us that when the asymmetry of $\sigma(E)$ with respect to E_f increases, the magnitude of seebeck coefficient will increase. If we consider σ is a delta function at the average electron energy,

$$\sigma(E) \sim \sigma\delta(E - E_{ave}) \tag{1.8}$$

the Seebeck coefficient can be further simplified as :

$$S \sim -\frac{1}{eT}(E_{ave} - E_f) \tag{1.9}$$

In metal, E_f is deep inside the band, and electron distributions above and below E_f are nearly symmetric, thus cancelling out the heat they carry. Therefore, the Seebeck coefficient of a metal is small. When E_f is moves into the band gap, the electronic conductivity drops in an approximately exponential fashion because of reducing carrier concentration. However, this also increases the asymmetry in $\sigma(E)$, and causes the Seebeck coefficient to increase. (see Figure 1.1 and Figure 1.2)

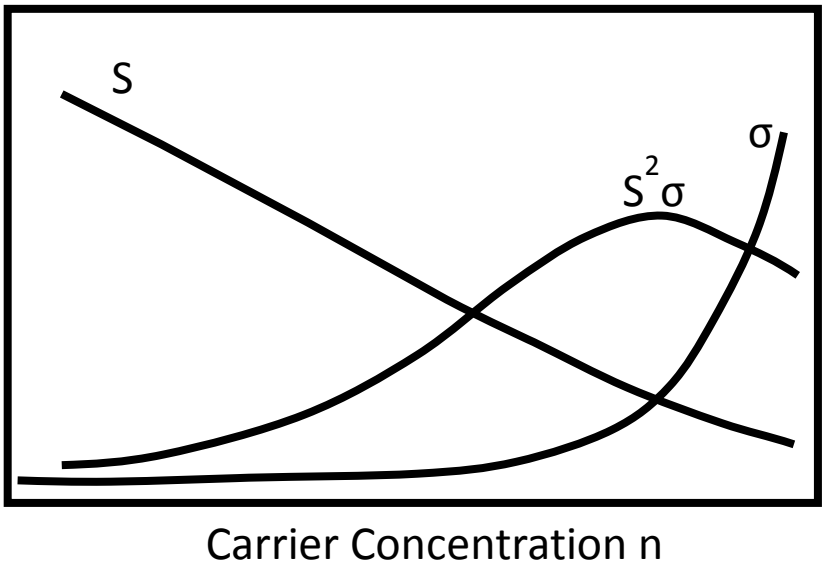

Figure 1.1 Sketch of the Seebeck coefficient *S*, electronic conductivity, σ, and power factor, $S^2\sigma$, dependences on carrier concentration, *n*.

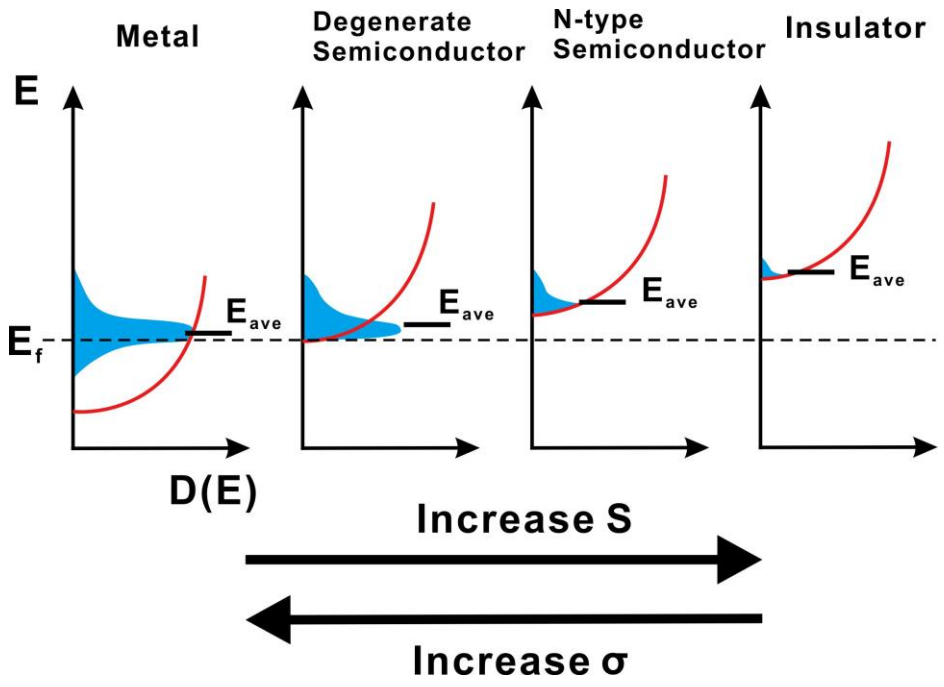

Figure 1.2 Sketch of the variation in thermopower and electrical conductivity for metals, semiconductors and insulators. The density of states is depicted by the red curve. The electrical conductivity is proportional to the number of carriers (blue area). The electrical conductivity decreases exponentially as the Fermi level moves away from the band edge. Meanwhile, the thermopower magnitude increases.

1.3. Thermal Conductivity

1.3.1. Thermal Energy Carriers

Thermal energy is transported by two major carriers: electrons and phonons. Electrons dominate the thermal transport in metals, whereas phonons dominate thermal transport in

insulators and moderately-doped semiconductors. This report focuses mainly on semiconductors and will consequently focus on phonon contribution to thermal conductivity (sometimes referred to as phonon thermal conductivity or lattice thermal conductivity).

1.3.2 Lattice Thermal Conductivity

Phonons are vibrational waves of the atomic lattice and carry energy through the crystal when they propagate. A phonon energy can be expressed as $E = \hbar\omega$ where ω is phonon frequency. Considering a simple model, one dimensional lattice. The atoms of weight M, are separated by distance A, and connected by springs whose spring constant is K. Like a photon, phonons are characterized by their frequency and wavelength. Alternatively, phonons are often characterized by their angular frequency, ω, and their wave vector, k. The relationship between ω and k, is called the dispersion relationship. This dispersion relationship can be derived by starting with the wave equation:

$$M\frac{\partial^2 u}{\partial t^2} = \mathrm{K}A^2\frac{\partial^2 u}{\partial x^2} \tag{1.10}$$

The solution of the above equation gives:

$$\omega = 2\sqrt{\frac{\mathrm{K}}{M}}\left|\sin\frac{kA}{2}\right| \tag{1.11}$$

The above equation is the phonon dispersion relationship for a 1-D monoatomic lattice. The phonon dispersion relationship is sometimes also called the phononic band diagram.

The speed that the wave is propagated is called group velocity. And it can be obtained using the following relation:

$$V = \frac{\partial \omega}{\partial k} \tag{1.12}$$

For a crystal lattice which has two different masses of atoms, m_1 and m_2, the phonon dispersion relation can be expressed as:

$$\omega_{\pm}^2 = \mathrm{K}\left(\frac{1}{m1} + \frac{1}{m2}\right) \pm \mathrm{K}\sqrt{\left(\frac{1}{m1} + \frac{1}{m2}\right)^2 - \frac{4\sin(ka/2)^2}{m1m2}} \tag{1.13}$$

The above equation is plotted in Fig 1.3. The lower branch is called the acoustic branch and the higher one is called the optical branch. The slope of the acoustic branch near the small wave vector region is the speed of sound. When the wave vector is close to the boundary of Brillouin zone ($k = \pi/a$), the dispersion curve goes flat, indicating the speed of phonons is nearly zero. The optical branches are relatively flat, which leads to slower optical phonon velocity and a negligible contribution to thermal conductivity.

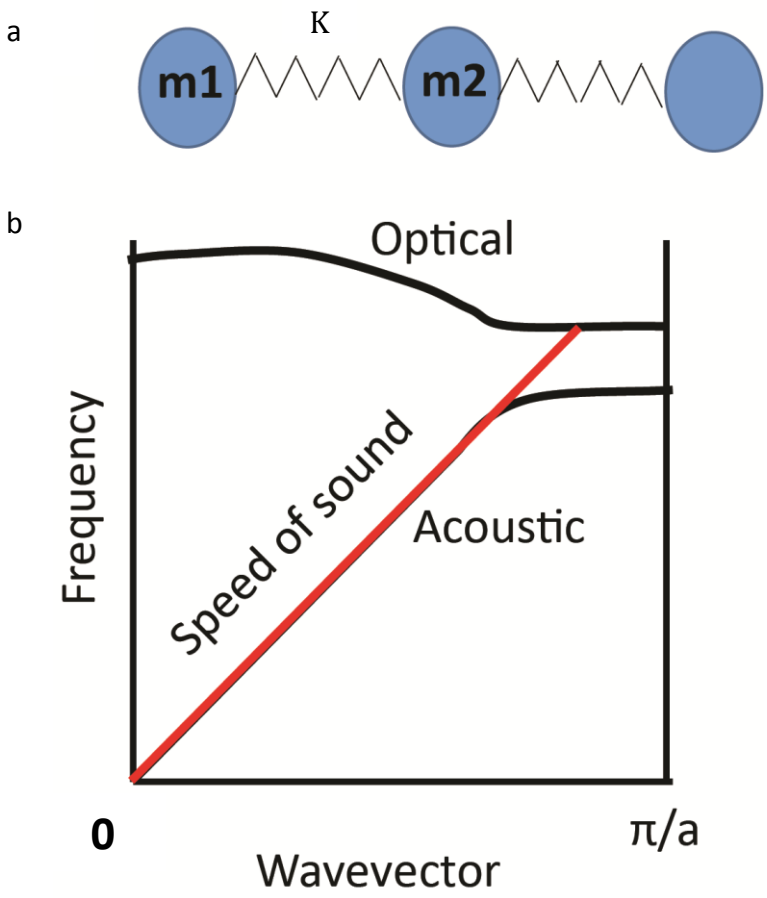

Figure 1.3 a) 1-D mass spring model with atom mass m1 and m2, and spring constant K. b) phonon dispersion relationship of a 1-D diatomic chain

1.3.3 Thermal Conductivity Expression

The phonon contribution to thermal conductivity can expressed as:

$$\kappa_p = \frac{1}{3}\int v\, l\, C_\omega d\omega \tag{1.14}$$

where $C_\omega = \hbar\omega D(\omega) df_0/dT$ is the specific heat per unit frequency at frequency ω and temperature T, v is the phonon group velocity and l is the phonon mean free path.

1.3.4 Thermal Conductivity Temperature Dependence

1.3.4.1 Specific Heat

Specific heat is one of the quantities that determines the temperature dependence of κ. In the Debye model, all branches of the dispersion relationship are replaced by three branches, each with the same linear dispersion relation. Using the Debye model, the specific heat can be derived as:

$$C_V = 9nk_B(\frac{T}{\Theta_D})^3 \int_0^{\Theta_D/T} \frac{x^4 e^x dx}{(e^x-1)^2} \tag{1.15}$$

where $x = \hbar ck/k_B T$. Θ_D is Debye temperature above which all phonon modes are excited. In the high temperature limit, $T >> \Theta_D$, the specific heat expression can be reduced to:

$$C_V = 3nk_B \tag{1.16}$$

which agrees with classical model proposed by Dulong and Petit that C_V is independent of temperature.

In the low temperature limit, $T << \Theta_D$, the specific heat expression can be simplified to:

$$C_V = \frac{12\pi^4}{5} nk_B(\frac{T}{\Theta_D})^3 \tag{1.17}$$

Specific heat is proportional to T^3 in the low temperature limit. The Debye temperature separates the low temperature region where quantum statistics must be used from the high temperature region where classical theory can still hold.

1.3.4.2 Mean Free Path

Before we discuss the temperature dependence of mean free path, we need to learn about phonon-phonon scattering. There are two types of phonon-phonon scattering, normal process and umklapp process. A normal process is a phonon-phonon scattering event in which the total momentum is conserved while in an umklapp process the initial momentum and the final momentum differ by a reciprocal lattice vector G.

In the low temperature limit, $T \ll \Theta_D$, the phonons present will have $k \ll k_D$ so that the phonon momentums are small compared to $\hbar k_D$. Since the total momentum is conversed, the momentum of phonons after collision should also be small, which means the initial momentum and the final momentum should be confined in the first Brillouin zone. Thus it is concluded that in low temperature, the most likely occurring phonon-phonon scattering event is normal process and the phonon mean free path is not determined by umklapp scattering.

When the temperature is low enough that the phonon mean free path is comparable to the mean free path due to the scattering of phonons by impurities, or even by the sides of the finite sample, the phonon mean free path is determined by the spatial distribution of impurities or the size of the sample.

In the high temperat*u*re regime, $T \gg \Theta_D$, the number of phonon that can participate in umklapp process increases exponentially. Therefore, it can be expected the phonon mean free path will decrease rapidly with increasing temperature.

1.3.4.3 Temperature Regimes for Phonon Scattering Mechanisms

Fig 1.4 shows a typical temperature dependence of thermal conductivity in a semiconductor or insulator. At low temperature, the mean free path is governed by the sample dimension or impurity concentration. The thermal conductivity dependence on temperature comes from the specific heat, C_V, which varies as T^3. When temperature continues to increase, thermal conductivity will reach a maximum at which point mean free path is no longer temperature independent and umklapp process starts to occur. The thermal conductivity then drops as umklapp phonon-phonon scattering begins to become the dominant phonon scattering process.

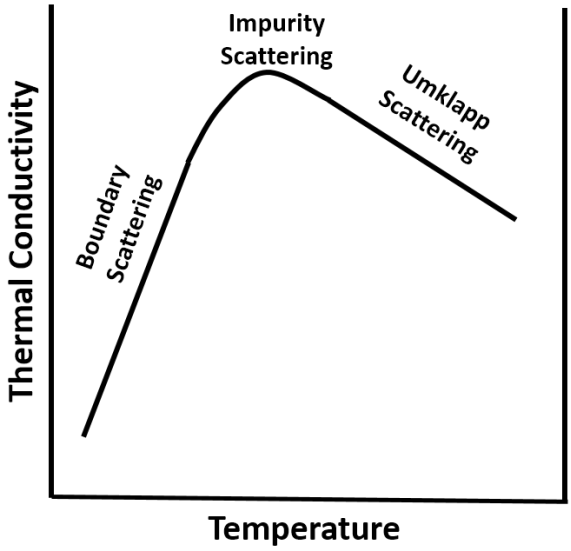

Figure 1.4 The temperature dependence of thermal conductivity for a typical semiconductor or insulator

1.4 Thermoelectric Materials

The traditional thermoelectric materials are PbTe, Bi_2Te_3 and their alloys with other substances, which was first investigated in 1950.[2, 3] PbTe and Bi_2Te_3 contain heavy elements which leads to low phonon velocity and low thermal conductivity, and they also have a large carrier mobility. Goldsmid found that alloys of Bi_2Te_3 could achieve ZT close to 1.[2] The thermoelectric community commonly targets values of ZT > 3 because this is the value at which thermoelectric device efficiencies are comparable to conventional heat pump and heat engines.

In order to achieve high ZT, one must achieve high Seebeck coefficient S, high electronic conductivity σ, and low thermal conductivity, κ, simultaneously. Because of the coupling among the variables S, σ and κ, changing them independently is very challenging.

The idea of using low dimensional materials to enhance ZT was first proposed by Hicks and Dresselhaus.[4, 5] It was believed that quantum confinement of electrons and holes will dramatically increase $S^2\sigma$. Later Mahan and Sofo[6] and Humphrey and Linke[7] predicted the best electronic density of states for thermoelectric material is a delta function. The fundamental idea is to introduce large asymmetry in $\sigma(E)$ with respect to E_f, as a result, S will be enhanced without greatly sacrificing electronic conductivity. The density of states for low dimensional materials contain sharp features that can be utilized to create charge carrier concentrations that are very asymmetric with respect to the Fermi level (see Figure 1.5)

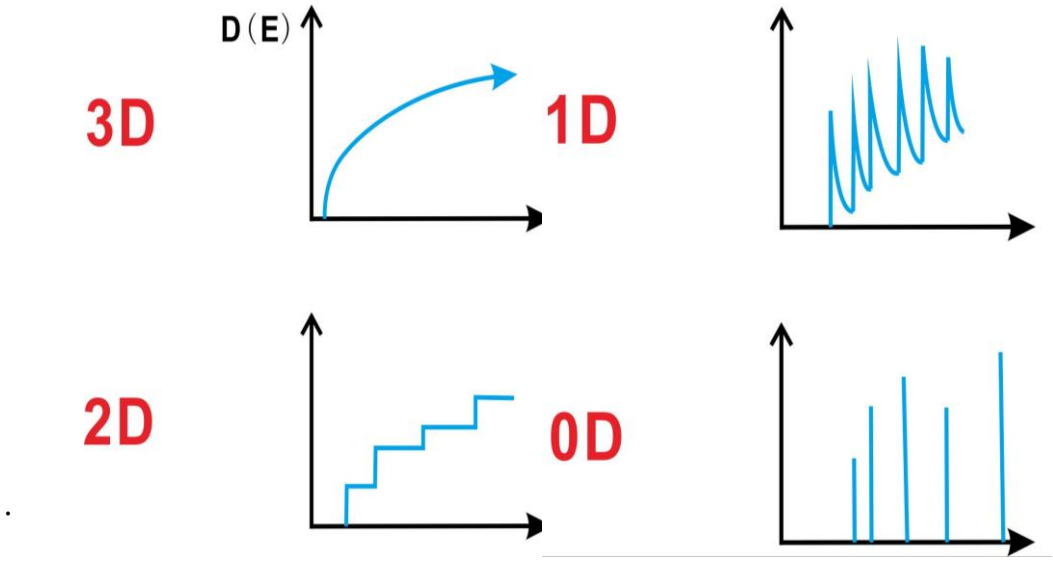

Figure 1.5 Sketches of electron density of state in low dimensional materials.

The idea of using material size as a variable to increase ZT triggered extensive research on nanostructured thermoelectric materials.[8-13] While nanostructured thermoelectric research in the past two decades has led to increases in ZT, it turns out that these increases in ZT have arisen from reductions in thermal conductivity rather than increases in $S^2\sigma$. Due to nanostructuring, the interface distance in materials is smaller than the bulk mean free paths of phonons, but larger than the bulk mean free paths of electrons. These small interface distances than cause the mean free paths of phonons to decrease while the mean free paths of electrons remains approximately the same. As a result, the thermal conductivity is reduced much more than the electrical conductivity, and ZT increases.

The initial research efforts on nanostructured thermoelectric materials focused on superlattices and quantum wells. The most successful finding is that in several cases of

superlattices, the cross plane thermal conductivity was below the 'alloy limit,' which is hard to surpass in traditional thermoelectric materials. For example, 0.5 W/m- K is achieved for a PbTe/$PbTe_{0.75}Se_{0.25}$ superlattice, which is approximately half the alloy value.[14] For Si/Ge superlattice, 3 W/m- K is achieved which is only 60 percent of the thermal conductivity of the comparable $Si_{0.8}Ge_{0.2}$ alloy. [15]

Motivated by the success of using low dimensional materials to reduce thermal conductivity, the potential of 3D nanocomposite is exploited. The idea is to have nanoinclusions like nanoparticle or nanowire in a host matrix, or to have a heterostructure with nanostructures adjacent with each other. Early research on 3D nanocomposites used molecular beam epitaxy and metal organic chemical vapor deposition as materials synthesis approach. In a landmark paper by Kim et al., they showed that $In_{0.53}Ga_{0.47}As$ containing ErAs nanoparticles led to a thermal conductivity over 50 percent lower than the alloy limit, which consequently increased ZT by a factor of 2.[16] More recently, higher throughput synthesis methods have been developed to create 3D nanocomposite thermoelectric materials. This approach commonly involves milling a bulk semiconductor into a nanopower and then hot pressing or spark plasma sintering it back together. Using this method, one can create nanograined samples with grain sizes that are comparable to the phonon mean free path, thus lowering the thermal conductivity. Poudel achieved a ZT of 1.2 at room temperature in BiSbTe alloy synthesized by ball-milling and hot-pressing, which is 20 percent higher than comparable state-of-art BiSbTe alloys.[13] Nanocomposite boron-doped Si/Ge materials were also reported to show significantly reduced thermal conductivities and enhanced ZT value compared to bulk SiGe alloys.[17]

While milling semiconductors into powders and then sintering them back to together is a straightforward process for making 3D nanocomposites, there are certain flaws lying behind this approach. First of all, it's hard to precisely control the sample morphology (grain size monodispersity and shape). Secondly, the solid-state method requires ball-milling and hot pressing/spark plasma sintering, which is often time and cost consuming.

In recent years, solution-phase synthesis routes to thermoelectric materials have received increased attention. Compared to solid-phase synthesis approaches, the solution-phase approach uses mild temperatures, mild pressures and inexpensive equipment. In this approach, nanoparticles and matrixes can be pre-synthesized and mixed in the solution phase and then converted into solid-phase nanocomposite. The size and the volume fraction of nanoparticles can be precisely controlled. Specifically, colloidal nanocrystals can be embedded in polymers, oxides, semiconductors and metals. Embedding colloidal nanocrystals in polymers is straightforward because both of these materials are soluble in a variety of solvents. However, creating matrices of inorganic oxides, semiconductors, and metals is more challenging because these materials are usually insoluble. This hurdle can be solved by finding a soluble matrix precursor that can be mixed with the colloidal nanocrystals and then converted into an inorganic oxide, semiconductor, or metallic matrix afterwards. The following chapter introduces colloidal nanocrystals and different approaches to synthesizing semiconductor/oxide precursors.

1.5. Colloidal Nanocrystals

Colloidal nanocrystals are a specific type of nanoparticle that consist of an inorganic crystalline core with organic surfactants bound to the surface.[18] The properties of the nanocrystal are predominantly determined by its inorganic core. The organic surfactants (often referred to as ligands) passivate the nanocrystal surface, stabilize the nanocrystals in solution, and facilitate inexpensive solution processing of the colloidal nanocrystals. (Fig 1.6)

Nanocrystals possess very interesting size dependent electrical, optical, thermal and magnetic properties. A representative example of these size dependent properties is the size dependent photoluminescence response of CdSe nanocrystals, which covers the whole visible spectrum.[19] (Fig 1.7)

Colloidal nanocrystals are synthesized by solution-phase methods, among which the hot injection method is commonly used to synthesize metal chalcogenide, noble metal, and transition metal nanocrystals.[20, 21] The hot injection method works by injecting nanocrystal precursor solution into a surfactant solution at high temperature. The nanocrystals nucleate upon injection due to the high temperature, but the temperature of the overall mixture quickly decreases due to the thermal mass of the nanocrystal precursor solution. At this lower temperature, the nanocrystals can continue to grow, but the nucleation of new nanocrystals is suppressed. This procedure enables the synthesis of nanocrystals with very narrow size distributions. The size and the shape of the nanocrystals can be controlled by

the reaction conditions like injection temperature, growth temperature, growing time, and monomer concentration.

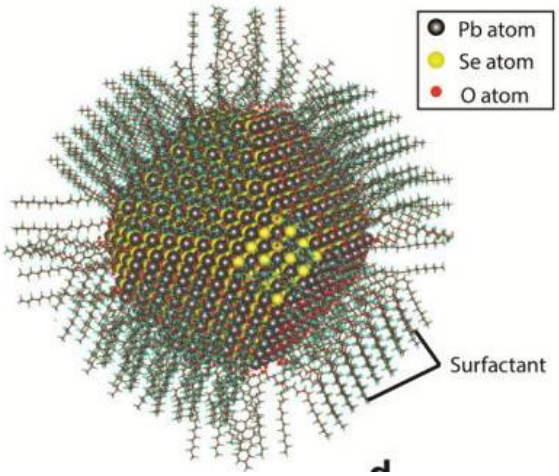

Figure 1.6 Scheme of a PbSe colloidal nanocrystal

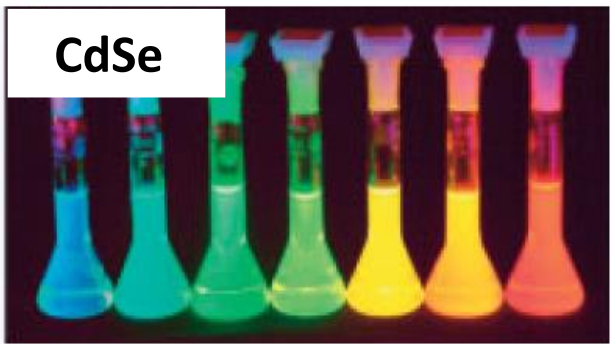

Figure 1.7 Size dependent photoluminescence by CdSe nanocrystal. Picture taken from Reference 16.

1.6 Soluble Metal Chalcogenide Precursors

In 2009, a broad range of metal chalcogenides such as tin, indium, antimony, germanium, gallium, mercury, copper, and zinc chalcogenides has been found to be soluble in solvent

hydrazine N_2H_4.[22, 23]The precursors are often referred as metal chalcogenide complexes (MCC). MCCs precursors can be spin coated and the resulting film can then be decomposed into the starting metal chalcogenide with a mild temperature treatment. An example of a MCC thermal decomposition reaction is the following, $(N_2H_5)_4Sn_2S_6 \rightarrow 4N_2H_4+2H_2S+2SnS_2$. Since most of the promising thermoelectric materials are metal chalcogenide, the discovery of MCCs precursors makes solution-phase approach a promising route to make thermoelectric materials.

MCCs can also be used to replace the conventional organic ligands that passivate the surface of colloidal nanocrystals. MCCs used in this manner fall under the growing class of inorganic ligands for colloidal nanocrystals. This class includes MCCs, metal-free chalcogenides, polyoxometallates, halide, pseudohalide and halometallates. The use of these inorganic ligands has led to greatly improved charge transport mobilities in colloidal nanocrystal materials on the order of 10^1 $cm^2/V\text{-}s$. Promisingly, very recent work using CdSe nanocrystals surface-functionalized with cadmium chalcogenidometallates has led to record mobility values on the order of 10^2 $cm^2/V\text{-}s$, which were within a factor of ~2 relative to single-crystal mobilities.[24] Moreover, MCCs can be used as soluble precursors with which to create the matrix for nanoparticle-in-matrix composites. One can easily control the amount of MCCs and nanoparticles in the solution-phase, which makes the solution-phase approach desirable in controlling the composition of nanocomposite, including nanocrystal size, shape, and composition as well as matrix composition.

Although the discovery of MCCs precursors using hydrazine triggers extensive promising research directions, a large drawback of this approach is that hydrazine is highly toxic,

explosive, and carcinogenic. To avoid this, Webber and Brutchey[25] used a much less solvent, binary thiol-amine solvent mixture, to create metal chalcogenide precursors, which also convert to metal chalcogenides under heat treatment. The metal chalcogenide precursors which can be made using this approach span a wide range,[26-30] which makes thiol-amine solvent mixtures another promising approach to make thermoelectric material. Furthermore, the precursor using diamine-dithiol solvent can be utilized as a capping ligand for nanoparticles or matrix in nanocomposite in the same fashion as the hydrazine solvent approach. [31]

Although the diamine-dithiol solvent approach eliminates the use of extremely toxic hydrazine, it still has other problems. The usage of dithiol introduces extra sulfur into the system, which makes making non-sulfide metal chalcogenides problematic. To circumvent this problem, this dissertation proposes a new soluble precursor approach by reacting diphenyl diselenide/diphenyl ditelluride with metals in solvent. By this approach, not only did we avoid the usage of highly toxic solvent, but we also avoid the introduction of unwanted sulfur into the precursor. After heat treatment, phase-pure and impurity-free metal chalcogenides can be retrieved. This approach, as a safe and clean route, has a potential to be wildly used in thin film transistors, photovoltaics, thermoelectrics, etc.

ORGANIZATION OF THIS THESIS:

This dissertation addresses solution-phase synthesis and thermoelectric properties of thin films and nanocomposites using different solvent systems and different materials. In Chapter 2, we study the thermal conductivity of nanostructured materials synthesized by mixing colloidal nanocrystals in metal chalcogenide complex (MCC) precursors in hydrazine solvent, and then decomposing the MCC precursors into a crystalline matrix. We then vary the volume fraction of nanoparticles and study its effect on the structural, chemical and thermal conductivity of the nanocomposite. The study is important in a number of ways. Firstly, it complements earlier works on nanoparticle-MCC nanocomposite systems that focused on very high nanocrystal volume fractions, but did not otherwise explore the dimension of nanoparticle volume fraction. Secondly, this work is particularly interesting to thermal science community, because nanoparticle-in-matrix composites are an appealing structure to reduce thermal conductivity. This type of structure might find its promising application in thermoelectric field. Lastly, this study shows the advantage of solution-phase synthesis over other approaches to make thermoelectric materials like molecular beam epitaxy and ball milling/hot pressing.

In Chapter 3, the thermoelectric properties of copper chalcogenide alloy thin films using a diamine-dithiol solvent mixture was first reported. This study shows diamine-dithiol solvent mixture, a far less toxic solvent compared to hydrazine, is a promising solution-phase route to make thermoelectric materials. The advantage of solution-phase synthesis like the facile control of doping and chemical composition is displayed. The thermoelectric properties of these solution-phase synthesized copper chalcogenides are

comparable to ones made by conventional methods, which is an important milestone for the solution-phase synthesis of thermoelectric materials.

In Chapter 4, we report a new route to make soluble metal chalcogenide precursors by reacting diphenyl diselenide/diphenyl ditelluride with metal in a variety of solvents. Compared to the hydrazine and diamine-dithiol routes, this new approach uses safe solvents and avoids introducing unwanted sulfur. Phase-pure and impurity free metal chalcogenides can be recovered after the precursor is decomposed. The ability of depositing the precursor solution to make thin films is also demonstrated. This new approach, as a safe and clean route, opens numerous directions for applications in thin film transistors, photovoltaics, thermoelectrics, etc.

The final chapter summarizes the results of this dissertation and discusses future research directions for advancing solution-phase synthesis routes to thermoelectric thin films and nanocomposites.

CHAPTER 2. SOLUTION-PHASE SYNTHESIS AND THERMAL CONDUCTIVITY OF NANOSTRUCTURED CDSE, IN_2SE_3, AND COMPOSITES THEREOF

2.1 Introduction

Nanoparticle composites are a morphological theme spanning applications in thermoelectrics,[13, 17, 32-36] thermal storage,[37, 38] optoelectronics,[39, 40] memory,[41, 42] and smart windows.[43, 44] Solution phase processes are a promising fabrication route to such composites because they utilize mild temperatures, moderate pressures, and inexpensive equipment, which generally lead to cost reductions. In addition, solution-phase processes provide a modular route wherein pre-synthesized colloidal nanostructures and matrices can be mixed in the solution-phase and then converted into a solid-phase nanocomposite. This approach has been commonly used to embed colloidal nanocrystals into polymers,[38, 45, 46] oxides,[47-49] semiconductors,[50, 51] and metals.[37] Embedding colloidal nanocrystals into polymer matrices is generally straightforward because both of these materials are commonly soluble in a variety of solvents. On the other hand, inorganic matrices such as oxides, semiconductors, and metals are generally insoluble. This hurdle can be circumvented by identifying a soluble matrix precursor that can be mixed with colloidal nanocrystals and then converted into a solid inorganic matrix afterwards.

Metal-chalcogenide complexes (MCCs) have been demonstrated to be soluble precursors for a broad range of metal-chalcogenide materials such as tin, indium, antimony, germanium, gallium, mercury, copper, and zinc chalcogenides.[23, 50, 52-54] These MCCs can also be used to replace the conventional organic ligands that passivate the surface of colloidal nanocrystals.[50, 51] MCCs used in this manner fall under the growing class of

inorganic ligands for colloidal nanocrystals.[55] This class includes MCCs,[50] metal-free chalcogenides,[56] polyoxometallates,[49] halide, pseudohalide and halometallates.[57] The use of these inorganic ligands has led to greatly improved charge transport mobilities in colloidal nanocrystal materials on the order of 10^1 $cm^2/V\text{-}s$.[57-62] Promisingly, very recent work using CdSe nanocrystals functionalized with cadmium chalcogenidometallates has led to record mobility values on the order of 10^2 $cm^2/V\text{-}s$ and are within a factor of ~2 relative to single-crystal mobilities.[24] This running theme of inorganic ligands has led to works on colloidal nanocrystal routes to transistors and integrated circuits,[61, 63] photovoltaics,[64] smart windows,[43] and thermoelectrics.[59, 65-69]

One attractive trait of colloidal nanocrystals with MCC ligands is that by annealing them, the MCC ligands can be transformed into an ultrathin metal-chalcogenide layer between the nanocrystals,[50, 51, 62, 69, 70] thereby creating nanocomposites with an ~100% nanoparticle volume fraction. In addition, the large variety of colloidal nanocrystal and MCC choices enables excellent control over nanocomposite parameters such as nanoparticle size and composition as well as matrix composition.

Inspired by this approach to nanocomposite fabrication, we explore the use of this chemistry to control an additional and important nanocomposite variable, that of nanoparticle volume fraction. By varying the colloidal nanocrystal – MCC precursor ratio in solution prior to nanocomposite formation, we create composites with nanoparticle volume fractions ranging from 0 to ~100%. Although such control over nanoparticle volume fraction has been previously demonstrated, few characterization details were reported.[50] In this work, we combine CdSe nanocrystals with varying amounts of In_2Se_3

MCC precursor and then characterize the resulting composites with x-ray diffraction (XRD), transmission electron microscopy (TEM), scanning electron microscopy (SEM), Rutherford backscattering spectroscopy (RBS), particle-induced x-ray emission (PIXE), and energy dispersive x-ray spectroscopy (EDX). This work complements earlier works on CdSe nanocrystals with In_2Se_3 MCCs that focused on very high nanocrystal volume fractions, but did not otherwise explore the dimension of nanoparticle volume fraction.[62, 71]

The structural motif of nanoparticles embedded in a crystalline matrix is a common theme in the thermal science community.[17, 32-36, 72, 73] In particular, it is well known that matrix-embedded nanoparticles promote broadband scattering of phonons, which correspondingly leads to low thermal conductivities. This is particularly important for thermoelectric applications wherein reduced thermal conductivities lead to large improvements in energy conversion efficiency.[17, 32-36] This chapter's solution-phase synthesis approach contrasts with many of the recent materials processes used to create nanostructured thermoelectrics such as molecular beam epitaxy,[35] ball-milling/hot-pressing,[74, 75] melt-processing,[36] and melt-processing/power-processing/spark-plasma-sintering.[32] In particular, the use of colloidal nanocrystals enables precise size control over the nanoparticle inclusions that is not possible by these other processing approaches. Furthermore, recent computational work suggests that the best nanoparticle size distribution for minimum thermal conductivity is neither a narrowly monodisperse or broadly polydisperse diameter distribution.[55] Instead the optimal size distribution consists of a mixture of several different monodisperse diameters.[55] Composites such as this could be achieved by mixing together

colloidal nanocrystals of different diameters. It should also be noted that a recent cost-analysis on thermoelectric materials and manufacturing suggests that solution-phase processing could lead to significant cost improvements relative to typical thermoelectric materials processing. [76]

Due to the importance of this nanoparticle-in-matrix structural motif to the thermal science community, we measured the thermal conductivity of our nanoparticle-in-matrix composites as a function of nanoparticle volume fraction. We find that the thermal conductivity of the CdSe – In_2Se_3 composites is very low over the entire nanoparticle volume fraction range. The average thermal conductivity of the ~100% CdSe composites is 0.53 W/m-K, which is 17 times lower than bulk single crystal CdSe.[77, 78] The average thermal conductivity of the 100% In_2Se_3 composites is 0.32 W/m-K, which is 3 times lower than other literature results on polycrystalline In_2Se_3.[79] With the exception of the ~100% CdSe sample, the thermal conductivities of these nanocomposites are insensitive to CdSe volume fraction. We believe this insensitivity is due to competing effects that both increase and decrease the composite's thermal conductivity. Many of these competing effects arise from changes in structural morphology as the composites are formed (i.e. ternary phase formation, grain orientation and size changes) and will be discussed below.

2.2 Experimental Section

2.2.1 Nanocomposite Synthesis

The nanocomposites were prepared using a four-step approach: (i) synthesis of colloidal CdSe nanocrystals (ii) functionalization of the CdSe nanocrystal surface with In_2Se_3 MCC precursor, (iii) controllably adding additional In_2Se_3 MCC precursor, and (iv) decomposing the In_2Se_3 MCC precursor into a polycrystalline In_2Se_3 matrix that encapsulates the nanocrystals.

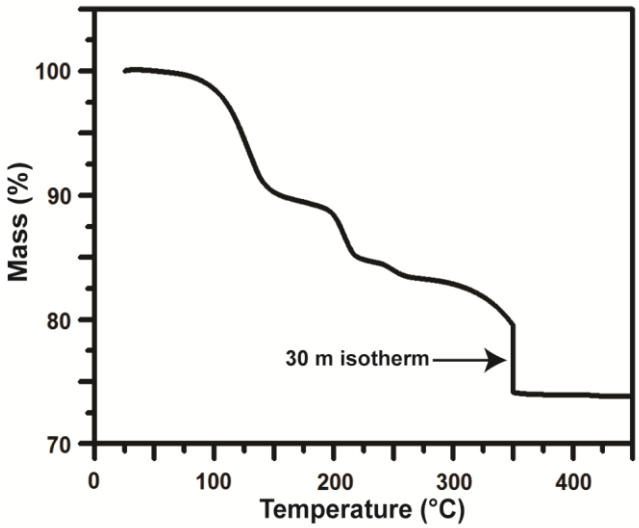

Figure 2.1 Themogravimetric analysis of the In_2Se_3 MCC precursor, $(N_2H_4)_2(N_2H_5)_2In_2Se_4$. The temperature ramp rate was 2 °C/min and a 30-minute isotherm was applied at 350°C

The In_2Se_3 MCC was made by reacting In_2Se_3 with Se and N_2H_4 to form $(N_2H_4)_2(N_2H_5)_2In_2Se_4$.[52] We confirmed the decomposition conditions for transforming this precursor into In_2Se_3 using thermogravimetric analysis. We heated the precursor to 350 °C,

applied a 30 minute isotherm, and then continued to heat the precursor to 450 °C (Figure 1.1). The lack of mass loss after the 350 °C isotherm indicates that the thermal decomposition process was complete. Composites consisting of 100% In_2Se_3 were made by directly using this precursor.

Wurtzite phase CdSe nanocrystals were synthesized by the hot injection method reported by Qu *et al.*[80]. As synthesized the CdSe nanocrystal surface is passivated by a combination of stearic acid (SA) and trioctylphosphine oxide (TOPO) ligands. These organic ligands were exchanged with the In_2Se_3 MCC precursor using the phase transfer process described by Kovalenko *et al.*[50] Two immiscible solutions, CdSe nanocrystals in hexane and MCC precursor in hydrazine, were combined and stirred for several hours. During this process, the hydrazine phase changed from colorless to dark, indicating the presence of CdSe nanocrystals functionalized with In_2Se_3 MCC precursor. The CdSe nanocrystals were then precipitated several times to separate them from unbound In_2Se_3 MCC precursor. Nanocomposites that are ~100% CdSe were made by directly using this nanocrystal solution. Nanocomposites with lower nanoparticle volume fractions were made by re-introducing appropriate amounts of In_2Se_3 MCC precursor back into the CdSe nanocrystal solution. A detailed report on the nanocomposite synthesis is available in the Appendix.The elemental composition of the composite was determined by a combination of RBS and PIXE. Since the CdSe nanocrystals and In_2Se_3 matrix in the composite reacted to form a third phase, $CdIn_2Se_4$, this elemental composition information cannot definitively determine the CdSe volume fraction in the composite (see XRD discussion in Section 6.1). Consequently we identify our composites by their In_2:Cd ratio. In the absence of $CdIn_2Se_4$

formation, a 40:60 ratio implies a composite that is 40 mol% In_2Se_3 and 60 mol% CdSe. Since the CdSe nanocrystal surface was functionalized with In_2Se_3 MCC precursor, the ~100% CdSe composites have trace amounts of In.

2.2.2 Thermal Conductivity Measurements

Thermal conductivity measurements were conducted using the differential 3ω method.[81-83] Nanocomposite samples were prepared by spin-coating the CdSe nanocrystal – In_2Se_3 MCC precursor solution onto silicon substrates and then thermally decomposing the In_2Se_3 MCC precursor at 350 °C for 30 minutes. The sample film thickness generally ranged from 50 – 130 nm. A 50 nm Al_2O_3 dielectric layer was first deposited on top of the nanocomposite film using electron beam evaporation. 150 nm thick Al 3ω lines were then patterned on top of the dielectric layer using standard lithographic techniques. Line dimensions were generally 500 – 1000 μm long and 5 – 6 μm wide, however line widths up to 20 μm were occasionally used. A Keithley 6221 was used as the current source and a Stanford Research Systems SR830 lock-in amplifier was used to measure the 1st and 3rd harmonics of the voltage signal. The temperature coefficient of resistance of the 3ω lines were measured using a custom-built temperature-controlled sample stage. The nanocomposite film thickness was measured by profilometry prior to deposition of the 50 nm Al_2O_3 dielectric layer.

Since the 3ω method measures the combined thermal response of the dielectric layer, nanocomposite film, and substrate, identical reference samples consisting of only the

dielectric layer and substrate were prepared simultaneously with the nanocomposite samples. Subtracting the thermal response of the reference sample from the measurement samples enables the nanocomposite thermal conductance to be isolated.

2.3 Results and Discussion

2.3.1 Nanocomposite Structure

The TEM images (Figure 2.2) reveal that the nanocomposite consists of randomly dispersed nanoparticles embedded in a matrix. While the general nanoparticle shape is retained throughout the composite formation, we do observe a slight increase in nanoparticle size after composite formation. The average diameter of the as-synthesized CdSe nanocrystals is 8.2 nm (Figure 2.2 a,e) whereas the average nanoparticle diameter in the 50:50 composite is 9.0 nm (Figure 2.2 c,e). We believe this slight growth in nanoparticle size is due to the formation of $CdIn_2Se_4$ at the interface between the CdSe nanocrystal and the In_2Se_3 matrix (see XRD discussion). In the absence of CdSe nanocrystals, the formation of relatively large In_2Se_3 grains is observed (38 ± 12 nm, Figure 2.2d).

The SEM images (Figure 2.3) show that mass loss and densification during thermal conversion of the MCC precursor into In_2Se_3 lead to mesoporosity in the nanocomposites. This mesoporosity was also evident when comparing film thicknesses measured via RBS and profilometry; profilometry thicknesses were approximately 20% greater than thicknesses determined by RBS, which assume fully dense films (Figures S5-S6).

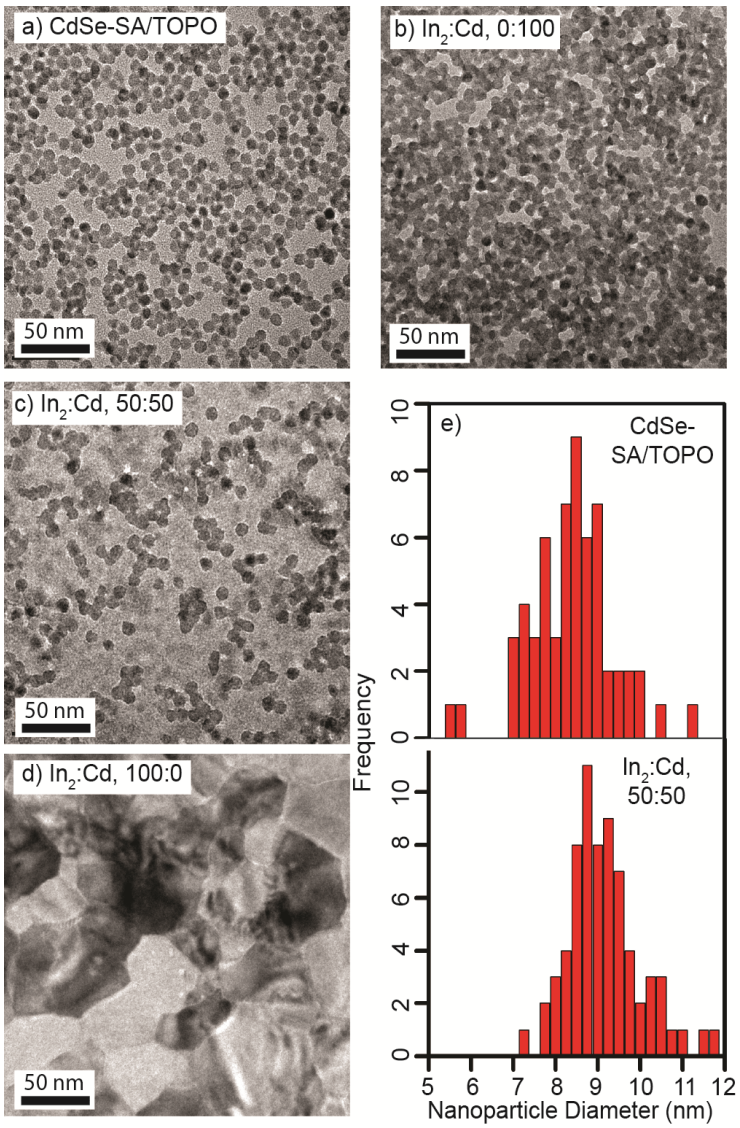

Figure 2.2 TEM images of (a) as-synthesized colloidal CdSe nanocrystals with a combination of stearic acid (SA) and trioctylphosphine oxide (TOPO) ligands and nanocomposites with In_2:Cd ratios of (b) 0:100, (c) 50:50, and (d) 100:0. Histograms illustrating the nanoparticle size distribution for the as-synthesized nanocrystals and the 50:50 composite are shown in part (e).

Structural features on the order of 10^1 and 10^2 nm in size are visible in the SEM images of 100% In_2Se_3 (Figure 2.3d). By comparison with the TEM images, we believe the 10^1 nm-scale features correspond to the In_2Se_3 grains whereas the 10^2 nm-scale features correspond to defects formed during thermal decomposition of the MCC precursor. Although the SEM images exhibit a rich surface structure, the nanocomposite films were optically smooth. Film roughnesses were generally less than 10 nm as measured by atomic force microscopy.

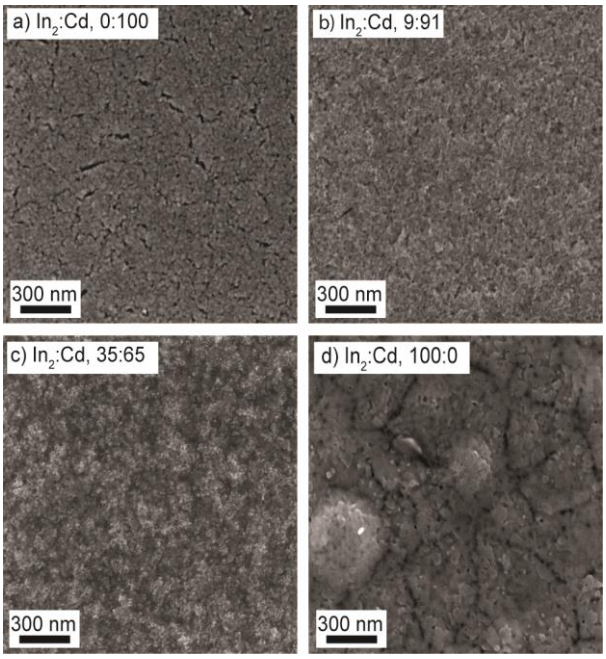

Figure 2.3 Scanning electron microscopy images of nanocomposites with In_2:Cd ratios of (a) 0:100, (b) 9:91, (c) 35:65, and (d) 100:0. Energy dispersive x-ray spectroscopy data illustrating the microscale chemical homogeneity of the sample is available in Figure S3 of the Appendix.

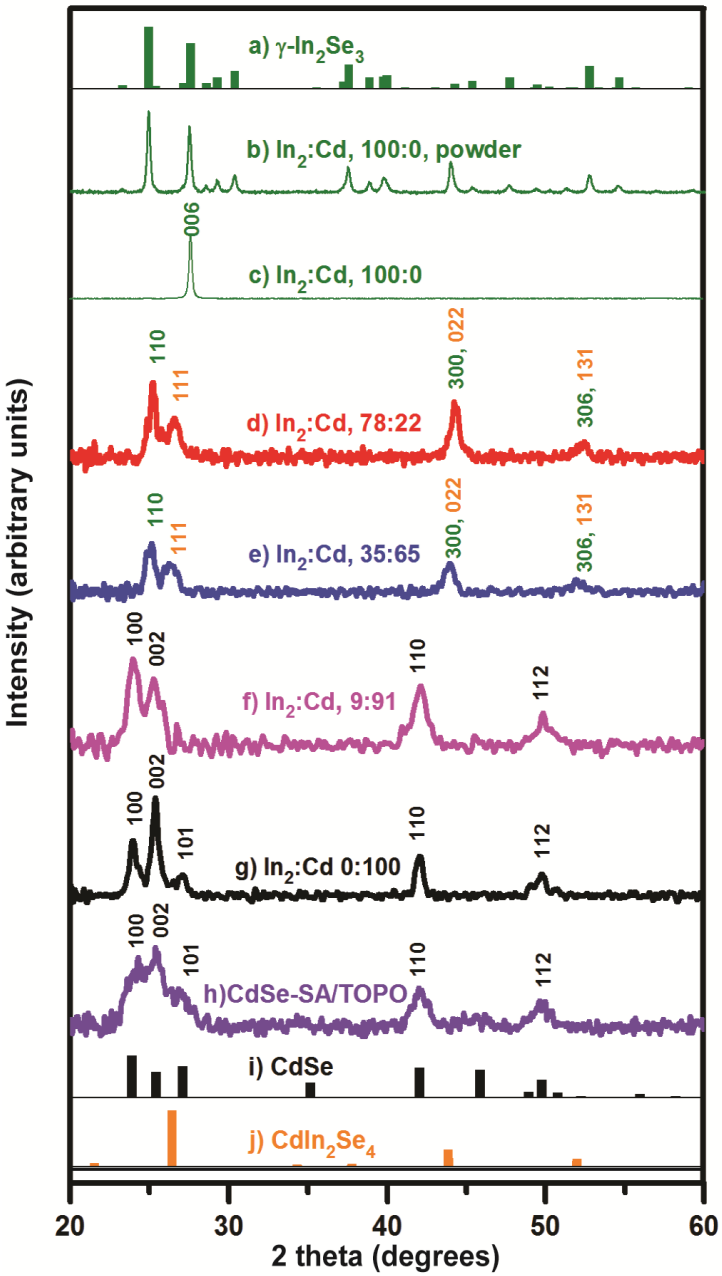

Figure 2.4 X-ray diffraction patterns of (a) γ-In_2Se_3 powder diffraction file 01-089-0658, (b) γ-In_2Se_3 powder, thin film nanocomposites with In_2:Cd ratios of (c) 100:0, (d) 78:22, (e) 35:65, and (f) 9:91, (g) 0:100 (h) as-synthesized colloidal CdSe nanocrystals (i) CdSe powder diffraction file 01-077-0021, and (j) $CdIn_2Se_4$ powder diffraction file 00-056-1124.

XRD of the decomposed In_2Se_3 MCC precursor indicates the formation of γ-In_2Se_3 (Figure 2.4b), which is one of many In_2Se_3 polymorphs.[84] γ-In_2Se_3 has a defect wurtzite structure with 1/3 of the In sites vacant.[84, 85] Due to surface effects, it can be anticipated that the formation of thin film samples may exhibit morphological changes relative to powder samples. This effect is clearly observed when thermally decomposing In_2Se_3 MCC powder relative to spin-coated In_2Se_3 MCC thin films (Figures 2.4b-c). While the powder sample closely matches the γ-In_2Se_3 powder diffraction file, the thin film sample exhibits only a single diffraction peak corresponding to (0 0 6). This indicates that the grains in the γ-In2Se3 thin films preferentially orient themselves with the ab-plane parallel to the substrate. We are unaware of any literature reports on the surface energy of γ-In_2Se_3, but believe that these growth characteristics imply that the surface energy of γ-In_2Se_3 has significant crystallographic anisotropy. Since it is thermodynamically preferable for the γ-In_2Se_3 to minimize its free energy during growth, our observed growth characteristics imply that the low- and high-energy crystal facets of γ-In_2Se_3 are parallel and perpendicular to the *ab*-plane, respectively. By growing with the *ab*-plane parallel to the substrate, the surface area of the high-energy facets was minimized. It is worth noting that another common form of indium selenide, α-In_2Se_3, is also known to be highly anisotropic.[84, 86] The strong crystallographic orientation preference of the In_2Se_3 is eliminated upon introducing CdSe nanocrystals into the composite, which indicates that the CdSe nanocrystals have a highly disruptive effect on the In_2Se_3 formation. This is indicated by the disappearance of the (0 0 6) In_2Se_3 reflection and appearance of new In_2Se_3 reflections. The large decrease in the signal:noise ratio of the XRD pattern upon inclusion of CdSe

nanocrystals also indicates that the resulting In_2Se_3 grains are much smaller than in the 100% In_2Se_3 samples. This formation of smaller grains is corroborated by TEM images of the composites; In_2Se_3 grains are clearly resolved in the 100% In_2Se_3 images, but are not resolved upon introduction of CdSe nanocrystals (Figures 2.2 c-d). This change in In_2Se_3 formation is likely due to the CdSe nanocrystals functioning as nucleation sites for In_2Se_3 crystallites. It is intuitive that the orientation of In_2Se_3 grains is random in the composites containing CdSe nanocrystals because the orientations of the CdSe nanocrystals themselves are randomized during deposition of the CdSe nanocrystal – MCC precursor mixture. It is also intuitive that the In_2Se_3 grain sizes are smaller in these composites because the presence of CdSe nanocrystals inhibits the formation of the large grains observed in the 100% In_2Se_3 samples.

The observed CdSe diffraction peak widths in our composites demonstrate that the In_2Se_3 matrix inhibits CdSe nanocrystal merger and growth (Figure 2.4f-h). The broad peaks of the as-synthesized CdSe nanocrystals with organic ligands become notably sharper in the ~100% CdSe nanocomposite, which is indicative of an increase in CdSe crystallite size.[87] Scherrer analysis of the (1 1 0) peak in the as-synthesized CdSe colloidal nanocrystals and the ~100% CdSe composite yield grain sizes of 8 nm and 20 nm, respectively. This increase in crystallite size is also visible in the TEM images, which show a significant amount of nanocrystal fusing (Figure 2.2b). This crystallite growth is not surprising given the lack of matrix in between nanocrystals and the relatively high 350°C annealing temperatures used to make the composites. However, even a modest inclusion of In_2Se_3 into the composite, such as that of the 9:91 sample (Figure 2.4f), yields a noticeable decrease in CdSe

diffraction peak sharpening. Scherrer analysis of the (1 1 0) peak in the 9:91 sample yields a grain size of 11 nm.

XRD characterization reveals the formation of a ternary phase, $CdIn_2Se_4$, in the nanocomposites and suggests a rich interaction between the CdSe nanocrystals and the In_2Se_3 matrix. Notably, only In_2Se_3 and $CdIn_2Se_4$ are observed in some of our XRD patterns (Figures 2.4d-e). While this qualitatively suggests the complete conversion of CdSe nanocrystals into $CdIn_2Se_4$ nanocrystals, such a conclusion would be oversimplified. For example, while our 35:65 sample shows only In_2Se_3 and $CdIn_2Se_4$ XRD peaks (Figure 2.4e), it is stoichiometrically impossible for this sample to only form these compounds; stoichiometry would instead dictate the formation of CdSe and $CdIn_2Se_4$. This peculiarity can be explained by calculating the relative XRD peak intensities for CdSe and $CdIn_2Se_4$, which demonstrates that x-ray diffraction from $CdIn_2Se_4$ is inherently more intense than CdSe. The intensity of a XRD peak is proportional to $|S_{hkl}|^2 M_{hkl} / V_c^2$ where S_{hkl} and M_{hkl} are the structure factor and multiplicity factor of the *hkl* peak and V_c is the unit cell volume.[87] Values for the structure factor and multiplicity factor come from analysis of the crystallographic unit cell and symmetry, respectively. Calculation of these values show that the (1 1 1) peak of $CdIn_2Se_4$ is more intense than the (0 0 2) and (1 0 0) peaks of CdSe by factors of 3.7 and 6.8, respectively (see Appendix). Consequently it is not surprising that we can observe $CdIn_2Se_4$ diffraction without CdSe diffraction.

As mentioned in the earlier TEM discussion, the slight nanocrystal diameter growth from 8.2 nm to 9.0 nm in the 50:50 sample suggests the formation of a thin $CdIn_2Se_4$ layer at the interface between the CdSe nanocrystals and In_2Se_3 matrix. It is worth noting that the

conversion of 8.2 nm CdSe nanocrystals into $CdIn_2Se_4$ via the addition of In and Se would result in 12.6 nm diameter nanocrystals, which are clearly not present in our TEM images. Nonetheless, it would still be possible to get 9.0 nm diameter $CdIn_2Se_4$ nanocrystals if Cd diffuses into the In_2Se_3 matrix. Consequently, while we believe a thin $CdIn_2Se_4$ layer between the CdSe nanocrystals and In_2Se_3 matrix is the most likely scenario, this cannot be definitively determined with the present data. Should the formation of ternary phases wish to be avoided, the use of other nanocrystal-matrix combinations with appropriate phase behavior could be used; for example, CdSe and $SnSe_2$ do not form ternary phases.[88] MCC precursors with low temperature decompositions such as that correspond to SnS_2,[22] Cu_2S,[89] or ZnTe[90] could also be used to limit elemental interdiffusion between the nanoparticles and matrix.

2.3.2 Nanocomposite Thermal Transport

Thermal transport in nanostructured materials is of interest for applications ranging from thermoelectricity, thermal barrier coatings, electronics thermal management, phase change memory, and heat assisted magnetic recording.[91] The structural motif of nanoparticles embedded in a crystalline matrix is a common theme in the thermal sciences community.[17, 32-36, 72, 73] It is well known that matrix-embedded nanoparticles promote broadband scattering of phonons, which correspondingly leads to low thermal conductivities. This is particularly important for thermoelectric applications wherein reduced thermal conductivities lead to large improvements in energy conversion efficiency.[17, 32-36] Notably CdSe alloyed with Hg has been investigated for its thermoelectrics properties.[92, 93] In

addition, a stoichiometric variant of indium selenide, In_4Se_3, is one of the best bulk thermoelectric materials.[94] Inspired by these facts, we measured the thermal conductivity of our composites.

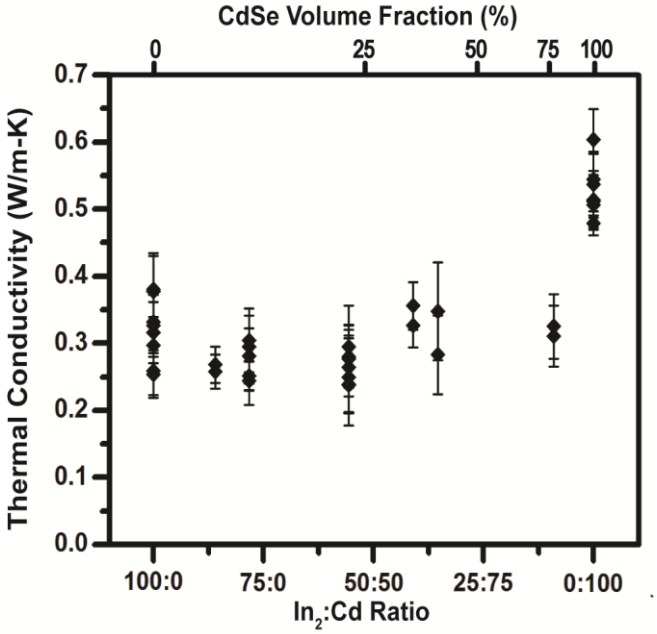

Figure 2.5 Thermal conductivity of nanocomposites with varying In_2:Cd ratios. Increasing amounts of Cd correspond to larger nanoparticle volume fractions in the composite. The upper horizontal axis indicates the nanocomposite's CdSe volume fraction in the limit of negligible $CdIn_2Se4$ formation. Thermal conductivity measurements were done on multiple films and on up to two locations per film for each In_2:Cd ratio. All data points are shown above to best illustrate sample-to-sample and location-to-location variations.

Figure 2.5 shows the room temperature thermal conductivity of the nanocomposites as a function of In_2:Cd ratio. For reference purposes, the upper horizontal axis of Figure 2.5

indicates the CdSe volume fraction in the limit of negligible $CdIn_2Se_4$ formation. The 100% In_2Se_3 and ~100% CdSe samples have average thermal conductivities of 0.32 and 0.53 W/m-K, respectively. Surprisingly, the thermal conductivities of the mixed CdSe-In_2Se_3 composites were insensitive to the amount of CdSe and were ~ 0.3 W/m-K in all cases. These low thermal conductivities are comparable to amorphous polymers, which is quite remarkable for inorganic crystalline materials. No correlation between measured thermal conductivity and film thickness was observed (Figure S4). This indicates that thermal transport in these samples is diffusive and that the thermal contact resistances between layers of the 3ω thermal conductivity samples are negligible.

The thermal conductivity of our nanostructured γ-In_2Se_3 is a factor of 3 lower than other reports on polycrystalline γ-In_2Se_3.[79] Our lower thermal conductivity can be understood in the context of microstructural differences between our samples and those in the other report.[79] Yim *et al*.[79] prepared their samples via mechanical alloying and spark plasma sintering, which led to an isotropic polycrystalline sample with grain sizes spanning tens to hundreds of nanometers. In contrast, our samples are anisotropic and have relatively monodisperse grain sizes on the order of tens of nanometers. As seen in the TEM images, the lateral grain size of our samples (which, due to their preferential crystallographic orientation, corresponds to *ab*-plane) is 38 ± 12 nm (Figure 2.2d). Although we did not directly measure the cross-plane grain size, we infer that it is smaller than the lateral grain size as dictated by the Wulff construction.[95] The Wulff construction states that crystals grow slowest in directions perpendicular to their low energy surfaces, which in our case means that the smallest grain dimension should be in the cross-plane direction. The reduced

grain sizes in our γ-In_2Se_3 relative to Yim *et al.*,[79] naturally leads to increased phonon scattering and reduced thermal conductivity.

Another factor leading to lower thermal conductivities in our γ-In_2Se_3 measurements is that we are probing transport along the *c*-axis. Since the low energy crystal facets in γ-In_2Se_3 are parallel to the *ab*-plane, the weakest bonds should be along the *c*-axis. This means that the phonon group velocities are slowest along the *c*-axis and as a consequence, the *c*-axis should be the crystallographic direction with lowest thermal conductivity. While it would be useful to assess the effect of this anisotropy by comparing to bulk single crystal γ-In_2Se_3 data, we note that thermal conductivity data in the literature is limited to polycrystalline In_2Se_3.[79, 96] We also note that although our measured thermal conductivity for γ-In_2Se_3 is quite low, it is still well above the minimum thermal conductivity predicted by the Cahill-Pohl model.[97] The Cahill-Pohl is often used to approximate the thermal conductivity of amorphous materials and is also commonly called the "minimum thermal conductivity model" and the "amorphous limit." The Cahill-Pohl model estimates a lower limit of 0.13 W/m-K for In_2Se_3 (see Appendix); this is approximately a factor of 2.5 below our measured thermal conductivity and suggests even lower thermal conductivities for γ-In_2Se_3 are possible.

The thermal conductivity of our nanostructured CdSe is a factor of 17 lower than measurements on bulk single crystal CdSe.[77, 78] In fact, our average thermal conductivity of 0.53 W/m-K is near that of the Cahill-Pohl model, which predicts a lower limit of 0.40 W/m-K for CdSe (see Appendix).[97] A thermal conductivity this low suggests very intense

phonon scattering in our ~100% CdSe composites. While thermal conductivity measurements on colloidal nanocrystals are relatively scarce, the existing literature shows that nanocrystal size and surface chemistry are the key factors determining thermal transport.[54, 71] Ong *et al.*[71] studied thermal transport in colloidal CdSe nanocrystals with varying surface chemistry and diameters ranging from 3.5 – 5.2 nm. Feser *et al.*[54] used colloidal nanocrystals to prepare polycrystalline CdSe with controlled grain sizes varying from 3.5 – 6.2 nm. The thermal conductivities in these prior works were on the order of 10^{-1} W/m-K, which is comparable to our results. However, extrapolating the results of Ong *et al.* and Feser *et al.* to the 20 nm grain size of our ~100% CdSe composites would yield thermal conductivity values greater than our measured value. The fact that our samples have larger grains, but a comparable thermal conductivity, implies that phonon scattering at our interfaces is more intense (i.e. our grain boundaries have a lower phonon transmission probability).[98] This could be a result of the different CdSe crystallite surface chemistries in our work and these prior works. Feser *et al.* functionalized their CdSe nanocrystals with HgSe MCC precursor instead of the In_2Se_3 MCC precursor used in our work. Since CdSe and HgSe form a solid solution,[99] the grain boundary interfaces in the work by Feser *et al.* are very different than ours. While Ong *et al.* also studied CdSe nanocrystals with MCC precursor ligands, they did not thermally transform the MCC precursor into a metal- chalcogenide semiconductor and consequently their interfaces also differ from ours. Differences in phonon impurity scattering between our samples and these earlier works could also be affecting thermal transport. It should also be noted that

mesoporosity differences in our samples and these prior works might also be leading to thermal transport dissimilarities.

With the exception of the ~100% CdSe sample, the thermal conductivities of our nanocomposites were surprisingly insensitive to CdSe volume fraction. The notable increase in thermal conductivity upon reaching ~100% CdSe likely arises from the increase in CdSe grain size that occurs in the absence of an In_2Se_3 matrix. We hypothesize the otherwise insensitive results to CdSe volume fraction arise from a variety of morphological changes that have competing effects on thermal conductivity. Since multiple morphological changes occur simultaneously in our composites, it is difficult to isolate the impact of any one change on thermal transport. Consequently we limit the discussion below to identifying these changes and qualitatively discussing their impact on thermal conductivity.

As CdSe is introduced into the In_2Se_3 matrix, the two most obvious morphological changes are a decrease in In_2Se_3 grain size and elimination of the preferential In_2Se_3 grain orientation. The decrease in In_2Se_3 grain size should reduce thermal conductivity due to increased phonon scattering at grain boundary interfaces. The elimination of the preferential In_2Se_3 grain orientation should increase thermal conductivity due to an increased phonon group velocity in the direction of thermal transport (i.e. as discussed earlier, the growth characteristics of the In_2Se_3 imply that the phonon group velocity is slow along the *c*-axis and fast in the *ab*-plane).

Another important morphological change is the occurrence of CdSe-In_2Se_3 grain boundaries. In the simple case of isotropic crystal structures, one would expect this to

reduce thermal conductivity. This is because compositionally-mismatched grain boundaries should have a greater acoustic impedance mismatch than compositionally-matched grain boundaries, which consequently leads to larger thermal interface resistances.[98] However, in our case the net effect of CdSe-In_2Se_3 grain boundaries is ambiguous due to the anisotropy of the In_2Se_3 grains. Crystalline anisotropy causes thermal interface resistance to be a function of both composition and grain orientation. This dependency has been both previously modeled[100] and experimentally demonstrated.[101] Although we could not find literature for the speed of sound anisotropy in γ-In_2Se_3, we note that the speed of sound anisotropy in α-In_2Se_3 is significant, ~70% for the longitudinal phonon mode.[86] We also note that the acoustic impedance mismatch in our grain boundaries is dominated by the speed of sound since the densities of CdSe and In_2Se_3 only differ by ~6%. Due to these grain orientation effects, some fraction of the In_2Se_3-In_2Se_3 grain boundaries likely have larger thermal interface resistances than CdSe-In_2Se_3 grain boundaries and vice versa. Consequently the relative impact of In_2Se_3-In_2Se_3 versus In_2Se_3-CdSe grain boundaries on thermal conductivity is ambiguous.

Yet another important morphological change is the formation of $CdIn_2Se_4$. As mentioned earlier, this $CdIn_2Se_4$ likely forms at the interface between the CdSe nanocrystals and the In_2Se_3 matrix, and so would also affect the CdSe-In_2Se_3 thermal interface resistance. If the $CdIn_2Se_4$ layer is very thin, it can have an interface "smoothing" effect[102] that decreases thermal interface resistance and thereby increases nanocomposite thermal conductivity. On the other hand, if the $CdIn_2Se_4$ is thick enough, two distinct interfaces could arise, CdSe-$CdIn_2Se_4$ and $CdIn_2Se_4$-In_2Se_3. The combined thermal resistance of these two interfaces

could be larger than that of a single CdSe-In_2Se_3 interface and thereby decrease nanocomposite thermal conductivity.

Regardless of its precise origins, this thermal conductivity insensitivity to CdSe volume fraction suggests that low thermal conductivities can be reliably achieved using this solution-phase synthesis route to nanocomposite materials. Since these thermal conductivities are already attractively low for thermoelectrics, future work measuring the other thermoelectric properties (i.e. electrical conductivity and Seebeck coefficient) is merited. Furthermore, studies using the recently-developed colloidal nanocrystal chemistries that yield charge mobilities near single-crystal values would be especially promising.[24]

2.4 Conclusions

The synthesis and characterization of nanocomposites with variable nanoparticle volume fraction made by combining CdSe nanocrystals and In_2Se_3 MCC precursor has been presented. We observe rich structural and chemical interactions between the CdSe nanocrystals and the In_2Se_3 matrix during composite formation. These interactions include alterations in In_2Se_3 grain size and orientation as well as the formation of a ternary phase, $CdIn_2Se_4$. The thermal conductivity of these composites is on the order of 10^{-1} W/m-K over the entire nanoparticle volume fraction range, which is remarkably low for inorganic crystalline materials and is comparable to amorphous polymers. With the exception of the ~100% CdSe samples, the thermal conductivity of the nanocomposite is insensitive to

CdSe volume fraction. We attribute this insensitivity to competing effects that arise from structural morphology changes as the composite is formed.

CHAPTER 3. THERMOELECTRIC PROPERTIES OF COPPER CHALCOGENIDE ALLOYS DEPOSITED VIA THE SOLUTION-PHASE USING A THIOL-AMINE SOLVENT MIXTURE

3.1. Introduction

The thermoelectric effect directly converts temperature differences into voltage differences and vice versa. This enables the creation of solid-state thermoelectric power generators and coolers, which are promising for addressing challenges related to energy and climate change.[103-106] For example, thermoelectric generators can convert waste heat into electricity and thereby boost the efficiency of power plants and automobiles. In addition, thermoelectric refrigerators eliminate the need for refrigerants, which are generally potent greenhouse gases. Much of the current thermoelectric literature focuses on developing improved thermoelectric materials and on device-level performance with these new materials.[26, 107-116]

In recent years, there has been growing interest in solution-phase routes to thermoelectric materials.[13, 112, 117-120] One reason for this interest is that solution-phase processes use mild temperatures, moderate pressures and inexpensive equipment, which inherently decrease costs. Importantly, solution-phase processes benefit thermoelectricity at the device architecture level as well. This is significant because cost analysis studies[104, 121, 122]have found that thermoelectric system cost is dominated by the heat exchangers instead of the thermoelectric materials themselves. Excitingly, new concepts in device architecture[123] leverage solution-phase processing to create devices that eliminate much of the heat exchanger costs and are more efficient than traditional flat plate designs.

Potential routes to solution-phase processed thermoelectric materials include the use of polymers and soluble inorganic semiconductor precursors. The excellent solubility properties of polymers make them attractive,[112, 118] but low charge carrier mobilities tend to hamper thermoelectric performance. The best thermoelectric materials are crystalline inorganic semiconductors, which makes finding solution-phase routes to these materials of high interest. Ideally one could deposit inorganic semiconductors by directly dissolving them in a solvent, depositing the solution, and drying. Unfortunately, inorganic semiconductors are generally insoluble due to their strong covalent bonds. One way around this hurdle is to create soluble semiconductor precursors that can be transformed into crystalline semiconductors after deposition. An excellent example of this is the use of hydrazine to create chalcogenidometallate precursors, which can be transformed into crystalline metal chalcogenide semiconductors via mild thermal treatments.[22, 23, 53] However, a large drawback of using hydrazine is that it is highly toxic, explosive, and carcinogenic.

Webber and Brutchey[25] recently discovered that metal chalcogenide semiconductors can be dissolved into binary thiol-amine solvent mixtures to create soluble precursors. This binary solvent approach is particularly attractive because these solvents are much less hazardous than hydrazine. This binary solvent approach has since been used to create soluble precursors for a large variety of metal chalcogenide semiconductors.[25, 28, 29, 124, 125]

It has been hypothesized that the mixing of ethylenediamine(en) and ethanedithiol(edt) solvent leads to extensive ionic cluster formation with possible stoichiometries of $(enH^{+})_2(edt^{2-})(en)_x$ or $(enH_2^{2+})(edt^{2-})(en)_x$.[25] The thiolate anions play an important role in

dissolving metal chalcogenides. It is hypothesized that with the addition of metal chalcogenides into the en-edt solvent mixture, thiolatochalcogenometallate anions countered balanced by $(enH^+)_2$ or enH_2^{2+} is a likely solute. For example, nuclear magnetic resonance (NMR) spectroscopy and Raman spectroscopy were used to identify bis(ethanedithiolate)tin(II) as the likely solute after Sn/SnO/SnS dissolves in en-edt solvent mixture.[124] While the above hypothesis still needs further experiments to confirm, it appears to be the most plausible one.

The deposition and characterization of photovoltaic Cu_2SnSe_3,[126] $Cu_2ZnSn(S_xSe_{1-x})_4$,[30] and $Cu(In,Ga)Se_2$[127] has already been demonstrated and promising performance achieved. Many of the best thermoelectric materials[105, 106, 108, 110]are metal chalcogenides (Cu_2X, Bi_2X_3, PbX, SnX, etc. where X = S, Se, or Te), which suggests that this binary solvent approach is promising as a solution-phase route to thermoelectric materials as well.

In this chapter, we report the first thermoelectric property measurements on metal chalcogenide thin films made using this thiol-amine solvent approach. More specifically, we combine $Cu_{2-x}Se$, $Cu_{2-x}S$, and Ag_2S precursors to create $Cu_{2-x}Se_yS_{1-y}$ and Ag-doped $Cu_{2-x}Se_yS_{1-y}$ thin films. We use Rutherford backscattering spectroscopy (RBS), scanning electron microscopy (SEM), and x-ray diffraction (XRD) to characterize the structure of these materials. We then gauge the thermoelectric performance of these materials by measuring Seebeck coefficient, electrical conductivity, and thermal conductivity at room temperature. We find that the room temperature thermoelectric properties of these solution-processed materials are comparable to measurements on $Cu_{2-x}Se$ alloys made via conventional thermoelectric material processing methods.[110, 128-130] Achieving parity

between solution-phase processing and conventional processing is an important milestone and demonstrates the promise of this binary solvent approach as a solution-phase route to thermoelectric materials.

3.2. Experimental Methodology

3.2.1. Precursor Synthesis

We synthesized three separate precursors for $Cu_{2-x}Se$, $Cu_{2-x}S$, and Ag_2S using thiol-amine solvent mixtures as reported by Lin *et al.*[125] and McCarthy *et al.*[29] The $Cu_{2-x}Se$ precursor was made by stirring a mixture of 100 mg Cu_2Se, 2 mL of ethylenediamine (EDA/en) and 200 μL of ethanedithiol (EDT) for more than 10 minutes to yield a transparent reddish-brown solution. The $Cu_{2-x}S$ precursor was made by stirring a mixture of 100 mg Cu_2S, 2 mL of EDA and 200 μL of EDT for more than 10 minutes to yield a brown solution. The Ag_2S precursor was made by stirring a mixture of 236 mg of Ag_2O, 1 mL of EDA, and 250 μL of EDT for 1 day to form a transparent colourless solution. All precursor solutions were filtered to remove any undissolved solids. These three precursors were then mixed in appropriate ratios to create the desired $Cu_{2-x}Se_yS_{1-y}$ or Ag-doped $Cu_{2-x}Se_yS_{1-y}$ samples. Prior to this precursor mixing process, we diluted the Ag_2S precursor so that it could be accurately added in the necessary small quantities. Note that the thiols in the solvent can function as a sulfur source when thermally decomposing these precursors. Hence thermal decomposition of the $Cu_{2-x}Se$ precursor yields a sample of approximately $Cu_{2-x}Se_{0.67}S_{0.33}$ composition (see Results and Discussion). Similarly the Ag_2O and thiols combine to form

Ag_2S when thermally decomposing the Ag_2S precursor. All of the precursor preparation was done in a nitrogen-filled glovebox.

At present, the nature of the dissolved Cu_2Se solute is unknown. However prior literature provides some possible clues.[25, 124] I hypothesize that upon the dissolution of Cu_2Se in the ethylenediamine and ethanedithiol solvent mixture, (ethanedithiolate)copper selenide counter balanced by enH_2^{2+} or $(enH^{1+})_2$ is the likely solute (Fig 3.1). This hypothesis could be tested by using NMR spectroscopy and/or Raman spectroscopy.

To prepare the precursors described above, we purchased ethylenediamine (>99.5%, purified by redistillation, product 391085), Cu_2Se (>99.95, product 481629), and Cu_2S (99.99%, product 510653) from Sigma-Aldrich. Ag_2O (99.99%, product 42577) was purchased from Alfa Aesar. Samples were prepared using ethanedithiol purchased from either Alfa Aesar (>98%, product L12865) or Sigma Aldrich (>98.0%, product O2390).

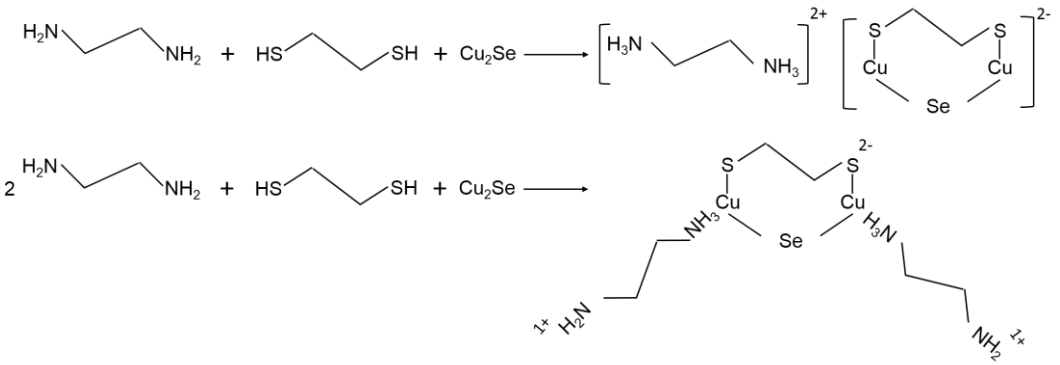

Figure 3.1 Hypothesized structures of the Cu_2Se precursor made via dissolution in the ethylenediamine and ethanedithiol solvent mixture.

3.2.2. Thin Film Deposition

Substrates were cleaned with acetone and isopropanol and then treated with UV ozone for 10 minutes prior to film deposition. In a typical film deposition, substrates were covered in filtered precursor solution then spin-coated at 2500 RPM for 45 seconds. Substrate size varied from ~1 x 1 cm to ~2 x 2 cm. Film thickness was controlled by varying spin speed and/or adjusting precursor concentration in the EDA-EDT solvent mixture. The precursor films were first dried by placing on a hotplate set to 125 °C for 15 min. The films were than thermally transformed into $Cu_{2-x}Se_yS_{1-y}$ or Ag-doped $Cu_{2-x}Se_yS_{1-y}$ samples by ramping up the hot plate to the annealing temperature and maintaining that annealing temperature for at least 30 minutes. Annealing temperatures were varied from 310 – 390 °C. In order to ensure the accuracy of our reported annealing temperatures, we created temperature calibration curves that relate the hotplate set temperature to the substrate surface temperature. These calibration curves were created by bonding thermocouples to the surface of reference substrates (i.e. amorphous quartz substrates and silicon substrates) while varying the hot plate temperature (Figure 3.2). Note that all annealing temperatures in this chapter refer to the true temperature at the surface of the substrate.

The thin films in this chapter ranged from 60 – 90 nm thick and were prepared on either amorphous quartz or silicon substrates. We did not observe any morphology differences between films prepared on quartz and silicon (Figure 3.3). This is likely because the native oxide on the silicon substrate makes that surface nearly identical to quartz.

Quartz substrates were used in samples for electrical conductivity measurements, Seebeck coefficient measurements, x-ray diffraction, scanning electron microscopy, and

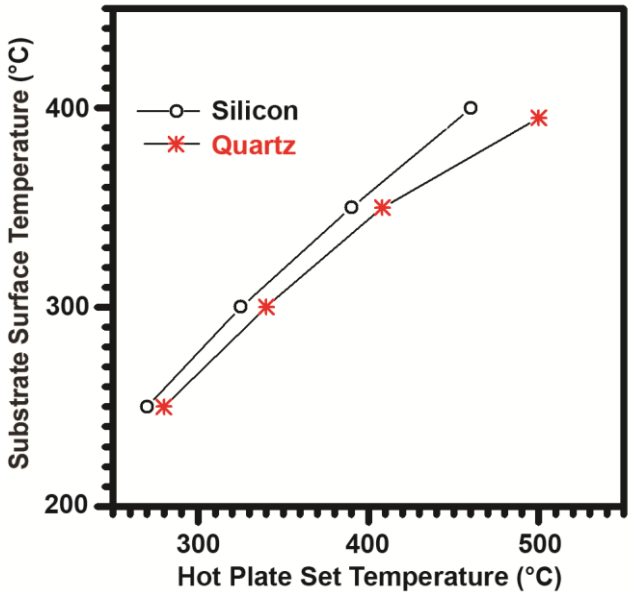

Figure 3.2 Temperature calibration curves that relate the surface temperatures of silicon and quartz substrates to the hot plate set temperature.

Rutherford backscattering spectroscopy. Silicon substrates were used in samples for thermal conductivity measurements. The use of both quartz and silicon substrates was necessitated by differing requirements for charge transport and thermal transport measurements (see Section 2.4 for more detail). All thin films were deposited and stored in a nitrogen-filled glovebox to prevent oxidation effects.

3.2.3. Materials Characterization

The $Cu_{2-x}Se_yS_{1-y}$ precursor was characterized using a thermogravimetric analyzer (Setaram TG92). The thermogravimetric analysis sample was prepared by dropcasting the

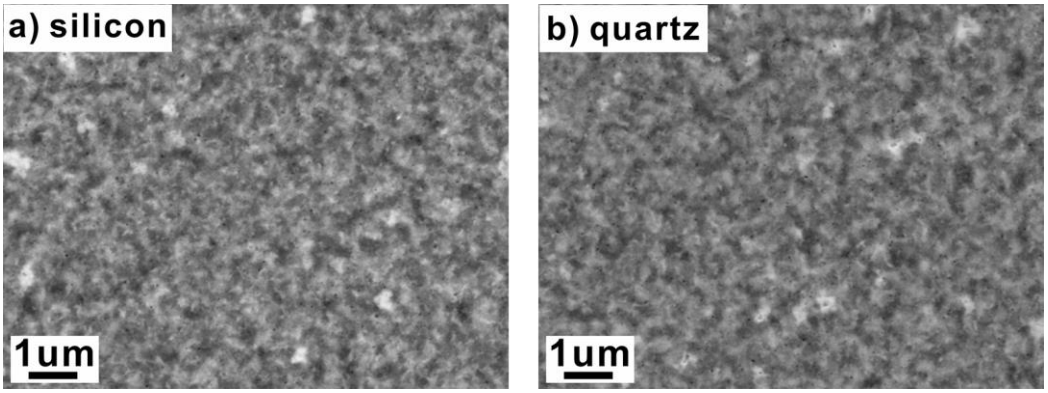

Figure 3.3 Scanning electron micrographs of $Cu_{2-x}Se_yS_{1-y}$ films prepared by spin-coating on a) silicon substrates and b) amorphous quartz substrates. No sample morphological differences are observed between these two substrates. This lack of morphology difference likely arises because the native oxide of the silicon makes the silicon surface nearly identical to the amorphous quartz substrates

precursor solution onto a substrate and drying on a hotplate set to 125 °C for 30 min. The solidified precursor was then scraped off of the substrate and then placed into the thermogravimetric analyzer, where it was heated from room temperature to 450 °C at 2 °C/min in a helium atmosphere.

Bulk $Cu_{2-x}Se_yS_{1-y}$ samples for XRD studies were prepared in a similar fashion to the thermogravimetric analysis samples. First a thick film of precursor was prepared by dropcasting the precursor solution onto a substrate. The precursor film was then annealed for 60 min. The sample was then scraped off of the substrate, ground into a powder, and examined in the x-ray diffractometer.

Films were characterized using a combination of RBS, XRD, SEM, and profilometry. High-resolution XRD was performed using a PANalytical X'Pert PRO MRD with CuKα X-ray source operating at 40 kV and 40 mA. SEM and profilometry were performed using a FEI XL30 and Bruker Dektak XT, respectively.

RBS was done using a 1.7 MV Tandetron Ion Accelerator made by General Ionex. The RBS data was collected using 3 MeV He^{2+} ions and analyzed using RUMP. The measurement uncertainty for the RBS data was determined using a combination of i) iterative data fitting with RUMP, ii) visual inspection of the data fit, and iii) matching the integrated areas of the elemental peaks between the RUMP fitting and RBS data. RUMP accounts for the experimental parameters of the RBS system during its data fittings. Consequently the indicated uncertainties for the RBS data account for bias uncertainties in our RBS setup as well as statistical uncertainties arising from weak elemental signals (i.e. the Ag signal had low counts).

3.2.4. Thermoelectric Property Measurements

Seebeck coefficient measurements were performed using the steady-state slope method.[131] The temperature gradient for the Seebeck coefficient measurement was created using two commercially available thermoelectric devices to heat and cool opposite ends of the sample. The heating and cooling of the sample was applied such that the average sample temperature was approximately room temperature. The temperatures at the hot and cold ends of the sample were measured using T-type thermocouples and a Stanford Research Systems SR630 Thermocouple Reader. The open circuit voltage was measured for six

temperature differences ranging from -20 to +20°C using an Agilent 34401A Multimeter. Plotting a curve of voltage (V) versus temperature difference (ΔT) and then taking the negative slope of the curve yields the Seebeck coefficient, $S = -V/\Delta T$. A positive Seebeck coefficient indicates that the sample is p-type and that the cold region of the sample develops a higher potential than the hot region. The temperature uncertainties in the sample's hot and cold regions were the dominant contributor to the uncertainty in each Seebeck coefficient measurement. This resulted in a Seebeck coefficient measurement uncertainty of ± 10%.

Electrical conductivity measurements were performed using the van der Pauw method and conducted on the same samples used to measure the Seebeck coefficient. The sheet resistance was measured using a Keithley 2400 Sourcemeter by taking current-voltage data at 10 points for currents ranging from -50 to +50 μA. The sample thickness was measured by scratching the sample and performing profilometry at the scratch location. Uncertainty in film thickness uniformity was the dominant contributor to the uncertainty in each electrical conductivity measurement. This resulted in an electrical conductivity measurement uncertainty of ± 5%. Samples for electrical conductivity and Seebeck coefficient measurements were prepared on quartz substrates. The use of electrically insulating quartz substrates ensures that all charge transport occurs within the thin film sample itself. Seebeck coefficient and electrical conductivity measurements were also done in a nitrogen-filled glovebox to ensure that the samples were not affected by oxidation.

Thermal conductivity measurements were done using the differential 3ω method.[81-83] An approximately 150 nm SiO_2 dielectric layer was first deposited on top of the samples by

sputtering. This dielectric capping layer protects the samples against oxidation effects and also ensures that the electrical current applied during the 3ω measurement stays isolated within the 3ω measurement lines. 3ω measurement lines were then patterned on top of the dielectric layer using standard photolithography techniques. The 3ω lines were made of 150 nm thick Al and had varying widths and lengths ranging between 6 - 15 μm wide and 800 - 1000 μm long. Current was applied to the 3ω line using the internal voltage source of a Stanford Research Systems SR830 Lock-in Amplifier. The SR830 Lock-in Amplifier was also used to measure the 1^{st} and 3^{rd} harmonics of the voltage signal. A differential op-amp and potentiometer was used to isolate the 3^{rd} harmonic of the voltage signal coming from the 3ω line. The temperature coefficient of resistance was measured using a custom-built temperature-controlled sample stage and an Agilent 34401a Multimeter. Since the 3ω method measures the combined thermal response of the dielectric layer, thin film sample, and substrate, reference samples consisting of only the dielectric layer and substrate were prepared identically and simultaneously with the measurement samples. Subtracting the thermal response of the reference sample from the measurement samples enables the thermal conductance of the thin film samples to be isolated. Thermal conductivity measurement samples were prepared on silicon substrates instead of the amorphous quartz substrates used for electrical conductivity and Seebeck coefficient measurements. Since the thermal conductivity of silicon is two orders of magnitude higher than amorphous quartz, this choice of substrate minimizes the temperature drop in the substrate and maximizes the temperature drop in the thin film during thermal conductivity measurements. This increases the sensitivity of the 3ω signal to the thin film and improves

measurement quality. The uncertainties in the 3ω line's temperature coefficient of resistance as well as the film thickness uniformity were the two dominant contributors to uncertainty in each thermal conductivity measurement. This resulted in a thermal conductivity measurement uncertainty of ± 15%.

We found that $Cu_{2-x}Se_yS_{1-y}$ and Ag-doped $Cu_{2-x}Se_yS_{1-y}$ could be routinely prepared using the procedures and reagents described in Sections 2.1-2.2 as based upon RBS, XRD, and SEM data. However, we found that the history of the ethylenediamine solvent could affect the resulting thermoelectric properties of the films. Ethylenediamine is extremely hygroscopic, and we speculate that absorption of impurities from the atmosphere in our wet chemistry glove box may be the origin of this behavior. To mitigate this effect, we prepared all thermoelectric measurement samples using a brand new bottle of ethylenediamine that was purified by redistillation by Sigma Aldrich (product 391085) and shipped in a Sure/Seal^{TM} bottle. This bottle was opened immediately prior to precursor preparation. The thermoelectric properties reported in this chapter came from two separate sample batches prepared three weeks apart and made with two different brand new ethylenediamine bottles.

3.3. Results and Discussion

Thermogravimetric analysis of the $Cu_{2-x}Se$ precursor indicates that the mass loss in the precursor is approximately complete at 275 °C, which indicates that this temperature is sufficient to transform the precursor into $Cu_{2-x}Se_yS_{1-y}$ (see Figure 3.4 and Table 3.1). To identify what effects the final precursor annealing temperature had on $Cu_{2-x}Se_yS_{1-y}$

structure, composition, and thermoelectric properties, we prepared samples with annealing temperatures of 310, 350, and 390 °C.

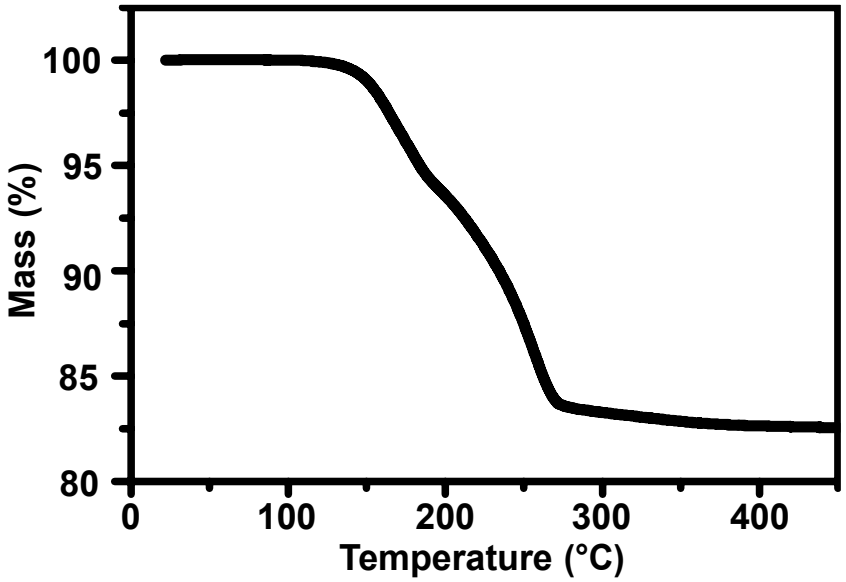

Figure 3.4 Thermogravimetric analysis of the $Cu_{2-x}Se$ precursor carried out at a temperature ramp rate of 2 °C/min and conducted in a helium atmosphere. Prior to the thermogravimetric analysis, solvent was removed from the precursor by placing the sample on a hotplate set to 125 °C for 30 minutes.

We next studied the chemical composition of our samples using RBS (Table 3.1). When the $Cu_{2-x}Se$ precursor is annealed at 310 °C, the resulting stoichiometric composition is $Cu_{1.78}Se_{0.69}S_{0.31}$. While it may seem odd that a $Cu_{2-x}Se$ precursor can yield a film of $Cu_{2-x}Se_ySy_{1-y}$ composition, we remind the reader that the thiols in the EDA-EDT solvent mixture function as a sulfur source during thermal decomposition of the precursor. It should be noted that Cu vacancies are a common in $Cu_{2-x}X$ (X = S, Se, Te) and values of *x* up to 0.3 are frequently observed.[132, 133] When the precursor is annealed at a higher temperature of

Sample	Precursor Annealing Temperature	Sample Stoichiometry			
	°C	Cu	Ag	Se	S
1	310	1.78 ± 0.06	0	0.69 ± 0.03	0.31 ± 10%
2	350	1.89 ± 0.06	0	0.69 ± 0.03	0.31 ± 10%
3	390	1.94 ± 0.06	0	0.65 ± 0.03	0.35 ± 10%
4	350	1.83 ± 0.06	0.009 ± 10%	0.77 ± 0.03	0.23 ± 10%
5	350	2.03 ± 0.06	0	0	1.00 ± 0.05
6	350	2.03 ± 0.06	0	0.52 ± 0.03	0.48 ± 10%

Table 3.1 The stoichiometry of the samples prepared in this work. Samples 1 - 3 were prepared using the $Cu_{2-x}Se$ precursor and annealed at 310 °C, 350 °C, and 390 °C, respectively. Sample 4 was prepared using a $Cu_{2-x}Se$ - Ag_2S precursor mixture annealed at 350 °C. Sample 5 was prepared using the $Cu_{2-x}S$ precursor and annealed at 350 °C. Sample 6 was prepared using a $Cu_{2-x}Se$ - $Cu_{2-x}S$ precursor mixture annealed at 350 °C.

390 °C, the number of Cu vacancies is reduced and the chemical composition becomes $Cu_{1.94}Se_{0.65}S_{0.35}$. This change in film stoichiometry is facilitated by the loss of chalcogen when the precursor is annealed at higher temperatures. This chalcogen loss can also be observed in the thermogravimetric analysis data; although the curve is approximately flat above 275 °C, a very slow mass loss is visible above this temperature (Figure 3.4).

Since our sample stoichiometries are close to $Cu_{2-x}Se$, we expect our samples to adopt the crystallographic structure of $Cu_{2-x}Se$. Stoichiometric $Cu_{2-x}Se$ has two common phases, the α-phase (monoclinic) which occurs at room temperature and the β-phase (cubic) which

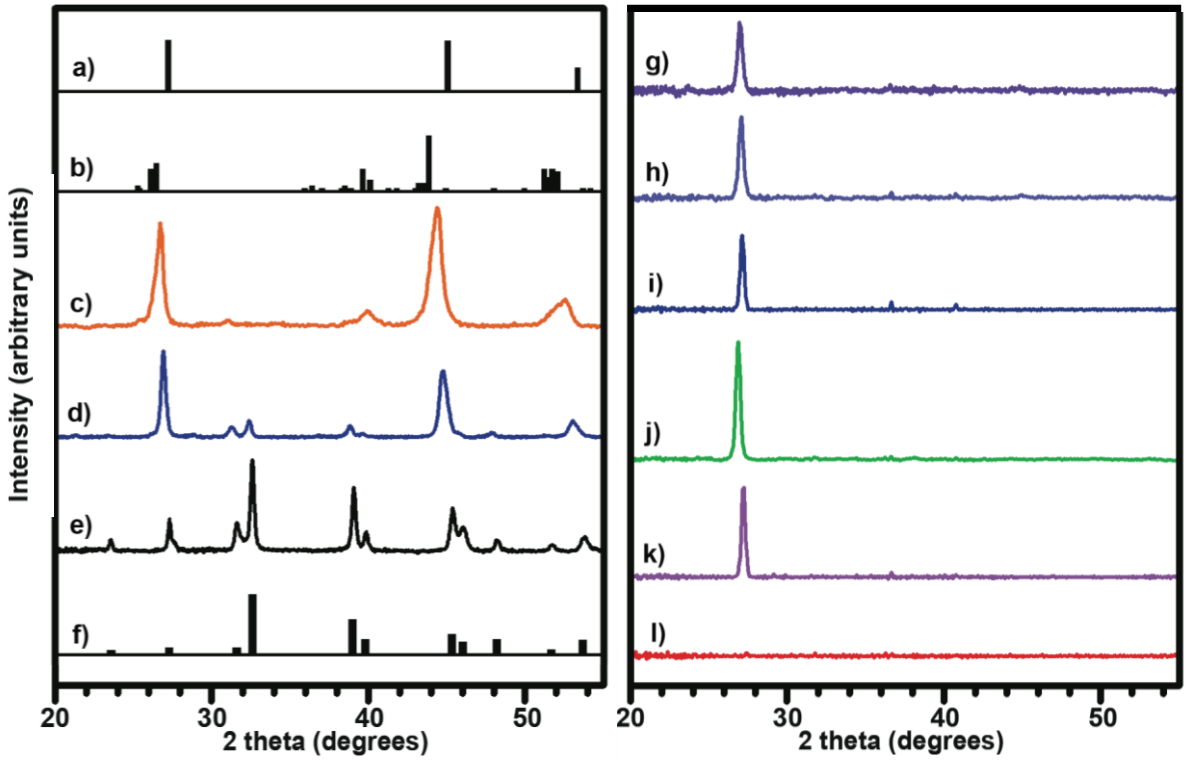

Figure 3.5 X-ray diffraction patterns of samples prepared in this work: (a) powder diffraction file for β-Cu_2Se, file 00-027-1131, (b) powder diffraction file for α-Cu_2Se, file 01-088-2043; diffraction patterns of bulk powders prepared using (c) the Cu_{2-x} Se precursor, (d) a mixture of the $Cu_{2-x}Se$ and $Cu_{2-x}S$ precursors, and (e) the $Cu_{2-x}S$ precursor; (f) powder diffraction file for tetragonal Cu_2S, file 01-072-1071; diffraction patterns of thin films prepared using the $Cu_{2-x}Se$ precursor at varying annealing temperatures of (g) 310°C, (h) 350 °C, and (i) 390 °C; diffraction pattern of thin films with nominal compositions of (j) $Cu_{1.83}Ag_{0.009}Se_{0.77}S_{0.23}$, (k) $Cu_{2.03}Se_{0.52}S_{0.48}$, and (l) $Cu_{2.03}S$.

occurs at temperatures above ~ 140 °C. The α-β transition is a continuous (*i.e.*, second order) phase transition and occurs over an extended temperature range. The transition

temperature for this phase change is also known to sharply decrease as the sample becomes more sub-stoichiometric (*i.e.*, value of x increases).[132, 134-136] In fact, two-phase α + β mixtures are often reported at or near room temperature.[132-138]

The x-ray diffraction pattern of bulk powder prepared from the $Cu_{2-x}Se$ precursor indicates that this process yields two-phase α + β mixtures (Figure 3.5c). Given that our samples have large values of *x*, the presence of a two-phase mixture is not surprising. The peak at 40° and small peak shoulder at 25.5° confirms the presence of the α-phase. A very broad peak spanning 51 - 53° confirms the presence of the β- phase; the right half of this broad peak can be attributed to the β-phase and the left half of this broad peak can be attributed to the α-phase. The peak intensity ratios provide additional evidence for a α + β mixture. For pure α-phase, the ratio of the peaks at 26° and 40° should be approximately equivalent. However, the observed intensity of our 26° peak is much greater than our 40° peak, and we attribute this extra intensity to the presence of the β-phase. Our thin film samples are highly textured and exhibit a strong diffraction peak at 26.9, 27.1, and 27.1° for the samples annealed at 310, 350, and 390 °C, respectively (Figures 3.4g-i). These peaks match more closely to the (111) β-$Cu_{2-x}Se$ reflection at 27.1° than to the (221) α-$Cu_{2-x}Se$ reflection at 26.5°. While the presence of the 27.1° peak confirms the presence of the β-phase in the thin films, this does not necessarily prove the absence of the α-phase. The peak intensities of the α-phase are inherently weaker than the β-phase due to their respective crystal structures (*i.e.*, monoclinic for α-phase and cubic for β-phase). Consequently we presume two possibilities for the crystal structure of these thin films. The

first possibility is that the thin films are indeed mixtures of α- and β-phase $Cu_{2-x}Se$ as in the case of the bulk powder prepared from the $Cu_{2-x}Se$ precursor (Figure 3.5c). If so, this would mean that the weak monoclinic peaks from an only partially monoclinic sub-90 nm thin film are undetectable to our diffractometer. The second possibility is that the surface energy of the thin films causes them to adopt a purely β-phase crystal structure. Our present data cannot definitively differentiate between the abovementioned two possibilities.

The XRD pattern on the bulk $Cu_{2-x}S$ powder prepared from the $Cu_{2-x}S$ precursor exhibits the characteristic peaks of tetragonal $Cu_{2-x}S$ (Figure 3.5e). In the case of the $Cu_{2-x}S$ thin film, no diffraction pattern peaks are observed (Figure 3.5l). This means that either the thin film is amorphous or that the intensity of the thin film's tetragonal diffraction pattern is below our diffractometer's detection limit.

The bulk diffraction from the mixed $Cu_{2-x}Se$-$Cu_{2-x}S$ precursor (Figure 3.5d) was made with the same ratio as Sample 6 in Table 3.1, and so we assume that it has a composition of $Cu_{2.03}Se_{0.52}S_{0.48}$ as well. This diffraction pattern possesses characteristics of both compounds. It maintains the tetragonal diffraction pattern peaks from the $Cu_{2-x}S$ phase, but has the peaks shifted to lower 2theta due to the larger atomic size of Se relative to S. In addition, the dominant peaks transition away from the tetragonal dominant peaks (32° and 39°) to the dominant $Cu_{2-x}Se$ peaks (27° and 45°), thereby confirming that the crystal structure of this sample also possesses characteristics of $Cu_{2-x}Se$. The diffraction pattern of the thin film made with this precursor mixture resembles that of the other thin film samples. It exhibits texturing with a strong diffraction peak at 27.2° (Figure 3.5K).

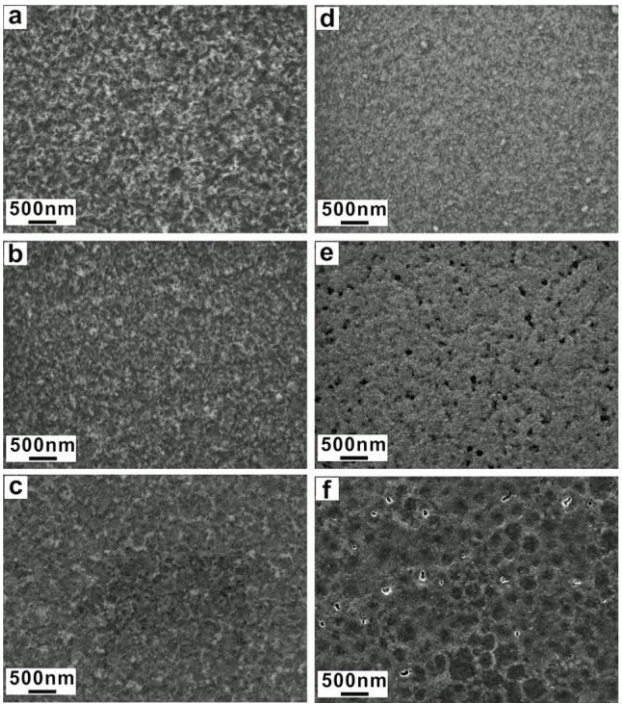

Figure 3.6 Scanning electron microscopy images of thin films prepared using the $Cu_{2-x}Se$ precursor at varying annealing temperatures of (a) 310°C, (b) 350 °C, and (c) 390 °C; and thin films with nominal compositions of (d) $Cu_{2.03}S$, (e) $Cu_{2.03}Se_{0.52}S_{0.48}$, and (f) $Cu_{1.83}Ag_{0.009}Se_{0.77}S_{0.23}$

Prior literature[129, 139, 140] demonstrates thermoelectric performance can be improved by doping $Cu_{2-x}X$ with Ag. Inspired by these results, we created $Cu_{1.83}Ag_{0.009}Se_{0.77}S_{0.23}$ samples by adding Ag_2S precursor to the $Cu_{2-x}Se$ precursor and annealing at 350 °C. The x-ray diffraction pattern of this film is similar to the other films prepared with the $Cu_{2-x}Se$ precursor. It exhibits texturing and a strong diffraction peak at 26.9° (Figure 3.5j).

Figure 3.6 shows scanning electron micrographs of typical $Cu_{2-x}Se_yS_{1-y}$ and Ag-doped $Cu_{2-x}Se_yS_{1-y}$ thin films prepared in this work. Although these films were specular to the eye, the scanning electron micrographs show reveal nanoscale features and pores. The presence of these features and pores can be attributed to the mass loss that occurs during the precursors' physical transformation into $Cu_{2-x}Se_yS_{1-y}$ and Ag-doped $Cu_{2-x}Se_yS_{1-y}$ thin films.

Having determined the salient structural and compositional features of $Cu_{2-x}Se_yS_{1-y}$ and Ag-doped $Cu_{2-x}Se_yS_{1-y}$ films prepared using EDA-EDT solvent mixtures, we proceeded to measure their thermoelectric properties. The energy conversion efficiency of a given thermoelectric material is given by its thermoelectric figure of merit, *ZT*. The thermoelectric figure of merit is given by the expression, $ZT = S^2\sigma T/k$, where *S, σ, T,* and *k* are the Seebeck coefficient, electrical conductivity, absolute temperature, and thermal conductivity. We measured the Seebeck coefficient, electrical conductivity, and thermal conductivity of our samples at room temperature using the steady-state slope method,[131] van der Pauw method,[131] and the 3ω method,[82, 83]respectively.Figure 3.7 shows the effect of precursor annealing temperature on the electrical conductivity, Seebeck coefficient, and thermal conductivity of thin films prepared with the $Cu_{2-x}Se$ precursor. We find that as the annealing temperature increases from 310 to 390 °C, the average Seebeck coefficient increases from 26 to 34 μV/K and the average electrical conductivity decreases from 1380 to 890 1/Ω-cm. The thermal conductivity of these samples was insensitive to annealing temperature and is approximately 0.6 W/m-K. It is worth noting that Lin *et al.*[30] measured the electrical conductivity of similarly prepared $Cu_{2-x}Se$ films that were annealed at 300

°C. Their value of 1168 1/Ω-cm is comparable to our value of 1380 1/Ω-cm obtained for samples annealed at 310 °C. Inspection of Figure 3.7 also shows that the sample-to-sample variations in thermoelectric properties are non-negligible and in some cases can exceed the uncertainty of an individual measurement. The positive sign of the Seebeck coefficient indicates that our samples are p-type, which is typical for $Cu_{2-x}Se$ films where it is well known that Cu vacancies lead to holes.[110, 132] Our observation of an increasing Seebeck coefficient accompanied by a decreasing electrical conductivity is a well-known occurrence that arises from changes in charge carrier concentration. More specifically, it is known that decreasing carrier concentration in a semiconductor decreases electrical conductivity and increases Seebeck coefficient.[106, 141]

We trace our observed electrical conductivity and Seebeck coefficient dependences on annealing temperature to stoichiometric changes in our samples. Inspection of our Rutherford backscattering spectroscopy shows that the amount of Cu vacancies (*i.e.,* value of *x*) decreases from 0.22 to 0.06 as the annealing temperature is increased from 310 °C to 390 °C. Since Cu vacancies in $Cu_{2-x}Se$ lead to holes, this stoichiometric trend indicates that increasing annealing temperature leads to a decrease in hole concentration and consequently a decrease in electrical conductivity. Accompanying this decrease in hole concentration is an increase in Seebeck coefficient as dictated by the interplay of carrier concentration and Seebeck coefficient in thermoelectric materials.[106, 141]

We also varied the Se:S ratio in our $Cu_{2-x}Se_yS_{1-y}$ by mixing in $Cu_{2-x}S$ precursor and annealing at 350 °C. Figure 3.8 shows that as the Se:S ratio is decreased, the average Seebeck coefficient increased from 29 to 83 μV/K and the average electrical conductivity

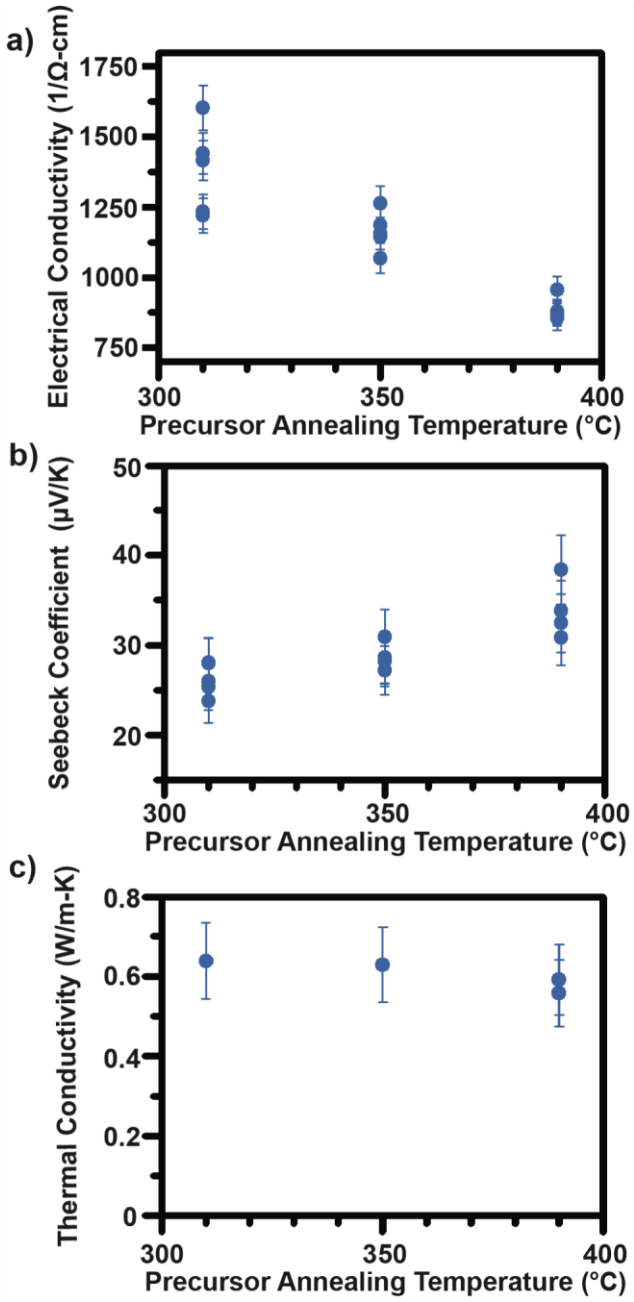

Figure 3.7 Room temperature properties of (a) electrical conductivity, (b) Seebeck coefficient, and (c) thermal conductivity of thin films prepared using the $Cu_{2-x}Se$ precursor at varying annealing temperatures. Each data point and error bar represents a distinct sample and the corresponding measurement uncertainty on that sample.

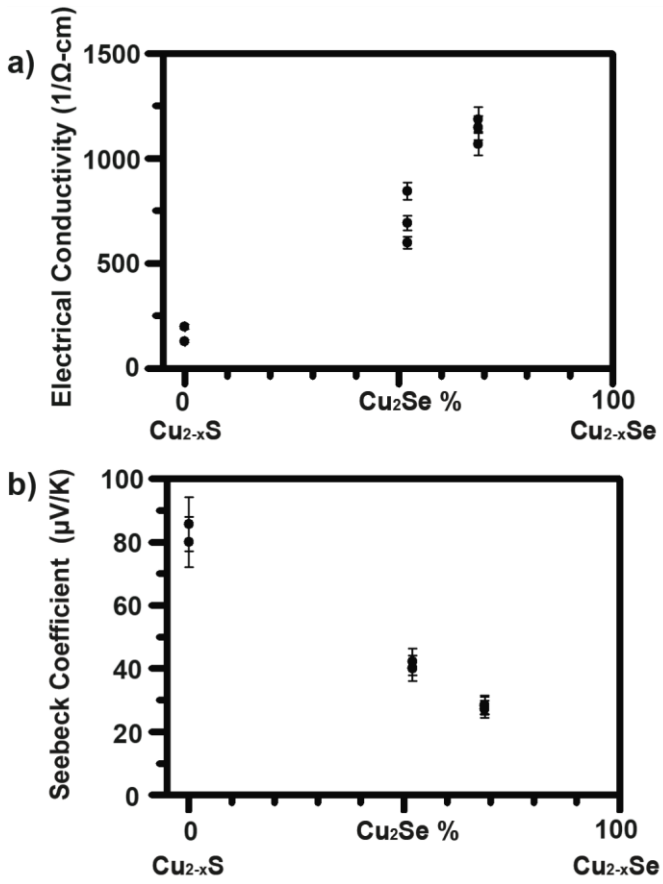

Figure 3.8 Room temperature properties of (a) electrical conductivity and (b) Seebeck coefficient for varying Se:S ratios in samples of $Cu_{2-x}Se_yS_{1-y}$ composition. Each data point and error bar represents a distinct sample and the corresponding measurement uncertainty on that sample. Note that error bars on some data points are smaller than the data points themselves.

decreased from 1163 to 163 1/Ω-cm. This order of magnitude difference in electrical conductivity between samples prepared with the $Cu_{2-x}Se$ and $Cu_{2-x}S$ precursors is similar

to that observed by Lin et al.[125] Part of this change in electrical conductivity can be attributed to stoichiometry. The RBS data shows that the values of x in the samples prepared with the $Cu_{2-x}S$ precursor and $Cu_{2-x}S$ - $Cu_{2-x}Se$ precursor mixture is approximately zero. Consequently these samples should have less charge carriers than the samples prepared with the $Cu_{2-x}Se$ precursor. Our observed increase in Seebeck coefficient as the sample becomes more $Cu_{2-x}S$ rich is also consistent with this decrease in charge carrier concentration. It is also possible that changes in electronic band structure (e.g. band gap, inertial effective mass, density of states effective mass, crystallographic symmetry, etc.) could be contributing to these property trends, however our present data is insufficient to assess this possibility.

Sample	Precursor Annealing Temperature °C	Seebeck Coefficient μV/K	Electrical Conductivity 1/Ω-cm	Thermal Conductivity W/m-K
Ag-1	350	44 ± 10%	1027 ± 5%	--
Ag-2	350	49 ± 10%	1134 ± 5%	--
Ag-3	350	61 ± 10%	869 ± 5%	--
Ag-4	350	--	--	0.42 ± 15%
Ag-5	350	--	--	0.44 ± 15%
Average	--	51	1010	0.43

Table 3.2 The thermoelectric properties of thin films prepared using a $Cu_{2-x}Se$ - Ag_2S precursor mixture annealed at 350 °C. The nominal compositions of these samples are $Cu_{1.83}Ag_{0.009}Se_{0.77}S_{0.23}$.

We next turn our attention to the thermoelectric properties of our Ag-doped $Cu_{2-x}Se_yS_{1-y}$ prepared with a 350 °C annealing temperature, which results in a composition of $Cu_{1.83}Ag_{0.009}Se_{0.77}S_{0.23}$ (Table 3.2). Our efforts to Ag-dope our samples were motivated by the work of Brown *et al.*[139] They studied Cu_2Se and $Cu_{1.97}Ag_{0.03}Se$ and found that Ag-doping increased structural entropy, which in turn dramatically increased *S* and slightly decreased σ around the α-β phase transition temperature region. They also found that doping Cu_2Se with Ag broadened the temperature region of the continuous α-β phase transition, and caused the effect of increased structural entropy to be observed at lower temperatures. Lastly, they found that Ag-doping decreased thermal conductivity by increasing phonon scattering. We observe similar behaviour when comparing the thermoelectric properties of our $Cu_{1.83}Ag_{0.009}Se_{0.77}S_{0.23}$ and $Cu_{1.89}Se_{0.69}S_{0.31}$ samples (Table 3.2 and Figure 3.7). Ag-doping leads to an average Seebeck coefficient of 52 μV/K, which represents an appreciable 80% increase over the non-Ag-doped samples. We note that the larger number of Cu vacancies and larger Se:S ratio in the Ag-doped sample cannot explain this increase in Seebeck coefficient. This is because we already showed that increases in Cu vacancies (Table 3.2 and Figure 3.7) and increases in Se:S ratio (Figure 3.8) both decrease Seebeck coefficient. Ag-doping also improves thermoelectric performance by decreasing thermal conductivity. We find that our Ag-doped samples have an average thermal conductivity of 0.43 W/m-K, which is ~30% lower than the non-Ag-doped samples. Sample-to-sample variations preclude us from definitively knowing if we also observe a small decrease in electrical conductivity with Ag-doping. While we speculate that the thermoelectric properties changes between our $Cu_{1.83}Ag_{0.009}Se_{0.77}S_{0.23}$ and

$Cu_{1.89}Se_{0.69}S_{0.31}$ samples have similar origins to the work by Brown *et al.*,[139] this cannot be conclusively determined with the present data. First, our Ag-concentration is approximately 3 times lower than their work. We note that that our Ag concentrations of 0.009 were near the solubility limit for the $Cu_{2-x}Se$ – Ag_2S precursor mixture and so we could not attempt larger Ag concentrations for this reason. In addition, the behaviour observed by Brown *et al.*[139] requires that the sample be near the α-β phase transition temperature region. This is true for the bulk powder sample prepared from the $Cu_{2-x}Se$ precursor because its XRD pattern exhibits both α- and β-phase peaks. However, the weak diffraction signal from our thin film samples cannot confirm the presence of both α- and β-phases in the thin film samples.

Overall, the room temperature Seebeck coefficients, electrical conductivities, and thermal conductivities of our samples prepared using solution-phase processing of precursors yield similar values to $Cu_{2-x}Se$ alloys made via conventional thermoelectric material processing methods.[110, 128-130, 139] We note that calculating the *ZT* of a thermoelectric material requires that all property measurements be performed along the same direction of the sample. This is not true in our case because our Seebeck coefficient and electrical conductivity measurements are in-plane measurements and our thermal conductivity measurements are cross-plane measurements. However, if one assumes that these properties are isotropic within our films, a ZT of 0.18 can be estimated for the $Cu_{1.83}Ag_{0.009}Se_{0.77}S_{0.23}$ sample. Although this is a modest value, it is important to note that the ZT of $Cu_{2-x}Se$ increases with temperature and large *ZT* values of 1.2 – 1.6 are commonly observed in the 600 -

700°C range.[110, 128-130]Consequently, future high temperature measurements on the solution-phase processed materials in this work could be interesting.

3.4. Summary

We deposited metal chalcogenide semiconductor thin films using soluble precursors created with thiol-amine solvent mixtures and reported the first thermoelectric measurements on materials made in this manner. More specifically, we deposited and studied $Cu_{2-x}Se_yS_{1-y}$ and Ag-doped $Cu_{2-x}Se_yS_{1-y}$ thin films. We found that the precursor annealing temperature affects the metal:chalcogen ratio and leads to carrier concentration changes that affect Seebeck coefficient and electrical conductivity. We also found notable improvements in both Seebeck coefficient and thermal conductivity for our Ag-doped $Cu_{2-x}Se_yS_{1-y}$. Overall, the room temperature thermoelectric properties of our solution-phase processed samples are comparable to those of $Cu_{2-x}Se$ alloys made via conventional thermoelectric material synthesis methods. Achieving parity between solution-phase processing and conventional processing is an important milestone and demonstrates the promise of this binary solvent approach as a solution-phase route to thermoelectric materials.

CHAPTER 4. SOLUTION-PHASE SYNTHESIS AND DEPOSITION OF METAL CHALCOGENIDE PRECURSORS USING ORGANIC DICHALCOGENIDES

4.1 Introduction

There has been a growing interest in solution processing and deposition of inorganic semiconductor due to cost reduction and novel device structure this method enables. Solution processing and deposition of inorganic semiconductor has a potential to be widely used in a number of aspects including photovoltaic,[142] thin film transistors,[22, 143-145] phase change memory,[53, 146] thermoelectrics,[117] etc. However, inorganic semiconductors are generally insoluble due to their strong covalent bonds. Hydrazine, as an exception, was found to possess a great ability to dissolve a variety of metal chalcogenides (SnS_2, In_2Se_3, Cu_2S, etc).[22, 52, 89] In the dissolution process, bulk metal chalcogenides react with E^{2-} (E^{2-} =S^{2-}, Se^{2-}, and Te^{2-}), where E^{2-} is formed by the in-situ reduction of the chalcogen with hydrazine.[23] However, the highly toxic, explosive, and carcinogenic nature of hydrazine makes it problematic for widespread production. To circumvent this problem, a new solvent system, binary diamine-dithiol solvent mixture, was discovered to readily dissolve a large variety of metal chalcogenides.[25] Although this binary solvent approach eliminates the usage of hydrazine, it also poses another problem. The unwanted sulfur brought by dithiol solvent is introduced into the metal selenide/telluride precursors. The amount of leftover sulfur is non-negligible after the precursors are thermal decomposed so that it's hard to make impurity-free and phase-pure metal selenides/tellurides using this diamine-dithiol solvent method.

This chapter proposes a new approach to make soluble metal chalcogenide precursors using safe solvents and eliminating the unwanted sulfur. Diphenyl diselenide/diphenyl ditelluride (Figure 4.1(a),(b)) was firstly dissolved in ethylenediamine or other solvents, and then metal powder was mixed in to form precursors. Using this approach, SnSe, PbSe, SnTe and PbTe precursors were successfully made. X-ray diffraction (XRD) and energy-dispersive x-ray spectroscopy (EDS) were used to determine that the decomposed products from the precursors were sulfur-free and phase-pure. Specially, this approach is the first to be able to make soluble PbSe precursor, and thermally convert back to pure-phase PbSe. Moreover, phase-pure SnTe with no elemental Te phase can also be recovered from our SnTe precursor. This is notable because metal telluride precursors usually yield a mixture of metal telluride and elemental tellurium after thermal decomposition. We also use these precursors to create SnSe and $PbSe_xTe_{1-x}$ thin films by spin coating or drop casting the precursor solution and annealing at elevated temperature. This is the first report of $PbSe_xTe_{1-x}$ thin films made by the deposition of soluble metal chalcogenide precursors. This success on making metal chalcogenide thin films demonstrates this route's strong potential for applications in photovoltaics, thin film transistors, thermoelectrics, etc.

4.2 Experiment and Results

SnSe, PbSe, SnTe, PbTe precursors were prepared in two steps. Use SnSe/PbSe as an example. Firstly, 100 mg diphenyl diselenide (0.32 mmol) was dissolved in 1 ml ethylenediamine. The solution was transparent orange after 5 minutes of stirring. Then an equal number of moles of tin/lead powder (0.32 mmol) was mixed in. For SnTe/PbTe

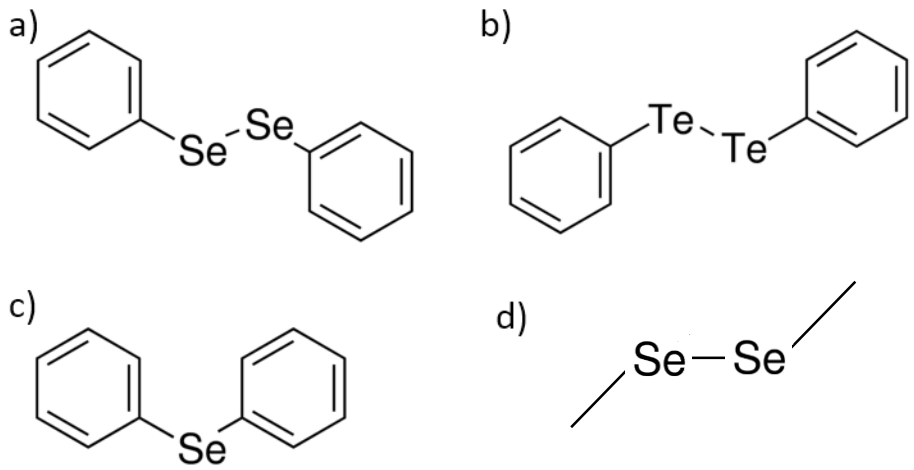

Figure 4.2 Chemicals used in this work: a) Diphenyl Diselenide b) Diphenyl Ditelluride c) Diphenyl Selenide d) Dimethyl Diselenide

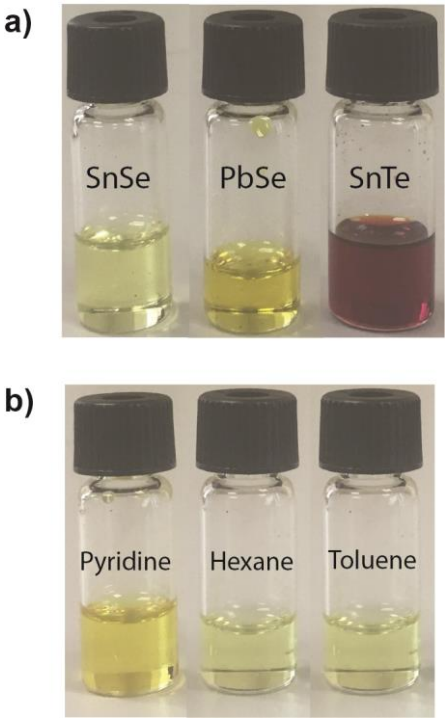

Figure 4.1 a) SnSe, PbSe, and SnTe precursors in ethylenediamine b) SnSe precursors in pyridine, hexane and toluene solvents

precursor, 100 mg diphenyl ditelluride and as equal molar of tin/lead powder were used

instead. After 24 hour stirring, the solutions were filtered to get rid of unreacted powder for further use. SnSe and PbSe precursors were light yellow (Figure 4.2a), and stable over a month. SnTe precursor was light red (Figure 4.2a), but should be used in 24 hours before precipitation happens. PbTe precursor, however, was not stable immediately after being filtered. Gray powder kept precipitating from the light red solution. The precipitates was collected from drop-casting PbTe precursor solution onto the silicon substrate and drying the solvents. All synthesis was proceeded in N_2 filled glove box.

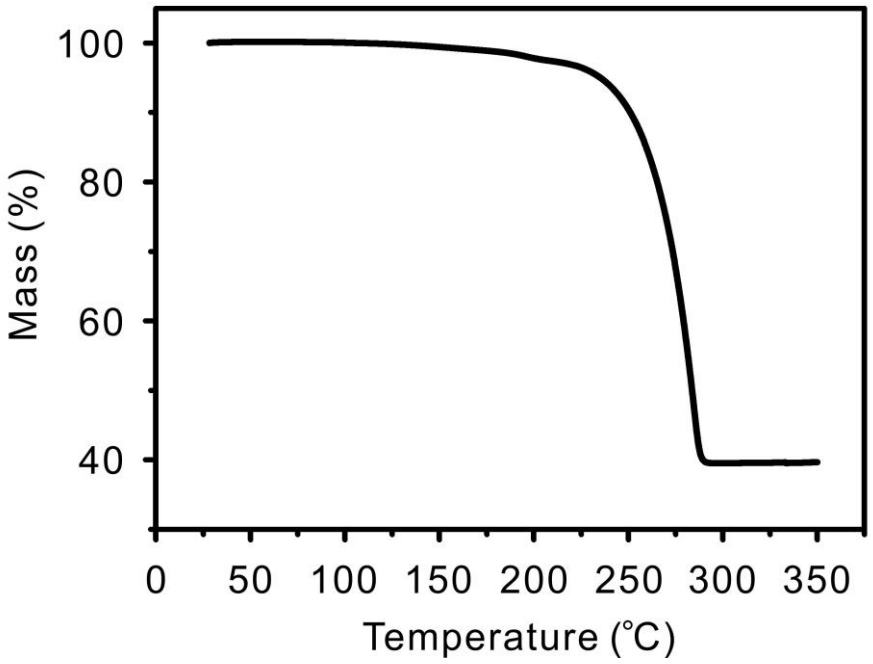

Figure 4.3 Thermogravimetric analysis of the SnSe precursor carried out at a temperature ramp rate of 5 °C/min and conducted in a nitrogen atmosphere. Prior to the thermogravimetric analysis, solvent was removed from the precursor by placing the sample on a hotplate set to 100 °C for 30 minutes.

Thermogravimetric analysis (TGA) was used to determine the temperature needed to recover SnSe from the precursor solution. The TGA analysis sample was prepared by drop-casting the SnSe precursor solution onto a substrate and drying on a hotplate set to 100 °C for 30 min. The solidified precursor was then scraped off of the substrate and then placed into the thermogravimetric analyzer, where it was heated from room temperature to 400 °C at 5 °C/min in a nitrogen atmosphere. TGA analysis result (Figure 4.3) shows that the mass loss in SnSe precursor completes around 300 °C. There is negligible mass loss beyond 300 °C. The temperature needed to recover SnSe is comparable with literature precedent set by diamine-dithiol route and hydrazine route.[22, 25, 29, 52]

Powder x-ray diffraction (XRD) was used to determine the crystal phase of the solid recovered from the precursor decomposition. XRD sample was prepared by drop-casting 50 μl precursor solution onto the silicon substrate, and heating to 300 degree for 30 minutes. XRD results (Figure 4.4) reveals that crystalline and phase-pure orthorhombic SnSe, cubic PbSe and SnTe are recovered after precursor decomposition. The precipitated powder from PbTe precursor is also confirmed to be phase-pure cubic PbTe (Figure 4.4). There are two major findings that are worthwhile to point out. Firstly, we have successfully synthesized soluble PbSe precursor using this approach. Lead chalcogenide is known to be hard to dissolve using hydrazine approach. Dolzhnikov et al. tried to solve this problem by using Na_2Se/Na_2Te instead of elemental chalcogens to increase the reaction driving force, and found lead chalcogenides can then be dissolved in hydrazine.[147] Although this approach makes lead chalcogenide soluble, the decomposing products are not pure phase lead chalcogenide, but with Na instead. To eliminate Na, one has to do a cation exchange

with $N_2H_5^+$. However, there is no report that pure-phase PbSe can be recovered after cation exchange. McCarthy et al. also reported to dissolve metal oxide in diamine-dithiol solvent mixture, and then thermally convert the solution to metal sulfide, by which lead sulfide can be made.[29] They also reported to mix metal oxide and stoichiometric amount of selenium precursor, and thermally decompose the precursor mixture to metal selenide by taking advantage of the difference of volatility between sulfur and selenium. A number of metal selenide can be made using this method including CdSe, ZnSe and Cu_2Se. But no success has been made on PbSe. Our approach, we believe, is the first to be able to make soluble PbSe precursor, and thermally convert back to pure-phase PbSe. The second thing that is important to point out is that we are able to recover pure-phase SnTe with no pure Te impurities as it is known that telluride precursors always result in binary phase mixture of telluride and pure tellurium in hydrazine route and diamine-dithiol route. The presence of Te in hydrazine route is probably because one of the decomposition products is H_2Te, which itself spontaneously turns into H_2 and Te. The attempt to make SnTe using diamine-dithiol route by David H. Webber et al. also yielded SnTe and Te,[27] which seems peculiar because they mixed tin powder and tellurium powder in 2:1 ratio in the solvent and the reaction was completed with no powder left. From a stoichiometric perspective, they should have gotten SnTe and Sn instead. This puzzling result might be worth to explore more with further experiments. In our SnTe percursor, the molar ratio of Sn to Te is 1 to 2. The fact that we recovered phase-pure SnTe after precursor decomposition makes us believe Te must have vaporized in a form of organic tellurides during heat treatment. To further determine the reason, more experiments are needed.

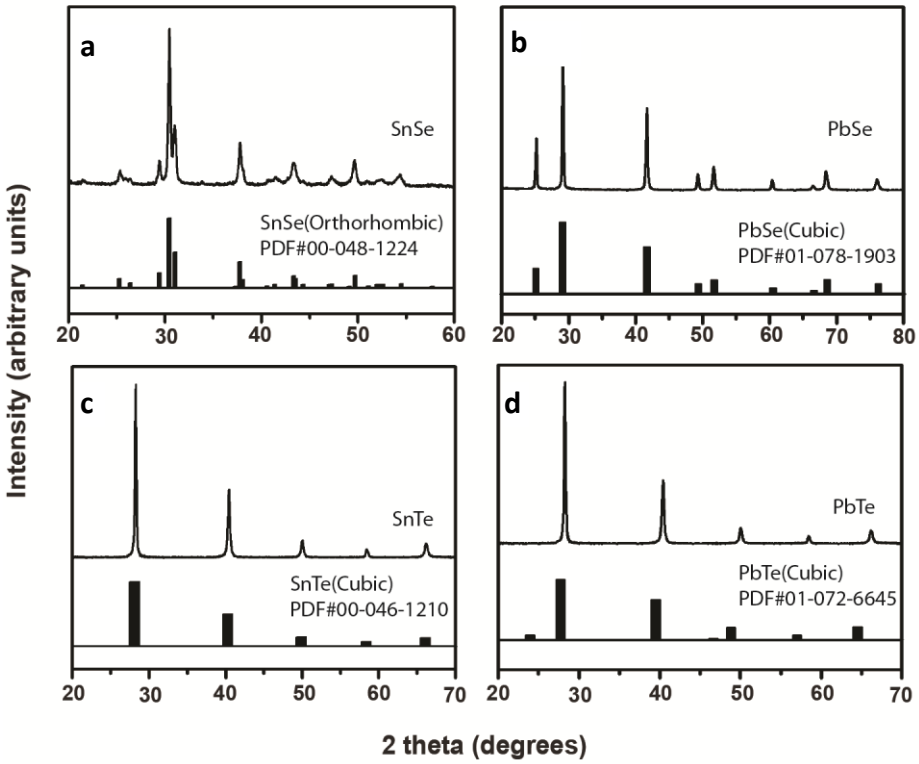

Figure 4.4 Powder diffraction patterns of powder prepared in this work and their powder diffraction files: a) SnSe, b) PbSe, c) SnTe, d) PbTe

Energy-dispersive X-ray spectroscopy (EDS) was used to determine the chemical composition of the recovered SnSe, PbSe, SnTe and PbTe. The samples was prepared in the same fashion as in XRD analysis. The results are shown in Table 4.1. The metal to chalcogen ratios for all four chalcogenides are slightly off unity. However, this might be due to the accuracy limit of EDS. It is important to point out that there is no sulfur detected in those four chalcogenides. In contrast, selenides and tellurides decomposed from precursor using diamine-dithiol route always have a non-negligible amount of sulfur.[25, 27] The inclusion of sulfur can cause altering of lattice constant and material properties. For

example, in the previous chapter, the dissolution of Cu_2Se powder in diamine-dithiol solvent mixture yielded $Cu_{2-x}Se_yS_{1-y}$ after precursor decomposition. It was also found that increasing the Se:S ratio increased electrical conductivity and decreased Seebeck coefficient. Because of the usage of dithiol, the inclusion of unwanted sulfur is inevitable. The approach in this chapter, however, eliminates the introduction of sulfur and gives a chemically pure metal selenide or metal telluride.

Sample Type	*Metal to chalcogen ratio*
SnSe	1.11
PbSe	1.03
SnTe	0.91
PbTe	1.05

Table 4.1 Metal to chalcogen ratio of powder prepared in this work.

With the success of synthesizing SnSe, PbSe, SnTe and PbTe precursors, we then hypothesize the nature of solute in the precursors. Use SnSe an example. We believe that during the dissolution process, the Se-Se bond in diphenyl diselenide breaks, and Se-Sn-Se bond forms (Figure 4.5a). We also hypothesize that the excess stoichiometry during the annealing process leaves the sample in the form of diphenyl selenide (Figure 4.5b). If that is the case, creation of this SnSe precursor should not require the presence of ethylenediamine (note that earlier work using ethylene diamine – ethanedithiol solvent mixtures found that both solvents were necessary to form the precursor). To verify that ethylenediamine is not needed in this precursor approach, we substituted ethylenediamine with other solvents like toluene, hexane and pyridine. The resulting solutions were all

transparent yellow. (Figure 4.2b) The thermally decomposed products were all crystalline pure-phase orthorhombic SnSe verified by XRD.

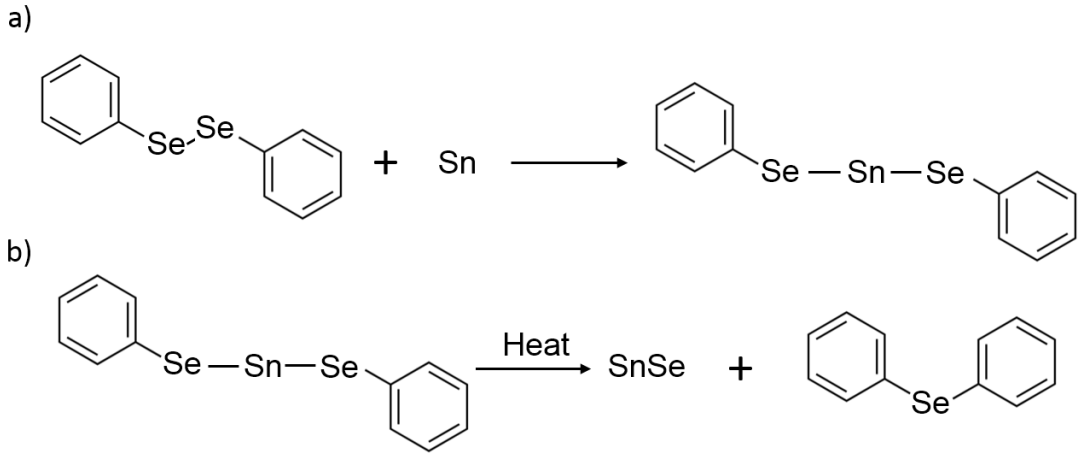

Figure 4.5 The hypothesis of a) the reaction process when Sn is mixed with di-phenyl diselenide in solvents. b) the decomposition process of SnSe precursor.

To provide additional evidence that the precursor formation is driven by the breaking of Se-Se bond, we attempted to form the precursor with diphenyl selenide (Figure 4.1(c)) instead of diphenyl diselenide. Diphenyl selenide does not have a Se-Se bond present because it contains only a single Se atom between two benzene rings instead of two Se atoms. Diphenyl selenide and tin are mixed in 1 to 1 molar ratio in ethylenediamine. The mixture remained unchanged after prolonged stirring. From above, our hypothesis about the nature of the solute is strengthened by the mass loss result from TGA result, the ability of other solvents to dissolve SnSe ,and the absence of Se-Se bonds to prevent dissolution.

It is noted that J.J. Buckley et al.[124] found that for SnS precursor made in ethylenediamine-ethanedithiol solvent mixture, bis(1-2-ethanedithiolate)tin(II) was identified as the likely molecular solute present after the dissolution of Sn, SnO and SnSe in the solvent mixture. In their case, they came up with a similar structure that consisted of Sn(II) four-fold coordinated to two ethanedithiolate groups via the 4 S atoms and then charge balanced via $(enH^{+})_2$ or (enH_2^{2+}) groups. The precursor shown in Figure 4.5 seems to be a reasonable hypothesis structure that would not require ethylenediamine cation charge balancing. Further studies using NMR and Raman spectroscopy could possibly clarify this hypothesis.

There are extensive works which have demonstrated the deposition of soluble metal chalcogenides precursors as a thin film for various applications. For example, phase-pure

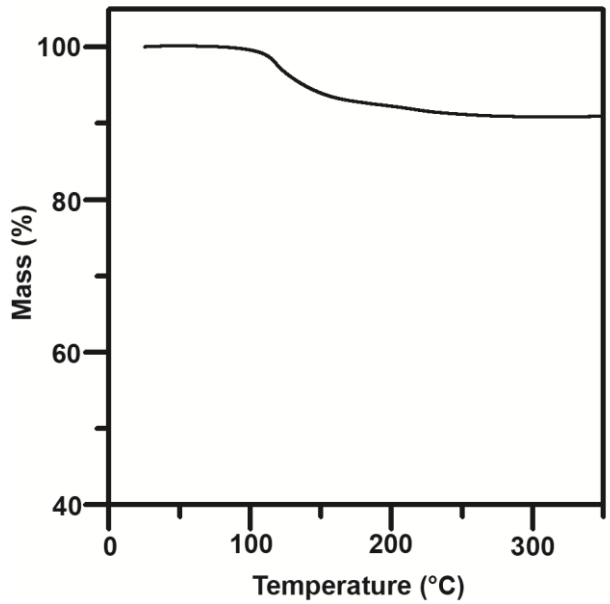

Figure 4.6 Thermogravimetric analysis of the SnSe precursor made by dimethyl diselenide carried out at a temperature ramp rate of 5 °C/min and conducted in a nitrogen atmosphere. Prior to the thermogravimetric analysis, solvent was removed from the pre-cursor by placing the sample on a hotplate set to 100 °C for 30 minutes

SnS, Sb_2Se_3, Bi_2S_3, Cu_2S, Cu_2Se and $CuInSe_2$[25, 28, 29, 125, 148] thin film were successfully deposited and recovered from precursors made by diamine-dithiol route. Similarly, hydrazine route has also shown success to make high quality electronic thin film of $SnSe_xS_y$, In_2Se_3, $CuInTe_2$, $CuInSe_2$, $Cu(Ga_{1-x}In_x)Se_2$, and etc.[22, 23, 52, 142, 149] To complement the researches above, we use our approach to successfully make SnSe and $PbSe_xTe_{1-x}$ thin films, both of which are interesting thermoelectric materials. It should be noted that this is the first report that $PbSe_xTe_{1-x}$ thin film can be made via soluble metal chalcogenide precursors. The failure of making lead chalcogenide thin films in previous work was due to the difficulty for lead chalcogenides to be dissolved in solvents and recovered as pure phase.

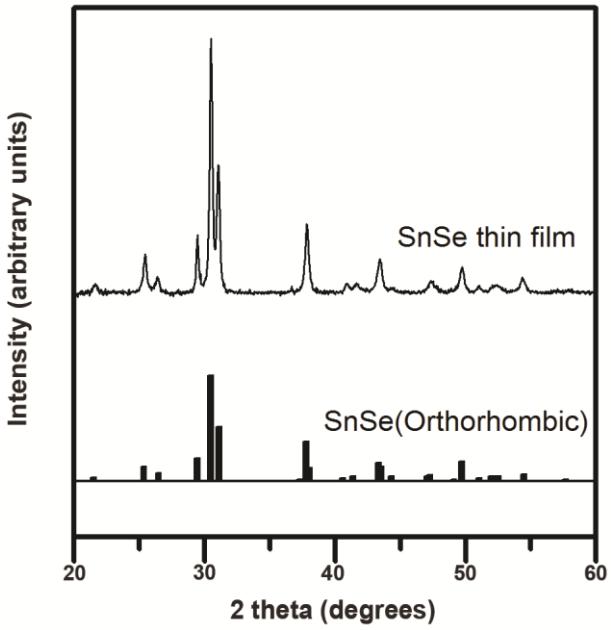

Figure 4.7 X-ray powder diffraction pattern of SnSe thin film and SnSe powder diffraction file

Due to the high mass lass for SnSe precursor during decomposition, forming a complete thin film is very challenging. To circumvent that problem, we substituted diphenyl diselenide with dimethyl diselenide (Figure 4.1 (d)) while making SnSe precursors. 0.64 mmol dimethyl diselenide and 0.64 mmol tin powder were added into 500 µl ethylenediamine. The solution was filtered after 1 day stirring. The final solution had the similar color with the one using diphenyl diselenide. TGA was performed on the precursor powder after pre-drying it at 100 °C. Only 10 percent weight loss was observed from room temperature to 350 °C, and the decomposition finished around 150 °C (Figure 4.6).

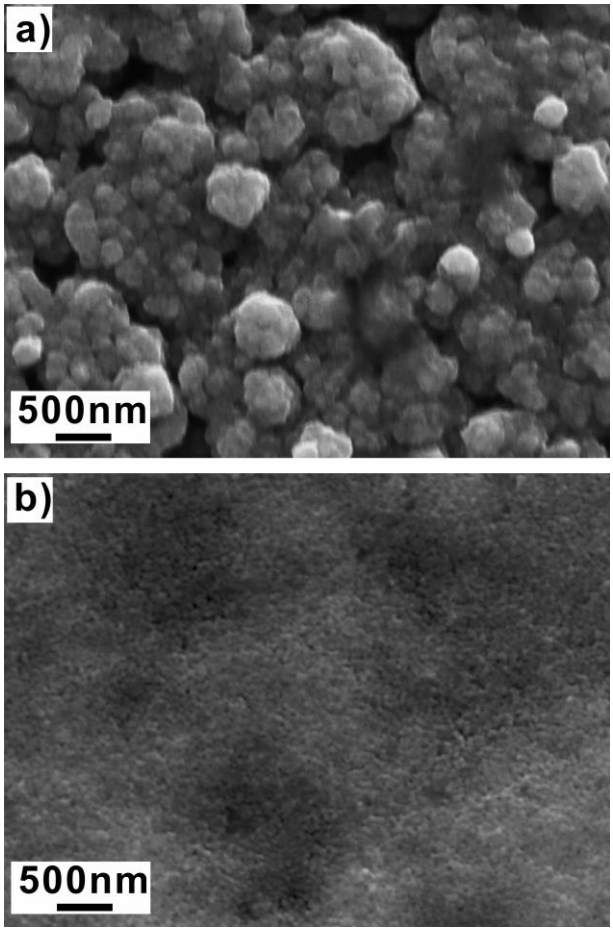

Figure 4.8 SEM image of a) SnSe thin film b) $PbSe_xTe_{1-x}$

If we assume SnSe precursor made with dimethyl diselenide loses weight in the same fashion as the SnSe precursor made with diphenyl diselenide, a simple calculations suggests that a 36 percent weight loss should be observed. This is clearly a much larger mass loss than observed in Figure 4.6. However, Figure 4.6 also shows that much of the mass loss is happening near 100 °C, which is also the temperature we used to pre-dry the precursor. This suggests that thermal decomposition of the precursor may have been occurring during our pre-drying process, which could explain this mass loss discrepancy. Additional experiments with different pre-drying processes should provide clarity on this peculiarity.

The decomposition product was also analyzed by XRD and EDX. The recovered powder was confirmed to be sulfur-free and phase-pure orthorhombic SnSe. To make SnSe thin film, the precursor solution was spin coated onto the quartz/silicon substrate at 5000 rpm

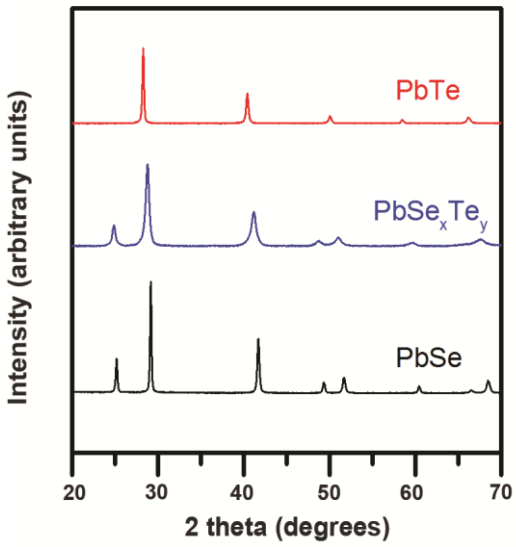

Figure 4.9 Powder diffraction pattern of samples prepared in this work: PbTe (Red), $PbSe_xTe_{1-x}$ (Blue), PbSe (Black)

for 1 minute. The substrate was then heated to 300 °C for 1 minute. Another two coats were followed using the same procedure to ensure the film completeness. The final coat was annealed at 300 °C for 30 minutes. XRD (Figure 4.7) and scanning electronic microscopy (SEM) image (Figure 4.8a) show that the resulting film is polycrystalline and composed of multigrain particles.

To make $PbSe_xTe_y$ compound, 0.24 mmol lead, 0.12 mmol diphenyl diselenide and 0.12 mmol diphenyl ditelluride were mixed in 1 mL ethylenediamine. The solution was stirred for one day, then filtered to remove the remained powder. Unlike the pure PbTe precursor, which was unstable right after filtering, the $PbSe_xTe_{1-x}$ compound precursor remained stable. The presence of diphenyl diselenide increases the precursor stability and solubility compared to pure PbTe precursor, where only diphenyl ditelluride reacts with Pb. The solution was then drop casted onto the silicon substrate, followed by a thermal treatment at 300 °C for 30 minutes. The resulting films were then analyzed by EDX, XRD and SEM analysis. EDX shows that the recovered film has Se to Te ratio about 4. The Te-poor stoichiometry is probably related to the relative poor stability of PbTe precursor compared to PbSe precursor. The remained powder after reaction is possibly composed of unreacted Pb and precipitated PbTe from solvent. Further experiments are needed to confirm the actual composition. Because the decomposed product, $PbSe_xTe_{1-x,}$ is more towards PbSe, XRD peaks of $PbSe_xTe_{1-x}$ (Figure 4.9) are more close to pure PbSe with a slight shift to small angle, which is due to the increase of the lattice constant resulting from the inclusion of larger Te atoms. To make $PbSe_xTe_{1-x,}$ thin film, the original $PbSe_xTe_{1-x}$ precursor was first diluted 2 times, and drop casted onto silicon/quartz substrate. The substrate was then

heated to 300 °C for 30 minutes. The resulting film shown from SEM image (Figure 4.8b) is crack free.

Room temperature thermoelectric property measurements were also performed on the SnSe and $PbSe_xTe_{1-x}$ thin film. Seebeck coefficient measurements were performed using the steady-state slope method, and electrical conductivity measurements were performed using the van der Pauw method and conducted on the same samples used to measure the Seebeck coefficient. The measurement results on SnSe and $PbSe_xTe_{1-x}$ thin film are shown in Table 4.2. Both films showed a high seebeck coefficient while the electronic conductivity was modest.

Thin film Type	*Electronic Conductivity (S/m)*	*Seebeck coefficient (μV/K)*
SnSe	0.05888	665
$PbSe_xTe_{1-x}$	3.36	278

Table 4.2 Room temperature thermoelectric properties of the thin films prepared in this work: SnSe and $PbSe_xTe_{1-x}$

SnSe is a good alternative thermoelectric material since it contains nontoxic and abundant elements. Zhao et al achieved a very high ZT of 2.62 from single crystal hole doped SnSe along a particular crystallographic direction.[108] Inspired by the extraordinary ZT value of signal crystal SnSe, the researchers paid their effort to study the thermoelectric property of polycrystalline SnSe. Most of the studies used solid-state method to fabricate polycrystalline SnSe samples. They reported undoped SnSe possessed high seebeck coefficient (300μV/K to 500μV/K) and very low electronic conductivity at room

temperature due to low carrier concentration.[150-152] To increase the carrier concentration, researchers have tried to dope SnSe with Ag, Na, Cu, Pb and Al.[150-152] They observed significant improvement on electronic conductivity, and a modest sacrifice on Seebeck coefficient, thus an enhancement on ZT value. Our SnSe thin film achieved similar high Seebeck coefficient as those literature results. But a lot of the studies above didn't focus on the room temperature electronic conductivity so that it's hard to compare our electronic conductivity. We believe future improvement in our SnSe thin film can be expected if properly doped. Because those dopants which have been proved effective including Ag, Na, Cu, and Pb all have their corresponding soluble chalcogenides precursors, doping process can be easily accomplished in solution phase.

Previous studies on polycrystalline PbSe made by traditional melting techniques reported Seebeck coefficients of 281 μV/K, [153] which is close to our data, 278 μV/K. Since our $PbSe_xTe_{1-x}$ thin film is more towards PbSe regarding the chemical composition and crystal structure, we feel it is a fair comparison. The equivalent Seebeck coefficient indicates that the carrier concentration in our sample is comparable to their reported data, 10^{18} cm^{-3}, which is close to the ideal carrier concentration for thermoelectric. However the small electrical conductivity in our samples suggest that we have a low carrier mobility. We speculate that our sample has trap states from impurities and/or interfaces that may be limiting mobility. To make future improvements, the origins of these trap states should be identified and the states themselves either eliminated or passivated. In addition, the carrier concentration can be further optimized by various dopants, among which Na, Ag and Sb dopants have been proved successful.[153, 154] Moreover, it was reported that Se to Te ratio

in $PbSe_xTe_{1-x}$ will alter the thermoelectric property,[109] so that Se to Te in our sample can also be optimized towards high ZT value, which should be easy to accomplish in solution phase.

It should be pointed out both bulk SnSe and PbSe were reported to have large ZT value in high temperature (>600K).[108, 109, 150-154] *Since all our current measurements were all conducted in room temperature, future high temperature measurements on those solution-phase deposited thin films could be interesting.*

4.3 Conclusions

We reported a new route to make soluble metal chalcogenide precursors by reacting diphenyl diselenide/diphenyl ditelluride with metal in solvents. By using this method, SnSe, PbSe, SnTe and PbTe precursors were successfully synthesized, and the decomposed products were phase pure and impurity free. Compared to the hydrazine or diamine-dithiol route, our approach uses safe solvents, and avoids introducing unwanted sulfur into the precursor. Moreover, our approach is the first to be able to make a soluble PbSe precursor, and thermally convert back to pure-phase PbSe. Plus, phase-pure SnTe with no elemental Te phase can also be recovered from our SnTe precursor, which is remarkable for metal telluride precursors. We hypothesize that during precursor forming, the Se-Se/ Te-Te bonds in diphenyl diselenide/diphenyl ditelluride break and Se/Te-metal-Se/Te bonds formed. We also successfully make SnSe and $PbSe_xTe_{1-x}$ thin films by spin coating/drop casting precursor solutions and annealing. The initial attempt on thermoelectric property measurements on those thin films show potential for future improvements. Our new

approach is a promising route to enable the construction of low-cost, high performance thin films for photovoltaics, thin film transistors, thermoelectrics, etc.

CHAPTER 5. SUMMARY AND FUTURE DIRECTIONS

This dissertation presents results on solution-phase synthesis and properties of thin films and nanocomposites for thermoelectricity. In Chapter 2, nanocomposites consisting of colloidal nanocrystals embedded in metal chalcogenide matrices is synthesized using metal chalcogenide complexes precursors (MCCs). The thermal conductivity of these composites is on the order of 10^{-1} W/m-K over the entire nanoparticle volume fraction range, which is remarkably low for inorganic crystalline materials and is comparable to amorphous polymers. A rich chemical and structural interaction between nanoparticle and matrix is observed, which contributes to the insensitivity of thermal conductivity to nanoparticle volume fraction. In Chapter 3, the first report on thermoelectric properties of copper chalcogenide thin films deposited soluble precursors in a diamine-dithiol solvent mixture was presented. The interrelationship between composition and room temperature thermoelectric properties was also discussed. Overall, we found that the room temperature thermoelectric property of copper chalcogenide alloys made from this solution-phase synthesis route is comparable to copper chalcogenide alloys made from conventional thermoelectric material processing methods. In Chapter 4, a new route to synthesizing soluble metal chalcogenides precursors was presented. Compared to the hydrazine and diamine-dithiol routes, this new route uses safe solvent and avoids introducing sulfur impurities. We demonstrate that after the decomposition of the precursor solutions, phase-pure and impurity-free metal chalcogenides can be recovered, among which the success to retrieve pure PbSe and SnTe is first reported. The ability to use these precursors to create thin films was also demonstrated. This new approach, as a safe and clean route, opens

numerous directions for further explorations and future applications of soluble metal chalcogenide precursors

The following section will discuss possible future directions based on the above three chapters.

5.1 Opportunity to Make Soluble Pb and Bi Chalcogenide Precursor Using Hydrazine.

Since Mitzi et al.[22, 23] first demonstrated hydrazine possess a great power to dissolve a variety of metal chalcogenides such as tin, indium, antimony, germanium, gallium, mercury, copper, and zinc chalcogenides, a lot of effort has been made to further expand this chemistry. Despite this working for numerous metal chalcogenides, attempts to make lead and bismuth chalcogenides have not had much success. Since lead and bismuth chalcogenides are among the best conventional thermoelectric materials, developing soluble precursors for these compositions is appealing.

In 2015, Dolzhnikov et al. found by introducing A_2Se or A_2Te (A = Na, K, and Cs) instead of elemental chalcogen in hydrazine, lead chalcogenides and bismuth chalcogenides can be successfully dissolved. For example, Na_2PbTe_2 can be made by mixing PbTe and Na_2Te in hydrazine. The Na^+ ions can then be further exchanged with $N_2H_5^+$. The resulting product is $(N_2H_5)_2PbTe_2$. Although Dolzhnikov et al. didn't report $PbTe/Bi_2Te_3$ is successfully made after decomposing corresponding precursor after cation exchange, it could be worthwhile to further investigate using this technique to make $PbTe/Bi_2Te_3$ thin films for thermoelectric applications. This technique is particularly interesting because pure phase $PbTe/Bi_2Te_3$ might be possibly made in contrast to that previous effort on

making $PbTe/Bi_2Te_3$ precursor always yields binary phase, $PbTe/Bi_2Te_3$ and Te. It might be also possible to use $(N_2H_5)_2PbTe_2$ or $(N_2H_5)_4Bi_2Te_5$ as ligands for colloidal nanoparticles to make nanograined materials. The nano-grains should scatter phonons and decrease thermal conductivity, thus enhancing ZT value.

5.2 Opportunity to Use the New Route Proposed in Chapter 4 to Make Thermoeletric Materials

In Chapter 4, we successfully made phase-pure and impurity-free SnSe and $PbSe_xTe_{1-x}$ thin films by depositing the precursor solution made from reacting diphenyl diselenide/diphenyl ditelluride with metals in solvents. Although the initial attempts of thermoelectric measurements on those thin films didn't show a high power factor, there is plenty of room to improve. The future effort can be made on finding a proper dopant to enhance the electronic conductivity. Se:Te ratio in $PbSe_xTe_{1-x}$ thin films can also be adjusted since it's reported that the amount of Se in bulk $PbSe_xTe_{1-x}$ affects the thermoelectric property. Adding dopant and controlling the chemical composition are much easier to achieve by solution-phase synthesis than conventional ways to make thermoelectric materials.

In Chapter 4, we also reported the first soluble PbSe precursor and that can recover pure phase PbSe after decomposition. It will be interesting to try use this PbSe precursor as capping ligands for PbSe/PbTe nanoparticles and make nanocomposite thin films for thermoelectricity. If that could succeed, the capping ligands and the nanoparticles would be composition/phase match, which would facilitate the electronic conductance between

nanoparticles. Moreover, the nano grain size of the nanocomposite thin films based on colloidal nanoparticles would also reduce the thermal conductivity resulting from phonon scattering at grain boundaries. As a result, a promising ZT value should be expected from PbSe/PbTe-PbSe nanocomposite thin films. One can also tune the volume fraction PbTe nanoparticles when making PbTe-PbSe composite films so that the optimal Te:Se ratio can be found to achieve high ZT value.

REFERENCES

1. Thompson, A. C., *X-Ray Data Booklet*. Los Angeles 2009.

2. Goldsmid, H. J.; Douglas, R. W. *British Journal of Applied Physics* 1954**, 5**, 386-390.

3. Ioffe, A. F., *Semiconductor Thermoelements and Thermo-Electric Cooling*. Infosearch Ltd.: 1957, 1957.

4. Hicks, L. D.; Dresselhaus, M. S. *Physical Review B* 1993**, 47**, 16631-16634.

5. Hicks, L. D.; Dresselhaus, M. S. *Physical Review B* 1993**, 47**, 12727-12731.

6. Mahan, G. D.; Sofo, J. O. *Proceedings of the National Academy of Sciences of the United States of America* 1996**, 93**, 7436-7439.

7. Humphrey, T. E.; Linke, H. *Physical Review Letters* 2005**, 94**.

8. Hochbaum, A. I.; Chen, R. K.; Delgado, R. D.; Liang, W. J.; Garnett, E. C.; Najarian, M.; Majumdar, A.; Yang, P. D. *Nature* 2008**, 451**, 163-U5.

9. Venkatasubramanian, R.; Siivola, E.; Colpitts, T.; O'Quinn, B. *Nature* 2001**, 413**, 597-602.

10. Harman, T. C.; Taylor, P. J.; Walsh, M. P.; LaForge, B. E. *Science* 2002**, 297**, 2229-2232.

11. Hsu, K. F.; Loo, S.; Guo, F.; Chen, W.; Dyck, J. S.; Uher, C.; Hogan, T.; Polychroniadis, E. K.; Kanatzidis, M. G. *Science* 2004**, 303**, 818-821.

12. Boukai, A. I.; Bunimovich, Y.; Tahir-Kheli, J.; Yu, J. K.; Goddard, W. A.; Heath, J. R. *Nature* 2008**, 451**, 168-171.

13. Poudel, B.; Hao, Q.; Ma, Y.; Lan, Y. C.; Minnich, A.; Yu, B.; Yan, X. A.; Wang, D. Z.; Muto, A.; Vashaee, D.; Chen, X. Y.; Liu, J. M.; Dresselhaus, M. S.; Chen, G.; Ren, Z. F. *Science* 2008**, 320**, 634-638.

14. Caylor, J. C.; Coonley, K.; Stuart, J.; Colpitts, T.; Venkatasubramanian, R. *Applied Physics Letters* 2005**, 87**.

15. Lee, S. M.; Cahill, D. G.; Venkatasubramanian, R. *Applied Physics Letters* 1997**, 70**, 2957-2959.

16. Kim, W.; Zide, J.; Gossard, A.; Klenov, D.; Stemmer, S.; Shakouri, A.; Majumdar, A. *Physical Review Letters* 2006**, 96**.

17. Dresselhaus, M. S.; Chen, G.; Tang, M. Y.; Yang, R. G.; Lee, H.; Wang, D. Z.; Ren, Z. F.; Fleurial, J. P.; Gogna, P. *Advanced Materials* 2007**, 19**, 1043-1053.

18. Yin, Y.; Alivisatos, A. P. *Nature* 2005**, 437**, 664-70.

19. Rogach, A. L.; Talapin, D. V.; Shevchenko, E. V.; Kornowski, A.; Haase, M.; Weller, H. *Advanced Functional Materials* **12**, 653.

20. Park, J.; Joo, J.; Kwon, S. G.; Jang, Y.; Hyeon, T. *Angew Chem Int Ed Engl* 2007**, 46**, 4630-60.

21. Kovalenko, M. V.; Manna, L.; Cabot, A.; Hens, Z.; Talapin, D. V.; Kagan, C. R.; Kilmov, V.; Rogach, A. L.; Reiss, P.; Milliron, D. J.; Sionnnest, P. G.; Konstantatos, G.; Parak, W. J.; Hyeon, T.; Korgel, B. A.; Murray, C. B.; Heiss, W. *Acs Nano* 2014**, XXX**, 000-000.

22. Mitzi, D. B.; Kosbar, L. L.; Murray, C. E.; Copel, M.; Afzali, A. *Nature* 2004**, 428**, 299-303.

23. Mitzi, D. B. *Advanced Materials* 2009**, 21**, 3141-3158.

24. Dolzhnikov, D. S.; Zhang, H.; Jang, J.; Son, J. S.; Panthani, M. G.; Shibata, T.; Chattopadhyay, S.; Talapin, D. V. *Science* 2015**, 347**, 425-428.

25. Webber, D. H.; Brutchey, R. L. *Journal of the American Chemical Society* 2013**, 135**, 15722-15725.

26. Bulman, G.; Barletta, P.; Lewis, J.; Baldasaro, N.; Manno, M.; Bar-Cohen, A.; Yang, B. *Nature Communications* 2016**, 7**.

27. Webber, D. H.; Buckley, J. J.; Antunez, P. D.; Brutchey, R. L. *Chemical Science* 2014**, 5**, 2498-2502.

28. Antunez, P. D.; Torelli, D. A.; Yang, F.; Rabuffetti, F. A.; Lewis, N. S.; Brutchey, R. L. *Chemistry of Materials* 2014**, 26**, 5444-5446.

29. McCarthy, C. L.; Webber, D. H.; Schueller, E. C.; Brutchey, R. L. *Angewandte Chemie-International Edition* 2015**, 54**, 8378-8381.

30. Zhang, R. H.; Cho, S.; Lim, D. G.; Hu, X. Y.; Stach, E. A.; Handwerker, C. A.; Agrawal, R. *Chemical Communications* 2016**, 52**, 5007-5010.

31. Buckley, J. J.; Greaney, M. J.; Brutchey, R. L. *Chemistry of Materials* 2014**, 26**, 6311-6317.

32. Biswas, K.; He, J.; Blum, I. D.; Wu, C. I.; Hogan, T. P.; Seidman, D. N.; Dravid, V. P.; Kanatzidis, M. G. *Nature* 2012**, 489**, 414-418.

33. Liu, W.; Yan, X.; Chen, G.; Ren, Z. *Nano Energy* 2012**, 1**, 42-56.

34. Mingo, N.; Hauser, D.; Kobayashi, N. P.; Plissonnier, M.; Shakouri, A. *Nano Letters* 2009**, 9**, 711-715.

35. Kim, W.; Zide, J.; Gossard, A.; Klenov, D.; Stemmer, S.; Shakouri, A.; Majumdar, A. *Physical Review Letters* 2006**, 96**, 045901.

36. Biswas, K.; He, J. Q.; Zhang, Q. C.; Wang, G. Y.; Uher, C.; Dravid, V. P.; Kanatzidis, M. G. *Nature Chemistry* 2011**, 3**, 160-166.

37. Liu, M.; Ma, Y.; Wu, H.; Wang, R. Y. *ACS Nano* 2015**, 9**, 1341-1351.

38. Liu, M. L.; Wang, R. Y. *Nanoscale* 2013**, 5**, 7234-7237.

39. Talapin, D. V.; Lee, J. S.; Kovalenko, M. V.; Shevchenko, E. V. *Chemical Reviews* 2010**, 110**, 389-458.

40. Chuang, C. H. M.; Brown, P. R.; Bulovic, V.; Bawendi, M. G. *Nature Materials* 2014**, 13**, 796-801.

41. Caldwell, M. A.; Jeyasingh, R. G. D.; Wong, H. S. P.; Milliron, D. J. *Nanoscale* 2012**, 4**, 4382-4392.

42. Sun, S. H.; Murray, C. B.; Weller, D.; Folks, L.; Moser, A. *Science* 2000**, 287**, 1989-1992.

43. Llordes, A.; Garcia, G.; Gazquez, J.; Milliron, D. J. *Nature* 2013**, 500**, 323-326.

44. Runnerstrom, E. L.; Llordes, A.; Lounis, S. D.; Milliron, D. J. *Chemical Communications* 2014**, 50**, 10555-10572.

45. Dabbousi, B. O.; Bawendi, M. G.; Onitsuka, O.; Rubner, M. F. *Applied Physics Letters* 1995**, 66**, 1316-1318.

46. Trindade, T.; Neves, M. C.; Barros, A. M. V. *Scripta Materialia* 2000**, 43**, 567-571.

47. Guglielmi, M.; Martucci, A.; Menegazzo, E.; Righini, G. C.; Pelli, S.; Fick, J.; Vitrant, G. *Journal of Sol-Gel Science and Technology* 1997**, 8**, 1017-1021.

48. Mokari, T.; Sertchook, H.; Aharoni, A.; Ebenstein, Y.; Avnir, D.; Banin, U. *Chemistry of Materials* 2005**, 17**, 258-263.

49. Llordes, A.; Hammack, A. T.; Buonsanti, R.; Tangirala, R.; Aloni, S.; Helms, B. A.; Milliron, D. J. *Journal of Materials Chemistry* 2011**, 21**, 11631-11638.

50. Kovalenko, M. V.; Scheele, M.; Talapin, D. V. *Science* 2009**, 324**, 1417-1420.

51. Tangirala, R.; Baker, J. L.; Alivisatos, A. P.; Milliron, D. J. *Angewandte Chemie-International Edition* 2010**, 49**, 2878-2882.

52. Mitzi, D. B.; Copel, M.; Chey, S. J. *Advanced Materials* 2005**, 17**, 1285-1289.

53. Milliron, D. J.; Raoux, S.; Shelby, R.; Jordan-Sweet, J. *Nature Materials* 2007**, 6**, 352-356.

54. Feser, J. P.; Chan, E. M.; Majumdar, A.; Segalman, R. A.; Urban, J. J. *Nano Letters* 2013**, 13**, 2122-2127.

55. Nag, A.; Zhang, H.; Janke, E.; Talapin, D. V. *Zeitschrift für Physikalische Chemie* 2015**, 229**, 85-107.

56. Nag, A.; Kovalenko, M. V.; Lee, J. S.; Liu, W.; Spokoyny, B.; Talapin, D. V. *journal of the American Chemical Society* 2011**, 133**, 10612-10620.

57. Zhang, H.; Jang, J.; Liu, W.; Talapin, D. V. *ACS Nano* 2014**, 8**, 7359-7369.

58. Liu, W.; Lee, J. S.; Talapin, D. V. *Journal of the American Chemical Society* 2013**, 135**, 1349-1357.

59. Ko, D. K.; Kang, Y.; Murray, C. B. *Nano Lett* 2011**, 11**, 2841-2844.

60. Choi, J. H.; Fafarman, A. T.; Oh, S. J.; Ko, D. K.; Kim, D. K.; Diroll, B. T.; Muramoto, S.; Gillen, J. G.; Murray, C. B.; Kagan, C. R. *Nano Letters* 2012**, 12**, 2631-2638.

61. Chung, D. S.; Lee, J. S.; Huang, J.; Nag, A.; Ithurria, S.; Talapin, D. V. *Nano Letters* 2012**, 12**, 1813-1820.

62. Lee, J. S.; Kovalenko, M. V.; Huang, J.; Chung, D. S.; Talapin, D. V. *Nature nanotechnology* 2011**, 6**, 348-352.

63. Kim, D. K.; Lai, Y.; Diroll, B. T.; Murray, C. B.; Kagan, C. R. *Nat Commun* 2012**, 3**, 1216.

64. Yun, H. J.; Paik, T.; Edley, M. E.; Baxter, J. B.; Murray, C. B. *ACS applied materials & interfaces* 2014**, 6**, 3721-3728.

65. Yang, D.; Lu, C.; Yin, H.; Herman, I. P. *Nanoscale* 2013**, 5**, 7290-7296.

66. Zhang, Y.; Snedaker, M. L.; Birkel, C. S.; Mubeen, S.; Ji, X.; Shi, Y.; Liu, D.; Liu, X.; Moskovits, M.; Stucky, G. D. *Nano Lett* 2012**, 12**, 1075-1080.

67. Han, M.-K.; Kim, S.; Kim, H.-Y.; Kim, S.-J. *RSC Advances* 2013**, 3**, 4673.

68. Cadavid, D.; Ibáñez, M.; Shavel, A.; Durá, O. J.; López de la Torre, M. A.; Cabot, A. *Journal of Materials Chemistry A* 2013**, 1**, 4864.

69. Kovalenko, M. V.; Spokoyny, B.; Lee, J. S.; Scheele, M.; Weber, A.; Perera, S.; Landry, D.; Talapin, D. V. *Journal of the American Chemical Society* 2010**, 132**, 6686-6695.

70. Wang, R. Y.; Tangirala, R.; Raoux, S.; Jordan-Sweet, J. L.; Milliron, D. J. *Advanced Materials* 2012**, 24**, 99-103.

71. Ong, W. L.; Rupich, S. M.; Talapin, D. V.; McGaughey, A. J.; Malen, J. A. *Nature Materials* 2013**, 12**, 410-415.

72. Pernot, G.; Stoffel, M.; Savic, I.; Pezzoli, F.; Chen, P.; Savelli, G.; Jacquot, A.; Schumann, J.; Denker, U.; Monch, I.; Deneke, C.; Schmidt, O. G.; Rampnoux, J. M.; Wang, S.; Plissonnier, M.; Rastelli, A.; Dilhaire, S.; Mingo, N. *Nature Materials* 2010**, 9**, 491-495.

73. Kim, W.; Wang, R. Y.; Majumdar, A. *Nano Today* 2007**, 2**, 40-47.

74. Poudel, B.; Hao, Q.; Ma, Y.; Lan, Y.; Minnich, A.; Yu, B.; Yan, X.; Wang, D.; Muto, A.; Vashaee, D.; Chen, X.; Liu, J.; Dresselhaus, M. S.; Chen, G.; Ren, Z. *Science* 2008**, 320**, 634-638.

75. Lee, H.; Lan, Y.; Wang, X. W.; Zhu, G.; Dresselhaus, M. S.; Chen, G.; Ren, Z. *Nano Letters* 2008**, 8**, 4670-4674.

76. LeBlanc, S.; Yee, S. K.; Scullin, M. L.; Dames, C.; Goodson, K. E. *Renewable and Sustainable Energy Reviews* 2014**, 32**, 313-327.

77. Ioffe, A. V.; Ioffe, A. F. *Soviet Physics-Solid State* 1960**, 2**, 719-728.

78. Slack, G. A. *Physical Review B* 1972**, 6**, 3791-3800.

79. Yim, J.-H.; Park, H.-H.; Jang, H. W.; Yoo, M.-J.; Paik, D.-S.; Baek, S.; Kim, J.-S. *Journal of Electronic Materials* 2012**, 41**, 1354-1359.

80. Qu, L. H.; Peng, Z. A.; Peng, X. G. *Nano letters* 2001**, 1**, 333-337.

81. Borca-Tasciuc, T.; Kumar, A. R.; Chen, G. *Review of Scientific Instruments* 2001**, 72**, 2139-2147.

82. Cahill, D. G. *Review of Scientific Instruments* 1990**, 61**, 802-808.

83. Lee, S. M.; Cahill, D. G. *Journal of Applied Physics* 1997**, 81**, 2590-2595.

84. Han, G.; Chen, Z. G.; Drennan, J.; Zou, J. *Small* 2014**, 10**, 2747-2765.

85. Ye, J. P.; Soeda, S.; Nakamura, Y.; Nittono, O. *Japanese Journal of Applied Physics, Part 1: Regular Papers, Short Notes & Review Papers* 1998**, 37**, 4264-4271.

86. Raranskii, N. D.; Balazyuk, V. N.; Kovalyuk, Z. D.; Mel'nik, N. I.; Gevik, V. B. *Inorganic Materials* 2011**, 47**, 1174-1177.

87. Howe, J.; Fultz, B., *Transmission Electron Microscopy and Diffractometry of Materials*. 3rd ed.; Springer: New York, 2008.

88. Galiulin, E. A.; Odin, I. N.; Novoselova, A. V. *Zhurnal Neorganicheskoi Khimii* 1982**, 27**, 266-268.

89. Mitzi, D. B. *Inorganic Chemistry* 2007**, 46**, 926-931.

90. Mitzi, D. B. *Inorganic Chemistry* 2005**, 44**, 7078-7086.

91. Cahill, D. G.; Braun, P. V.; Chen, G.; Clarke, D. R.; Fan, S. H.; Goodson, K. E.; Keblinski, P.; King, W. P.; Mahan, G. D.; Majumdar, A.; Maris, H. J.; Phillpot, S. R.; Pop, E.; Shi, L. *Applied Physics Reviews* 2014**, 1**, 011305.

92. Cruceanu, E.; Ionescub.S. *Journal of Materials Science* 1969**, 4**, 570-573.

93. Sofo, J. O. *Journal of Applied Physics* 1995**, 77**, 1561-1563.

94. Rhyee, J. S.; Lee, K. H.; Lee, S. M.; Cho, E.; Il Kim, S.; Lee, E.; Kwon, Y. S.; Shim, J. H.; Kotliar, G. *Nature* 2009**, 459**, 965-968.

95. Wulff, G. *Zeitschrift Fur Krystallographie Und Mineralogie* 1901**, 34**, 449-530.

96. Sirota, N. N.; Berger, L. I. *INZHENERNO-FIZICHESKII ZHURNAL* 1958**, 1**, 117-120.

97. Cahill, D. G.; Watson, S. K.; Pohl, R. O. *Physical Review B* 1992**, 46**, 6131-6140.

98. Swartz, E. T.; Pohl, R. O. *Review of Modern Physics* 1989**, 61**, 605-668.

99. Gavaleshko, N. P.; Gorlei, P. N.; Paranchich, S. Y.; Frasunyak, V. M.; Khomyak, V. V. *Inorganic Materials* 1983**, 19**, 298-300.

100. Duda, J. C.; Smoyer, J. L.; Norris, P. M.; Hopkins, P. E. *Applied Physics Letters* 2009**, 95**, 031912.

101. Hopkins, P. E.; Beechem, T.; Duda, J. C.; Hattar, K.; Ihlefeld, J. F.; Rodriguez, M. A.; Piekos, E. S. *Physical Review B* 2011**, 84**, 125408.

102. English, T. S.; Duda, J. C.; Smoyer, J. L.; Jordan, D. A.; Norris, P. M.; Zhigilei, L. V. *Physical Review B* 2012**, 85**, 035438.

103. Chu, S.; Majumdar, A. *Nature* 2012**, 488**, 294-303.

104. Yee, S. K.; LeBlanc, S.; Goodson, K. E.; Dames, C. *Energy Environ. Sci.* 2013**, 6**, 2561-2571.

105. Vineis, C. J.; Shakouri, A.; Majumdar, A.; Kanatzidis, M. G. *Advanced Materials* 2010**, 22**, 3970-3980.

106. Shakouri, A., Recent Developments in Semiconductor Thermoelectric Physics and Materials. In *Annual Review of Materials Research, Vol 41*, Clarke, D. R.; Fratzl, P., Eds. 2011; Vol. 41, pp 399-431.

107. Biswas, K.; He, J. Q.; Blum, I. D.; Wu, C. I.; Hogan, T. P.; Seidman, D. N.; Dravid, V. P.; Kanatzidis, M. G. *Nature* 2012**, 489**, 414-418.

108. Zhao, L. D.; Lo, S. H.; Zhang, Y. S.; Sun, H.; Tan, G. J.; Uher, C.; Wolverton, C.; Dravid, V. P.; Kanatzidis, M. G. *Nature* 2014**, 508**, 373-+.

109. Pei, Y. Z.; Shi, X. Y.; LaLonde, A.; Wang, H.; Chen, L. D.; Snyder, G. J. *Nature* 2011**, 473**, 66-69.

110. Liu, H. L.; Shi, X.; Xu, F. F.; Zhang, L. L.; Zhang, W. Q.; Chen, L. D.; Li, Q.; Uher, C.; Day, T.; Snyder, G. J. *Nature Materials* 2012**, 11**, 422-425.

111. Ibanez, M.; Luo, Z. S.; Genc, A.; Piveteau, L.; Ortega, S.; Cadavid, D.; Dobrozhan, O.; Liu, Y.; Nachtegaal, M.; Zebarjadi, M.; Arbiol, J.; Kovalenko, M. V.; Cabot, A. *Nature Communications* 2016**, 7**.

112. Kim, G. H.; Shao, L.; Zhang, K.; Pipe, K. P. *Nature Materials* 2013**, 12**, 719-723.

113. Peng, K. L.; Lu, X.; Zhan, H.; Hui, S.; Tang, X. D.; Wang, G. W.; Dai, J. Y.; Uher, C.; Wang, G. Y.; Zhou, X. Y. *Energy Environ. Sci.* 2016**, 9**, 454-460.

114. Hu, X. K.; Jood, P.; Ohta, M.; Kunii, M.; Nagase, K.; Nishiate, H.; Kanatzidis, M. G.; Yamamoto, A. *Energy Environ. Sci.* 2016**, 9**, 517-529.

115. Chowdhury, I.; Prasher, R.; Lofgreen, K.; Chrysler, G.; Narasimhan, S.; Mahajan, R.; Koester, D.; Alley, R.; Venkatasubramanian, R. *Nature nanotechnology* 2009**, 4**, 235-238.

116. Fu, C. G.; Bai, S. Q.; Liu, Y. T.; Tang, Y. S.; Chen, L. D.; Zhao, X. B.; Zhu, T. J. *Nature Communications* 2015**, 6**.

117. Wang, R. Y.; Feser, J. P.; Gu, X.; Yu, K. M.; Segalman, R. A.; Majumdar, A.; Milliron, D. J.; Urban, J. J. *Chemistry of Materials* 2010**, 22**, 1943-1945.

118. See, K. C.; Feser, J. P.; Chen, C. E.; Majumdar, A.; Urban, J. J.; Segalman, R. A. *Nano Letters* 2010**, 10**, 4664-4667.

119. Coates, N. E.; Yee, S. K.; McCulloch, B.; See, K. C.; Majumdar, A.; Segalman, R. A.; Urban, J. J. *Advanced Materials* 2013**, 25**, 1629-1633.

120. Yee, S. K.; Coates, N. E.; Majumdar, A.; Urban, J. J.; Segalman, R. A. *Physical Chemistry Chemical Physics* 2013**, 15**, 4024-4032.

121. LeBlanc, S.; Yee, S. K.; Scullin, M. L.; Dames, C.; Goodson, K. E. *Renewable & Sustainable Energy Reviews* 2014**, 32**, 313-327.

122. Hendricks, T. J.; Yee, S.; Leblanc, S. *Journal of Electronic Materials* 2016**, 45**, 1751-1761.

123. Menon, A. K.; Yee, S. K. *Journal of Applied Physics* 2016**, 119**.

124. Buckley, J. J.; McCarthy, C. L.; Del Pilar-Albaladejo, J.; Rasul, G.; Brutchey, R. L. *Inorganic Chemistry* 2016**, 55**, 3175-3180.

125. Lin, Z. Y.; He, Q. Y.; Yin, A. X.; Xu, Y. X.; Wang, C.; Ding, M. N.; Cheng, H. C.; Papandrea, B.; Huang, Y.; Duan, X. F. *Acs Nano* 2015**, 9**, 4398-4405.

126. Liu, F.; Zhu, J.; Li, Y.; Wei, J. F.; Lv, M.; Xu, Y. F.; Zhou, L.; Hu, L. H.; Dai, S. Y. *Journal of Power Sources* 2015**, 292**, 7-14.

127. Zhao, D. D.; Tian, Q. W.; Zhou, Z. J.; Wang, G.; Meng, Y. N.; Kou, D. X.; Zhou, W. H.; Pan, D. C.; Wu, S. X. *Journal of Materials Chemistry A* 2015**, 3**, 19263-19267.

128. Tyagi, K.; Gahtori, B.; Bathula, S.; Jayasimhadri, M.; Singh, N. K.; Sharma, S.; Haranath, D.; Srivastava, A. K.; Dhar, A. *Journal of Physics and Chemistry of Solids* 2015**, 81**, 100-105.

129. Ballikaya, S.; Chi, H.; Salvador, J. R.; Uher, C. *Journal of Materials Chemistry A* 2013**, 1**, 12478-12484.

130. Yu, B.; Liu, W. S.; Chen, S.; Wang, H.; Wang, H. Z.; Chen, G.; Ren, Z. F. *Nano Energy* 2012**, 1**, 472-478.

131. Borup, K. A.; de Boor, J.; Wang, H.; Drymiotis, F.; Gascoin, F.; Shi, X.; Chen, L. D.; Fedorov, M. I.; Muller, E.; Iversena, B. B.; Snyder, G. J. *Energy Environ. Sci.* 2015**, 8**, 423-435.

132. Ohtani, T.; Tachibana, Y.; Ogura, J.; Miyake, T.; Okada, Y.; Yokota, Y. *Journal of Alloys and Compounds* 1998**, 279**, 136-141.

133. Xiao, X. X.; Xie, W. J.; Tang, X. F.; Zhang, Q. J. *Chinese Physics B* 2011**, 20**.

134. Tonejc, A. *Journal of Materials Science* 1980**, 15**, 3090-3094.

135. Ogorelec, Z.; Celustka, B. *Journal of Physics and Chemistry of Solids* 1966**, 27**, 615-+.

136. Murray, R. M.; Heyding, R. D. *Canadian Journal of Chemistry-Revue Canadienne De Chimie* 1975**, 53**, 878-887.

137. Elakkad, F.; Mansour, B.; Hendeya, T. *Materials Research Bulletin* 1981**, 16**, 535-539.

138. Celustka, B.; Ogorelec, Z. *Journal of Physics and Chemistry of Solids* 1971**, 32**, 1449-&.

139. Brown, D. R.; Day, T.; Borup, K. A.; Christensen, S.; Iversen, B. B.; Snyder, G. J. *Apl Materials* 2013**, 1**.

140. Day, T. W.; Zeier, W. G.; Brown, D. R.; Melot, B. C.; Snyder, G. J. *Applied Physics Letters* 2014**, 105**.

141. Snyder, G. J.; Toberer, E. S. *Nature Materials* 2008**, 7**, 105-114.

142. Mitzi, D. B.; Yuan, M.; Liu, W.; Kellock, A. J.; Chey, S. J.; Deline, V.; Schrott, A. G. *Advanced Materials* 2008**, 20**, 3657-+.

143. Kim, D.; Jeong, Y.; Song, K.; Park, S. K.; Cao, G. Z.; Moon, J. *Langmuir* 2009**, 25**, 11149-11154.

144. Meyers, S. T.; Anderson, J. T.; Hung, C. M.; Thompson, J.; Wager, J. F.; Keszler, D. A. *Journal of the American Chemical Society* 2008**, 130**, 17603-17609.

145. Lee, M. M.; Teuscher, J.; Miyasaka, T.; Murakami, T. N.; Snaith, H. J. *Science* 2012**, 338**, 643-647.

146. Wang, R. Y.; Caldwell, M. A.; Jeyasingh, R. G. D.; Aloni, S.; Shelby, R. M.; Wong, H. S. P.; Milliron, D. J. *Journal of Applied Physics* 2011**, 109**.

147. Dolzhnikov, D. S.; Zhang, H.; Jang, J.; Son, J. S.; Panthani, M. G.; Shibata, T.; Chattopadhyay, S.; Talapin, D. V. *Science* 2015**, 347**, 425-428.

148. Arnou, P.; van Hest, M.; Cooper, C. S.; Malkov, A. V.; Walls, J. M.; Bowers, J. W. *ACS applied materials & interfaces* 2016**, 8**, 11893-11897.

149. Mitzi, D. B.; Copel, M.; Murray, C. E. *Advanced Materials* 2006**, 18**, 2448-+.

150. Chen, C. L.; Wang, H.; Chen, Y. Y.; Day, T.; Snyder, G. J. *Journal of Materials Chemistry A* 2014**, 2**, 11171-11176.

151. Leng, H. Q.; Zhou, M.; Zhao, J.; Han, Y. M.; Li, L. F. *Rsc Advances* 2016**, 6**, 9112-9116.

152. Singh, N. K.; Bathula, S.; Gahtori, B.; Tyagi, K.; Haranath, D.; Dhar, A. *Journal of Alloys and Compounds* 2016**, 668**, 152-158.

153. Wang, H.; Pei, Y. Z.; LaLonde, A. D.; Snyder, G. J. *Advanced Materials* 2011**, 23**, 1366-1370.

154. Fan, H. T.; Su, T. C.; Li, H. T.; Du, B. L.; Liu, B. G.; Sun, H. R.; Zhang, Y. W.; Li, L.; Li, S. S.; Hu, M. H.; Ma, H. G.; Jia, X. P. *Journal of Alloys and Compounds* 2015**, 639**, 106-110.

155. Mohr, M.; Thomsen, C. *Nanotechnology* 2009**, 20**, 115707.

156. Kittel, C., *Introduction to Solid State Physics*. 7th ed.; John Wiley and Sons, Inc.: 1996.

APPENDIX A

CDSE-IN_2SE_3 NANOCOMPOSITE SYNTHESIS AND CHARACTERIZATION

Materials:

$CdCO_3$ (99.998%), stearic acid (90%+) and selenium shot (99.999%) were purchased from Alfa Aesar. Trioctylphosphine (97%) and trioctylphosphine oxide (99%) were purchased from Strem Chemicals. Hydrazine (anhydrous, 98%) was purchased from Sigma Aldrich and then further purified via distillation prior to use.

CdSe Nanocrystal Synthesis:

Wurtzite phase CdSe nanocrystals were synthesized by the hot injection method reported by Qu *et al*.[80] In a typical CdSe nanocrystal synthesis, 0.069 g $CdCO_3$ and 4 g stearic acid were loaded into a three-neck flask. This mixture was then heated to 250°C under N_2 flow until it formed a yellow transparent solution. The solution was then cooled to room temperature and 4 g of trioctylphosphine oxide (TOPO) was added into the flask. The flask was then resealed and heated to 360°C under N_2 flow. A solution of 78mg Se, 0.4 g toluene, and 3.6 g trioctylphosphine (TOP) was then quickly injected into the reaction flask. The reaction solution temperature dropped to 285 °C after injection and then gradually increased to 300 °C over the course of approximately 1 minute. The 300°C growth temperature was then maintained for 1 minute and the heating mantle was then removed from the flask. The flask was cooled by natural convection to the ambient air until the temperature reached 150°C, at which point it was further cooled by immersion in a water bath. Once the temperature was below 50°C, the flask was removed from the Schlenk line and toluene was added to the reaction mixture to prevent solidification (1:1 toluene:reaction mixture). The CdSe nanocrystals were then precipitated by adding

ethanol, and re-suspended in toluene two times. The CdSe nanocrystals were precipitated an additional time and re-suspended in hexane.

$(N_2H_4)_2(N_2H_5)_2In_2Se_4$ Precursor Synthesis:

$(N_2H_4)_2(N_2H_5)_2In_2Se_4$ precursor was made by mixing 1.25mmol In_2Se_3, 3.75 mL of N_2H_4, and 1.25 mL of a 1 M solution of Se in N_2H_4. The mixture was stirred for two days and the resulting viscous light green solution was filtered with a 200 nm PVDF filter.

Ligand Exchange Process:

In a typical ligand exchange process, two separate solutions were prepared: (A) CdSe nanocrystal solution in hexane (15 mg/mL) and (B) 0.25 M solution of $(N_2H_4)_2(N_2H_5)_2In_2Se_4$ in hydrazine. Solution B was then diluted with 2 mL of N_2H_4 and then 2 mL of Solution A was added to Solution B. This resulted in a bi-layer of liquid with the hexane phase on top and the N_2H_4 phase on bottom. This mixture was stirred for several hours, during which the hexane phase changed from dark to colorless and the hydrazine phase changed from colorless to dark, indicating that the ligand exchange was complete. The hexane was then removed and the hydrazine phase was filtered through a 200 nm PVDF filter. The CdSe nanocrystals with In_2Se_3 MCC ligands were then separated from unbound In_2Se_3 MCC precursor by precipitating via the addition of acetonitrile. The CdSe nanocrystals were then re-suspended in N_2H_4.

Nanocomposite Formation:

100% In_2Se_3 nanocomposites were made by directly using the In_2Se_3 MCC precursor. ~100% CdSe nanocomposites were prepared with the solution of CdSe nanocrystals with

In_2Se_3 MCC precursor ligands. Variation of CdSe mole fraction was achieved by mixing appropriate amounts of $(N_2H_4)_2(N_2H_5)_2In_2Se_4$ back into the solution of CdSe nanocrystals with In_2Se_3 MCC precursor ligands. Silicon substrates were prepared for nanocomposite deposition by cleaning with acetone, isopropanol, and UV ozone treatment. Nanocomposite thin film samples were prepared by spin-coating the solutions onto the silicon substrates, drying for several minutes, and then heating to 350°C for 30 minutes. Film thickness was controlled by solution concentration and spin speed.

Thermogravimetric Analysis:

Samples for thermogravimetric analysis (TGA) were prepared by drying the In_2Se_3 MCC precursor under a nitrogen flow to remove solvent. The dried precursor was orange in color and then crushed into a fine powder prior to the TGA measurement. TGA was done using a Mettler Toledo TGA/DSC1 Star system. The TGA measurement was done under a nitrogen atmosphere, during which the sample was heated at 2 °C/min from room temperature to 350 °C, maintained at 350 °C for 30 minutes, and then heated at 2 °C from 350 °C to 450 °C. The In_2Se_3 MCC precursor, $(N_2H_4)_2(N_2H_5)_2In_2Se_4$, contains weakly bound N_2H_4 groups that are easily removed during the abovementioned drying process. Consequently, a final decomposition product of In_2Se_3 implies a final mass between 69% and 76%. This corresponds to an initial condition between $(N_2H_4)_2(N_2H_5)_2In_2Se_4$ and $(N_2H_5)_2In_2Se_4$, respectively.

Transmission Electron Microscopy:

Transmission electron microscope (TEM) images were taken by a Philips CM200-FEG high resolution TEM. TEM samples of the CdSe nanocrystals with organic ligands were prepared by drop-casting 50 μL of a dilute nanocrystal suspension onto a carbon film supported copper TEM grid. The nanocrystal diameter was determined with ImageJ by analyzing a representative TEM image containing 100 - 200 CdSe nanocrystals. In_2Se_3 TEM samples were prepared by drop casting 2 μL of a dilute $(N_2H_4)_2(N_2H_5)_2In_2Se_4$ precursor onto a Si_3Ni_4 window and then annealing at 350°C for 30 min. The grain size of In_2Se_3 was determined by manually measuring 60 grains and taking the average. The nanocomposite TEM samples were prepared in a similarly to the 100% In_2Se_3 samples.

Scanning Electron Microscopy:

Scanning electron microscope (SEM) images were taken by a Nova 200 Nanolab SEM. SEM samples of nanocomposite were prepared by spin-coating the solution onto the silicon substrates, drying for several minutes, and then heating to 350°C for 30 minutes. The film thickness varied between 50 and 100 nm.

Elemental Composition Characterization:

A 1.7 MV Tandetron Ion Accelerator made by General Ionex was used for Rutherford backscattering spectroscopy (RBS) and particle-induced x-ray emission (PIXE). PIXE was done with 2.8 MeV H^+ ions and used to acquire the Cd:In ratio by analyzing the *K* x-ray emission. RBS was done with 2 MeV He^{2+} ions to acquire a Se peak and a combined Cd-In peak. The Cd:In ratio from PIXE along with the RBS data was then analyzed using an

RBS fitting program (RUMP) to obtain the final elemental ratios. As mentioned in the main text, the ~100% CdSe composite samples had trace amounts of In due to the In_2Se_3 MCC surface functionalization of the CdSe nanocrystals. We note that this RBS-PIXE technique could not precisely determine the amount of trace In, but could confirm that the In was less than 3 at% of the composite.

X-ray Diffraction:

Powder diffraction pattern was performed by a high-resolution X-ray diffractometer (XRD, PANALYTICAL X'PERT PRO) with CuKα X-ray source operating at 40 kV AND 40 mA. Thin film XRD samples were prepared by spin coating solutions onto silicon substrates, and decomposing at 350°C for 30 minutes. Powder XRD samples were prepared similarly, but were drop cast instead of spin coated.

APPENDIX B

CALCULATION OF RELATIVE PEAK INTENSITIES FOR CDSE AND $CDIN_2SE_4$

The peak intensity of an *hkl* reflection in a XRD pattern is proportional to:

$$I \propto |S|^2 \frac{M}{V_c^2}$$

where S is the structure factor, M is the multiplicity factor, and V_c is the unit cell volume. The structure factor can be calculated as:

$$S = \sum_i^N f_i \, exp\left[-2\pi i\left(h x_i + k y_i + l z_i\right)\right]$$

where $(h\ k\ l)$ are the Miller indices of the plane of interest, $(x_i\ y_i\ z_i)$ are the position of the ith atom in the unit cell, N is the total number of atoms in the unit cell, and f is the atomic form factor. CdSe has a wurtzite structure with the following atomic positions:

Cd	(0 0 0)
Cd	(1/3 2/3 1/2)
Se	(0 0 3/8)
Se	(1/3 2/3 7/8)

$CdIn_2Se_4$ has a tetragonal structure with the following atomic positions:

Cd	(0 0 0)
In	(1/2 0 1/2)
In	(0 1/2 1/2)
Se	(1/4 1/4 1/4)
Se	(3/4 1/4 3/4)
Se	(1/4 3/4 3/4)
Se	(3/4 3/4 1/4)

The table below contains the parameters that were used for calculations of the relative peak intensities for CdSe and $CdIn_2Se_4$ as based on analysis of the structure factor, multiplicity factor, and unit cell volume. The intensity of the (1 1 1) peak in $CdIn_2Se_4$ is larger than the (0 0 2) and (1 0 0) peaks of CdSe by factors of 3.7 and 6.8, respectively (i.e.

rightmost column of table below). Note that since these peaks all occur at approximately the same 2θ, the other factors contributing to XRD peak intensity (i.e. Lorentz factor, polarization factor, absorption factor, and temperature factor) should be approximately equivalent.

Peak	$\|S\|^2$	M	V_c (Å^3)	$\|S\|^2M/V_c$ (Å^{-3})
CdSe (1 0 0)	5.40×10^3	3	112	1.29
CdSe (0 0 2)	1.49×10^4	2	112	2.38
$CdIn_2Se_4$ (1 1 1)	4.22×10^4	8	196	8.79

APPENDIX C

CAHILL-POHL MODEL CALCULATION

The Cahill-Pohl model (note that the Cahill-Pohl model is also commonly referred to as the "minimum thermal conductivity model" and the "amorphous limit") is a simple calculation that is commonly used to estimate the thermal conductivity of amorphous materials. It is given by the equation:[97]

$$k_{mi} = \left(\frac{\pi}{6}\right)^{1/3} k_B n^{2/3} \sum_i v_i \left(\frac{T}{\Theta_i}\right)^2 \int_0^{\Theta_i/T} \frac{x^3 e^x}{(e^x - 1)^2} dx$$

where k_B is the Boltzmann constant, n is the number density of atoms, T is the absolute temperature, and v_i and Θ_i are the speed of sound and Debye temperature of the ith phonon branch. We used the following inputs in our implementation of the Cahill-Pohl model for CdSe:[155]

n	3.68×10^{28} m^{-3}
$v_{longitudinal}$	3780 m/s
$v_{transverse,1}$	1490 m/s
$v_{transverse,2}$	1490 m/s

The values for the Debye temperatures can be calculated as:[156]

$$\Theta_i = v_i \left(\frac{\hbar}{k_B}\right)\left(6\pi^2 n\right)^{1/3}$$

where $\hbar$ is the reduced Planck constant. Although there is no available literature on the speed of sound for γ-In_2Se_3, there is available literature for α-In_2Se_3.[86] Since an amorphous material should be phase independent, we use the properties of α-In_2Se_3 in our calculations for the Cahill-Pohl model. Furthermore, since our thermal conductivity measurements of γ-In_2Se_3 were approximately along the c-axis, we use the c-axis properties of α-In_2Se_3 for our calculation:

n	7.29×10^{27} m^{-3}
$v_{longitudinal}$	2679 m/s
$v_{transverse,1}$	1728 m/s
$v_{transverse,2}$	1728 m/s

Using the above equations and values, we estimate that the thermal conductivities of amorphous CdSe and amorphous In_2Se_3 are 0.40 W/m-K and 0.13 W/m-K, respectively.

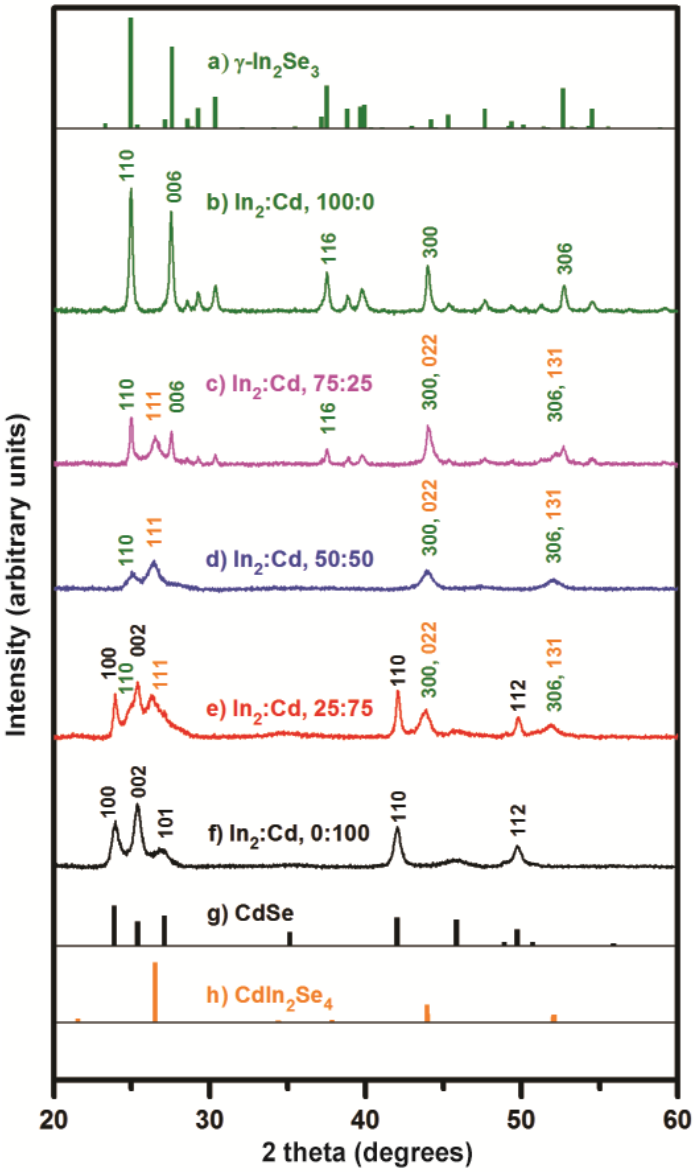

Figure S1 X-ray diffraction patterns of (a) γ-In_2Se_3 powder diffraction file 01-089-0658, nanocomposite powders with In_2:Cd ratios of (b) 100:0, c) 75:25, (d) 50:50, and (e) 25:75, (f) 0:100, (g) CdSe powder diffraction file 01-077-0021, and (h) $CdIn_2Se_4$ powder diffraction file 00-056-1124.

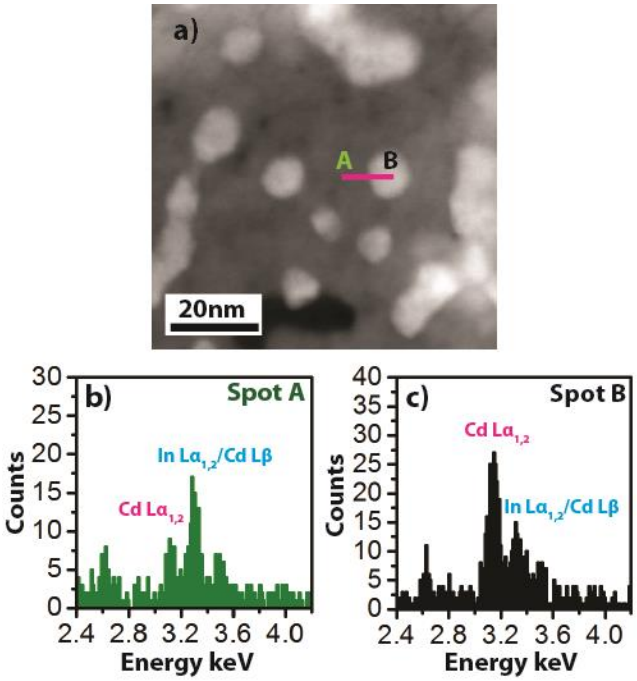

Figure S2 (a) Dark field scanning transmission electron microscopy image of nanocomposite with In_2:Cd ratio of 50:50. **(b)** Energy-dispersive X-ray spectroscopy (EDX) on Spot A, which corresponds to the In_2Se_3 matrix **(c)** EDX on Spot B, which corresponds to a CdSe . The EDX peak at ~3.1 keV corresponds to $L_{\alpha 1,2}$ transitions of Cd whereas the peak at ~3.3 keV corresponds to both the L_β transitions of Cd and the $L_{\alpha 1,2}$ transitions of In. Since the ratio of the $L_{\alpha 1,2}$ to L_β transition in Cd is 1.9,[1] it can be seen that Spot A is In-rich whereas Spot B is Cd-rich. Given the nanoscale features of our composite and since x-rays are generated from a relatively large volume during EDX, our apparent detection of Cd in the In_2Se_3 matrix and vice versa is to be expected.

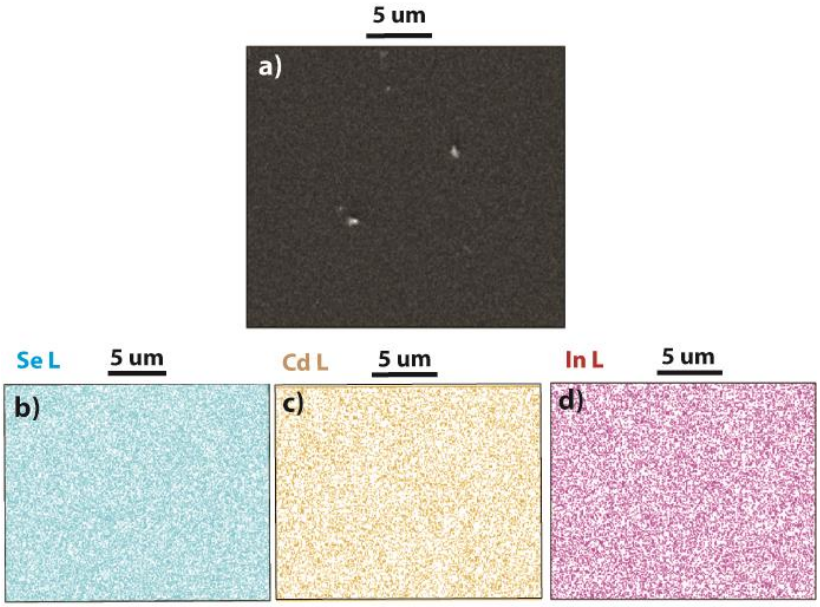

Figure S3 a) Scanning electron microscopy image of a nanocomposite with In_2:Cd ratio of 41:59. Energy-dispersive X-ray (EDX) maps of **(b)** Se, **(c)** Cd, and **(d)** In show an uniform elemental distribution in the composite.

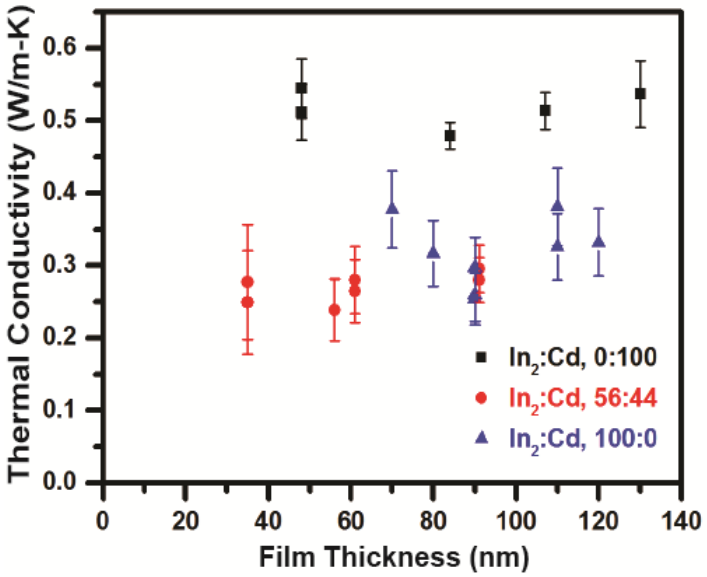

Figure S4 Thermal conductivity of nanocomposite thin films as a function of film thickness for composites with In_2:Cd ratios of 0:100 (black squares), 56:44 (red squares), and 100:0 (blue triangles). The lack of correlation between thermal conductivity and film thickness indicates that transport in these films is diffusive and that the thermal contact resistances between layers of the 3ω thermal conductivity samples are negligible

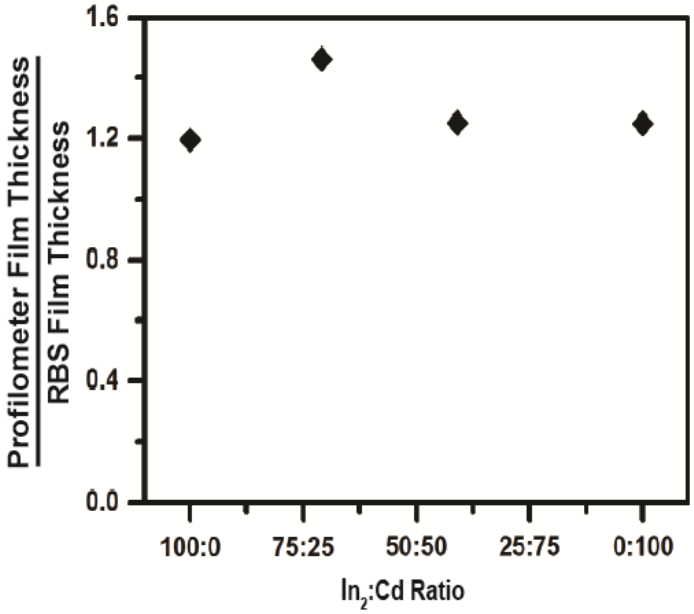

Figure S5 Ratio of film thickness measured by profilometry to film thickness measured by Rutherford backscattering spectroscopy for composites with varying In_2:Cd ratios. Film thicknesses determined by Rutherford backscattering spectroscopy used the measured areal atomic density and assumed fully dense films. All samples in this figure had film thicknesses of approximately 50 – 60 nm.

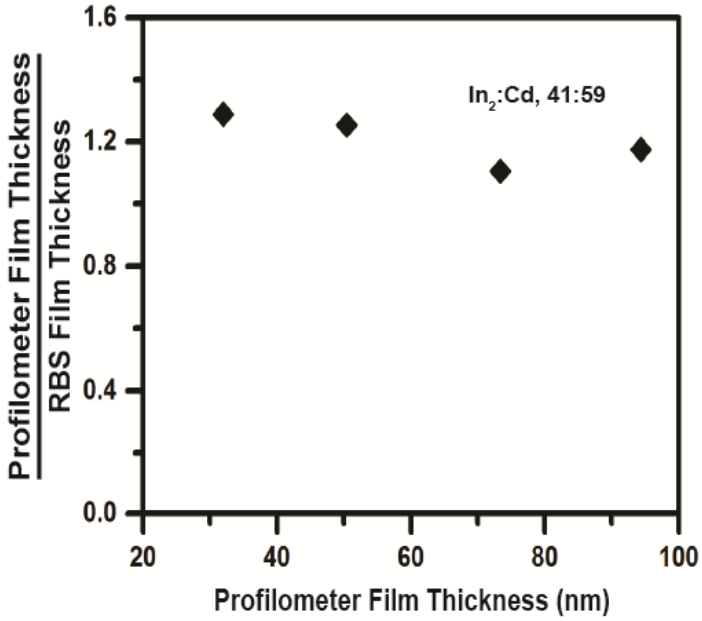

Figure S6 Ratio of film thickness measured by profilometry to film thickness measured by Rutherford backscattering spectroscopy for composites with varying thicknesses. Film thicknesses determined by Rutherford backscattering spectroscopy used the measured areal atomic density and assumed fully dense films. All samples in this figure have an In_2:Cd ratio of 41:59.